



UNIVERSITÀ  
di **VERONA**

UNIVERSITY OF VERONA

*DEPARTMENT OF*

*Neurosciences, Biomedicine and Movement*

*SECTION OF*

*Anatomy and Histology*

*PhD PROGRAM in*

*Natural sciences and engineering*

*PhD in Nanoscience and advanced Technologies*

*PRESENTED BY **FEDERICA VURRO***

*32° CYCLE*

**CHARACTERIZATION AND OPTIMIZATION OF NANO-STRUCTURES  
WITH HYPERTHERMIC PROPERTIES FOR BIOMEDICAL APPLICATIONS.**

S.S.D. BIO/16 HUMAN ANATOMY

COORDINATOR: Prof. Franco TAGLIARO

TUTOR: Dott.ssa Laura CALDERAN

PhD STUDENT: Federica VURRO

Quest'opera è stata rilasciata con licenza Creative Commons Attribuzione – non commerciale Non opere derivate 3.0 Italia. Per leggere una copia della licenza visita il sito web

<http://creativecommons.org/licenses/by-nc-nd/3.0/it/>

Characterization and evaluation of nano-structures with hyperthermic properties  
for biomedical applications. – FEDERICA VURRO

Tesi di dottorato

Verona, 10 Dicembre 2019

ISBN





## SOMMARIO

Negli ultimi anni, il nostro gruppo si è concentrato sullo studio di nanoparticelle magnetiche (MNPs), che sono in grado di indurre ipertermia, come potenziali strumenti biomedici. “Ipertermia magnetica” è un termine usato per indicare la generazione di calore da parte di MNPs in risposta all'applicazione di un campo magnetico esterno alternato. Abbiamo applicato l'ipertermia *in vitro* con scopi diversi e gli effetti sulle cellule sono stati analizzati applicando test di vitalità e valutazioni morfologiche con tecniche di microscopia ottica ed elettronica (TEM). Abbiamo usato NP superparamagnetiche di ossido di ferro per indurre la delipidazione negli adipociti 3T3L1 e nelle cellule staminali adulte derivate da tessuto adiposo umano. Immediatamente dopo l'ipertermia, abbiamo osservato una drastica perdita di materiale lipidico intracellulare che è persistita per almeno 24 ore in assenza di morte, danno o dedifferenziazione. Questi risultati aprono prospettive interessanti per l'applicazione dell'ipertermia nel trattamento dell'obesità. Abbiamo applicato un trattamento ipertermico anche alle cellule tumorali, note per essere più sensibili allo *shock* termico rispetto alle cellule sane, al fine di indurre l'apoptosi. Una linea cellulare di glioblastoma (U87MG) è stata trattata con le Zn-SPIONs o con NP biomimetiche magnetiche (BMNP). Zn-SPIONs sono ossido di ferro( $\text{Fe}_3\text{O}_4$ ) ricoperti con zinco di dimensioni pari a  $15 \pm 2$  nm e presentano un'elevata capacità termica. Le BMNPs, sintetizzate con la proteina MamC da batteri magnetotattici, possono agire sia come trasportatori di farmaci che come agenti ipertermici, e potrebbero essere strumenti promettenti per il trattamento di molti tipi di tumore. Le BMNPs sono state testate anche su una linea cellulare di epatocarcinoma umano (HepG2) dopo la funzionalizzazione con un inibitore della colina chinasi al fine di ottenere una nanoparticella potenzialmente adatta per la chemioterapia mirata. In effetti, la colina chinasi è considerata un biomarcatore della progressione del tumore e della carcinogenesi. Pertanto, queste nanoparticelle consentirebbero un trattamento locale del cancro evitando / riducendo possibili effetti collaterali sistemici. L'internalizzazione delle BMNPs è stata valutata utilizzando la microscopia elettronica. Nel loro insieme, i nostri risultati dimostrano l'efficacia delle MNPs nell'indurre l'ipertermia nelle cellule in coltura. Sebbene questi dati siano stati ottenuti in modelli *in vitro*,

suggeriscono l'idoneità di queste NPs come strumenti terapeutici e incoraggiano ulteriori studi per la loro applicazione nel campo biomedico.

## ABSTRACT

In the last years, our group focused on magnetic nanoparticles (MNPs), which are able to induce hyperthermia, as potential biomedical tools. Magnetic hyperthermia is a term used to denote the generation of heat by MNPs in response to the application of an external alternating magnetic field. We applied hyperthermia *in vitro* with different aims and the effects on cells were analyzed by applying viability test and morphological analysis with light and transmission electron microscopy (TEM) techniques.

We used superparamagnetic iron oxide nanoparticles (NPs) to induce delipidation in 3T3L1 adipocytes and human adipose-derived adult stem cells. Immediately after hyperthermia, we observed a drastic intracellular lipid loss that persisted for at least 24h in the absence of cell death, damage or dedifferentiation. These results open interesting perspectives for the application of hyperthermia to treat obesity.

We applied hyperthermic treatment also to cancer cells, known to be more sensitive to heat shock than healthy cells, in order to induce apoptosis. A glioblastoma cell line (U87MG) was treated with either Zn-SPIONs or biomimetic magnetic NPs (BMNPs). Zn-SPIONs are amphiphilic polymer, dodecyl grafted poly(isobutylene-alt-maleic anhydride) coated zinc-doped iron oxide ( $\text{Fe}_3\text{O}_4$ ) NPs of  $15\pm 2$  nm size, and show a high thermal capacity. BMNPs, synthesized with the protein MamC from magnetotactic bacteria, may act as both drug carriers and hyperthermic agents, being promising tools for the treatment of many types of tumor. BMNPs were also tested in a human hepatocyte carcinoma cell line (HepG2) after functionalization with a Choline Kinase inhibitor in order to obtain a nanocarrier potentially suitable for targeted chemotherapy. In fact, Choline Kinase is considered as a biomarker of tumor progression and carcinogenesis, and a target therapy. Therefore, our nanocarriers would allow a local treatment of cancer thus avoiding/reducing possible systemic side effects. The internalization of BMNPs was evaluated using TEM.

Taken together, our results prove the efficacy of MNPs in inducing hyperthermia in cultured cells. Although these basic data have been obtained in *in vitro* models, they suggest the suitability of these NPs as therapeutic tools and encourage further studies for their application in the biomedical field.

**ACRONYMS.....10**

**LIST OF FIGURES.....11**

**I. INTRODUCTION.....14**

- Hyperthermia.....15
- Mechanisms of heat generation.....17
- Characteristics of MNPs for intracellular hyperthermia.....22
- Nanoparticle delivery to the tumor site.....23
- Cellular effects of hyperthermia.....26
- Biophysical and metabolic differences between healthy and cancerous cells.....28
- Nanoparticles used for our in vitro studies.....29
- Magnetic nanosystems for thermo- chemotherapy.....33
- Aim of the work.....36

**II. RESULTS.....37**

*MR Marinozzi, L Pandolfi, M Malatesta, M Colombo, V Collico, P M-J Lievens, S Tambalo, C Lasconi, F Vurro, F Boschi, S Mannucci, A Sbarbati, D Prospero, L Calderan (2017): Innovative approach to safely induce controlled lipolysis by superparamagnetic iron oxide nanoparticles-mediated hyperthermic treatment..38*

**Biomimetic Magnetic Nanocarriers optimization and functionalization**

1. *F Vurro, S Mannucci, M Perduca, C Jiménez Lòpez, M Gerosa, A Busato, MP Carrasco Jiménez, Y Jabalera, M Malatesta, L Calderan: PLGA Encapsulation and TAT peptide Functionalization of Biomimetic Magnetic Nanoparticles Increase their uptake in human brain glioblastoma*

<i>(U87MG) and in mouse embryonic fibroblast (3T3L1) cell lines</i> .....	67
2. <i>Y Jabalera , A Sola-Leyva, A Peigneux , F Vurro, G R. Iglesias, J Vilchez-Garcia, I Pérez-Prieto, F J. Aguilar-Troyano, L C. López-Cara , María P. Carrasco-Jiménez and C Jimenez-Lopez (2019). Biomimetic Magnetic Nanocarriers Drive Choline Kinase Alpha Inhibitor inside Cancer Cells for Combined Chemo-Hyperthermia Therapy</i> .....	52
<i>F. Vurro, S Mannucci, D.Prosperi, P.Das, M Gerosa, A Busato, , M Malatesta, L Calderan: Colloidal polymer-coated Zn-doped iron oxide nanoparticles with high relaxivity and specific absorption rate for efficient magnetic resonance imaging and magnetic hyperthermia</i> .....	76
<b>III. DISCUSSION</b> .....	<b>84</b>
<b>IV. APPENDIX</b> .....	<b>89</b>
<i>Accardo, S. Mannucci, E. Nicolato, F.Vurro, C. Diaferia, P. Bontempi, P. Marzola, G.Morelli (2018). Easy formulation of liposomal doxorubicin modified with a bombesin peptide analogue for selective targeting of GRP receptors overexpressed by cancer cells, Drug Delivery and Translational Research, 9:215–226,</i> .....	92
<i>M. Costanzo, F. Vurro, B. Cisterna, F. Boschi, A. Marengo, E. Montanari, C. Di Meo, P. Matricardi, G. Berlier, B. Stella, S. Arpicco, M. Malatesta(2019). Uptake and intracellular fate of biocompatible nanocarriers in cycling and noncycling cells, Nanomedicine, 14(3):301 316.</i> .....	105
<b>V. BIBLIOGRAPHY</b> .....	<b>123</b>

**AMF:** Alternating magnetic field  
**ATGL:** Transcript expression of adipose triglyceride lipase  
**BMNPs:** Biomimetic magnetic nanoparticles  
**ChoK $\alpha$ 1:** Choline kinase  $\alpha$ 1  
**EPR:** Enhanced permeability and retention  
**ILP:** Intrinsic loss power  
**MAPK:** Mitogen-activated protein kinase  
**MFH:** Magnetic fluid hyperthermia  
**MH:** Magnetic hyperthermia  
**MNPs:** Magnetic nanoparticles  
**MRI:** Magnetic resonance imaging  
**NPs:** Nanoparticles  
**PI3K/AKT:** Phosphoinositide 3-kinase  
**PIOs:** Polyhedral iron oxide nanocrystals  
**PLGA NPs:** Poly(lactic-co-glycolic acid) nanoparticles  
**SAR:** Specific absorption rate  
**SPIONs:** Superparamagnetic iron oxide nanoparticles  
**TAT:** Transactivator of transcription  
**TEM:** Transmission electron microscopy

## LIST OF FIGURES

---

Figure 1. Illustration of the Néel relaxation and the Brownian relaxation (the image has been reproduced from Chengyin Fu, 2012)

Figure 2. Hysteresis loop of a ferromagnet. The area of the hysteresis loop represents the energy dissipated during a magnetisation cycle (the image has been reproduced from Hervault et al., 2014)

Figure 3. Typical curve for a superparamagnetic material (the image has been reproduced from Hervault et al., 2014)

Figure 4. Biomedical applications of magnetic nanoparticles (the image has been reproduced from A Lascialfari et al)

Figure 5. Mechanism responsible for the synergistic effect of the combined therapy (the image has been reproduced from Hervault et al., 2014)

Figure 6. Magnetic nanoparticle-based therapeutic agents for thermo-chemotherapy treatment of cancer

Figure 7. Viability (MTT assay) of Hep-G2 after incubation with Ff35(1 $\mu$ M), BMNPs, Ff35-BMNPs for 2, 24, 48h.

Figure 8. Transmission electron micrographs of BMNPs and Ff35-BMNPs internalization in Hep-G2 cells.

Figure 9. Effects of Ff-35 BMNPs and hyperthermia on Hep-G2 cells viability.

Figure 10. Viability (MTT assay) of 3T3L1 after incubation with different BMNPs concentrations for 2, 24, 48 and 72 h. Asterisks indicate significantly different values ( $P < 0.05$ ) between treated and control samples

Figure 11. Viability (MTT assay) of 3T3L1 after incubation with different PLGA-BMNPs concentrations for 2, 24, 48 and 72 h. Asterisks indicate significantly different values ( $P < 0.05$ ) between treated and control samples

Figure 12. Viability (MTT assay) of 3T3L1 after incubation with different TAT-PLGA -BMNPs concentrations for 2, 24, 48 and 72 h. Asterisks indicate significantly different values ( $P < 0.05$ ) between treated and control samples

## LIST OF FIGURES

---

Figure 13. Viability (MTT assay) of U87MG after incubation with different BMNPs concentrations for 2, 24, 48 and 72 h. Asterisks indicate significantly different values ( $P < 0.05$ ) between treated and control samples

Figure 14. Viability (MTT assay) of U87MG after incubation with different PLGA-BMNPs concentrations for 2, 24, 48 and 72 h. Asterisks indicate significantly different values ( $P < 0.05$ ) between treated and control samples

Figure 15. Viability (MTT assay) of U87MG after incubation with different PLGA-BMNPs concentrations for 2, 24, 48 and 72 h. Asterisks indicate significantly different values ( $P < 0.05$ ) between treated and control samples

Figure 16. Transmission electron micrographs of a human fibroblast treated with nanoparticles for 24 h. a) Clusters of nanoparticles occur both at the surface (arrow) and inside (open arrow) the cell. b) High magnification of the nanoparticles at the cell surface (arrow in a): note the cell protrusion indicating a phagocytic process. c) High magnification of nanoparticles enclosed in a cytoplasmic vacuole (open arrow in a). Bars: 1000 nm (a), 500 nm (b,c)

Figure 17. AMF apparatus (Magnetherm, nanaTherics, UK)

Figure 18. Viability (MTT assay) of HFL1 after incubation with different magnetoliposomes concentrations for 2, 24, 48 h. Asterisks indicate significantly different values ( $P < 0.05$ ) between treated and control samples

Figure 19. Viability (MTT assay) of HFL1 after incubation with different S1 NPs concentrations for 2, 24, 48 and 72 h. Asterisks indicate significantly different values ( $P < 0.05$ ) between treated and control samples. All the concentrations tested induced a significant increase in cell death; consequently, these concentrations were excluded from the subsequent experimentation

Figure 20. Viability (MTT assay) of HFL1 after incubation with different S1 NPs concentrations for 2, 24, 48 and 72 h. Asterisks indicate significantly different values ( $P < 0.05$ ) between treated and control samples. 5  $\mu\text{g/mL}$  and 1  $\mu\text{g/mL}$

## LIST OF FIGURES

---

concentrations induced a significant increase in cell death; consequently, these concentrations were excluded from the subsequent experimentations.

Figure 21. Viability (MTT assay) of U87MG after incubation with different S1 NPs concentrations for 2, 24, 48 and 72 h. Asterisks indicate significantly different values ( $P < 0.05$ ) between treated and control samples. All the concentrations tested induced a significant increase in cell death; consequently, these concentrations were excluded from the subsequent experimentation

Figure 22. Viability (MTT assay) of U87MG after incubation with different S1 NPs concentrations for 2, 24, 48 and 72 h. Asterisks indicate significantly different values ( $P < 0.05$ ) between treated and control samples. 5  $\mu\text{g/mL}$  and 1  $\mu\text{g/mL}$  concentrations induced a significant increase in cell death; consequently, these concentrations were excluded from the subsequent experimentations

Figure 23. Transmission electron micrographs of U87MG cells incubated for 24 hours with S1 nanoparticles. (a) Two nanoparticles are adhering to the cell surface (arrow). (b) A nanoparticle occurs into a cell surface invagination (arrow), while two nanoparticles are enclosed in a small endosome (arrowhead). (c) A large vacuole (thick arrow), probably a secondary lysosome, contains many nanoparticles

Figure 24. (a) Time-dependent temperature curves of polymer-coated Zn-SPIONs at different NPs concentrations in water in presence of an external alternating magnetic field. (b) the calculated specific absorption rate (SAR) of polymer coated Zn-SPIONs as a function of the applied magnetic field

Figure 25. Light microscopy micrographs of U87MG cells. In **a** and **c** the cells were incubated for 24 hours with S1 nanoparticles and then placed in the induction coil without undergoing hyperthermic treatment. In **b** and **d** the cells were incubated for 24 hours with S1 nanoparticles, submitted to hyperthermia and

observed immediately after (**b**) or after 24 h (**d**) from the treatment. Note the high number of dead cells (arrows) in **b** and **d** in comparison to **a** and **c**

## **I. INTRODUCTION**

---

### **Hyperthermia**

Hyperthermia is the procedure of raising the temperature of a part of or the whole body above normal body temperature for a defined period of time. Body temperature variations could interfere with basal metabolisms and homeostasis processes (energetic metabolism, hydro-saline and acid-basic homeostasis). It is clear that adipose tissue plays a critical role in the regulation of lipid and carbohydrate metabolism and that hot conditions are responsible for the alteration of carbohydrate/lipid metabolism and in correlation with lipid metabolism (Bernabucci et al, 2009). Park et al. (2005) reported that the increase of 1-2°C from physiological temperature represents a mild heat shock for the cells, while higher temperatures may lead to severe heat shock. High temperature induce changes in the fluidity of membrane lipids and could cause trasduction of a signal, which would induce cell heat shock response and the activation of several important regulatory proteins. Recently, magnetic nanoparticles proved to affect the expression of obesity and type 2 diabetes mellitus-associated risk genes in human adipocytes, opening interesting perspectives for their use to modulate lipid metabolism.

In cancer care, the term “hyperthermia” refers to the treatment of cancer by administering heat in different ways. Hyperthermia is usually applied in combination with an already established treatment modality (radiotherapy and chemotherapy), where it is necessary to reach temperatures in the range of 40-46°C inside the tumor. Clinical studies have shown that the success of a hyperthermia cancer treatment is related to the minimum temperature rise occurring in the tumor tissue (Moyer et al., 2008), (Lee et al., 2010). The efficacy of hyperthermia treatment is related to the temperature achieved during the treatment, as well as to the lenght of treatment and tissue characteristics (Hegyi et al., 2013). An important challenge is to reduce damages to healthy tissues and other adverse effects; in fact, high temperatures, above 43°C, can kill a great number of tumor cells, but normal tissues are also severely injured under these

## **I. Introduction**

---

conventional hyperthermia treatments; thus, the goal is the development of novel hyperthermia systems that are able to heat tumor cells above 43°C keeping local temperatures under 44°C, avoiding damage to surrounding tissues, and the whole body temperatures under 42°C.

Magnetic fluid hyperthermia (MFH) is a non-invasive technique for cancer therapy and has several advantages compared to traditional hyperthermia therapy (Laurent et al., 2011), (Kumar et al. 2011).

This therapy involves the administration of magnetic nanoparticles as heat mediators into the tumor followed by its exposure to an external alternating magnetic field (AMF). Therefore, the temperature inside the tumor increases and the cells reach the temperature of 42-46 °C resulting in an extremely selective thermal ablation of tumor. This is due to the generation of heat from internalized magnetic nanoparticles under high frequency AMF leading to magnetic energy dissipation for single-domain particles caused by internal Néel fluctuations of the nanoparticle magnetic moment and external Brownian fluctuations (Das et al. 2018). (Figure1).

Magnetic Fluid Hyperthermia (MFH) has been in development for many years but has just recently come into increasing clinical use. Moreover, novel innovations are rapidly increasing the efficacy of the technique. MFH is currently FDA approved in the US, with the completion of stage 1 enrollment of 120 patients. A follow-up single-arm study has been proposed for focal ablation of solid prostate cancer that will be conducted at University of Texas, San Antonio and University of Seattle, Washington (Chandrasekharan et al. 2020).

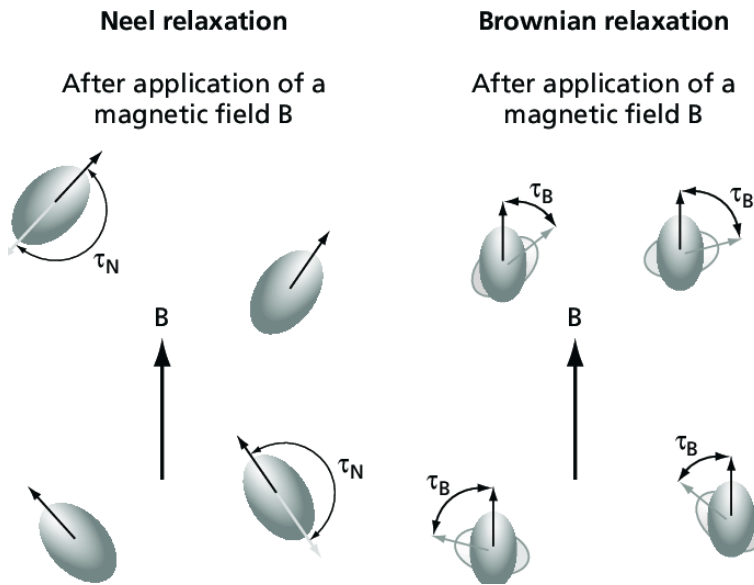


Figure 1. Illustration of the Néel relaxation and the Brownian relaxation (the image has been reproduced from Chengyin Fu, 2012).

### Mechanisms of heat generation

The conversion from magnetic energy to thermal energy in MNPs subjected to an alternating magnetic field can be due to several mechanisms. In multi-domain NPs (ferri- or ferromagnetic material), the production of heat is due to hysteresis losses, which can be seen as the amount of energy dissipated during a magnetisation cycle (Cherukuri et al., 2010). A ferromagnet is formed by magnetic domains (Weiss domains) in which the moments of atoms are all parallel to each other to maintain a lower energy state, while a ferrimagnet is composed by magnetic domains with opposing magnetic moments of different amplitudes. When an external magnetic field is applied, the magnetic domains tend to align themselves in the same direction as the applied field. The saturation magnetisation is reached as soon as each moment of each domain is aligned toward this direction. When the applied field is removed, the magnetisation does not revert back to zero, and this is the so called remaining magnetisation. In order to reduce the magnetisation to zero again, a magnetic field with a precise intensity

## I. Introduction

---

needs to be applied. The magnetisation curve of a ferromagnet is represented by a hysteresis loop (Figure. 2) and the hysteresis losses can be measured by integrating the area of the hysteresis loop. Superparamagnetism is a form of magnetism that occurs in ferromagnetic or ferrimagnetic materials when they are in the form of sufficiently small NPs. Indeed, bulk materials basically contain multiple magnetic domains due to their large size. However, small enough NPs are single-domain particles, which can be regarded as one giant magnetic moment composed of all magnetic moments of the atoms forming the NPs. Superparamagnetic NPs are preferred over ferri- and ferromagnetic NPs for biomedical applications, because they do not retain any magnetisation once the magnetic field is removed (Figure. 3). Single-domain NPs dissipate heat through relaxation losses, which fall in two ways: Neel relaxation and Brownian relaxation. The mechanism of relaxation depends on the size of the NPs but also on the magnetic material (Fortin et al., 2008). Neel relaxation comes from the reorientation of the magnetic moment in the same direction as the applied magnetic field with each field oscillation (Suto et al., 2009), (Kotitz et al., 1999). The Neel relaxation time  $\tau_N$  is given by the following equation:

$$\tau_N = \tau_0 \exp(KV/k_B T)$$

where  $\tau_0 = 10^{-9}$  s, K is the anisotropy constant, V is the volume of the magnetic particle,  $k_B$  is the Boltzmann constant and T is the temperature. Néel relaxation is strongly size-dependent. A smaller particle requires less energy for the rotation of its magnetic moment, consequently the Néel relaxation mechanism will be very important. Brownian relaxation is induced by thermal excitation (Suto et al., 2009), (Kotitz et al., 1999). The Brownian relaxation time  $\tau_B$  is expressed by the following equation:

$$\tau_B = 3\eta V_H / k_B T$$

where  $\eta$  is the viscosity of the liquid carrier,  $V_H$  is the hydrodynamic volume of the particle,  $k_B$  is the Boltzmann constant and T is the temperature.

## I. Introduction

---

The Brownian relaxation mechanism is size-dependent too and also strongly viscosity-dependent (Kotitz et al., 1995). A higher viscosity of the liquid medium will slow down the rotation of the particles. Generally, losses by Néel relaxation prevail in small NPs while the Brownian relaxation dominates in larger NPs (Suto et al., 2009),(Levy et al., 2008). In fact, the Brownian losses are not exclusively found in superparamagnetic NPs (Hergt et al., 2006). For hyperthermia applications, it is better to have NPs relaxing essentially through the Néel mechanism, because when internalised in the cells, a change in the viscosity medium can happen and/or free rotation of the particles can be prevented.

A combination of the two magnetic relaxation times gives the overall effective relaxation time  $\tau$  of the particles:

$$\tau = \tau_B \tau_N / (\tau_B + \tau_N)$$

Application of an AMF oscillating faster than the relaxation time of the MNPs induces the release of heat from the MNPs caused by the delay in the relaxation of the magnetic moment (Suto et al., 2009). The power dissipation (P) is given by the following equation:

$$P = \mu_0 \chi'' f H^2$$

where P is the power dissipation value,  $\mu_0$  is the permeability of free space,  $\chi''$  is the AC magnetic susceptibility, f is the frequency of the applied AC magnetic field, and H is the strength of the applied AC magnetic field. Quantification of the power dissipation of magnetic nanoparticles in an AMF is usually done by measuring the specific absorption rate (SAR) expressed in  $W g^{-1}$  (also referred to as specific loss power) (Suto et al., 2009).

## I. Introduction

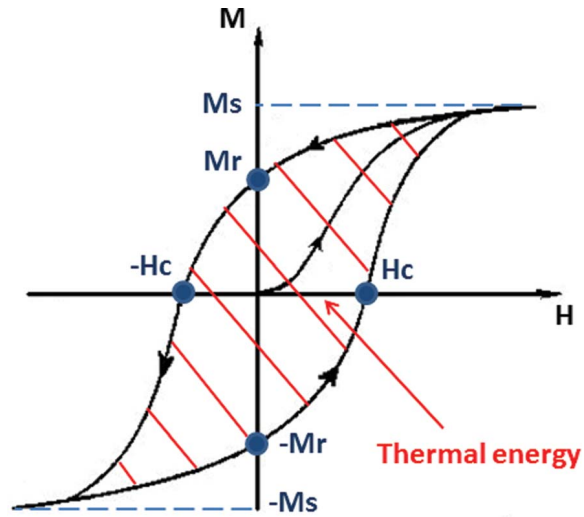


Figure 2. Hysteresis loop of a ferromagnet. The area of the hysteresis loop represents the energy dissipated during a magnetisation cycle (the image has been reproduced from Hervault et al., 2014).

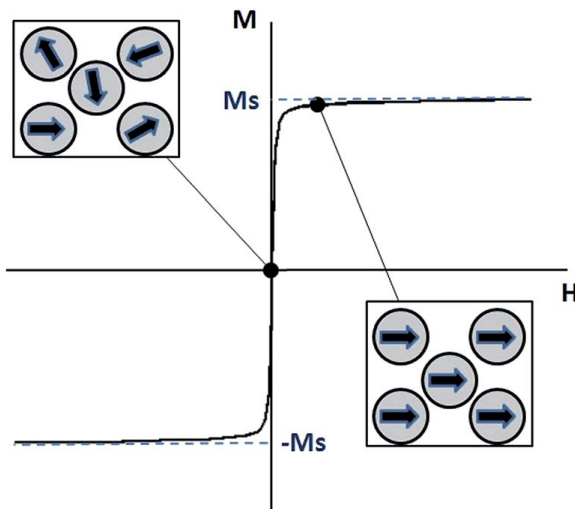


Figure 3. Typical curve for a superparamagnetic material (the image has been reproduced from Hervault et al., 2014)

## I. Introduction

---

$$\text{SAR} = c \left( \frac{dT}{dt} \right) \left( \frac{m_s}{m_m} \right)$$

where  $C$  is the specific heat capacity of the sample,  $dT/dt$  is the initial slope of the time-dependent heating curve,  $m_s$  is the mass of the water and  $m_m$  is the mass of the NPs. SAR highly depends on various parameters such as the size, size distribution, shape, chemical composition and surface modification, saturation magnetisation of the particles; and frequency and amplitude of the applied magnetic field. A high heating potential is crucial for the clinical use of MFH, because it would require a smaller amount of NPs to be injected into the patient. Therefore, it is highly desirable to obtain MNPs with an exceptional SAR value (Sharifi et al., 2012), (Liu et al., 2012). Superparamagnetic NPs, which produce heat via Néel and Brownian relaxation mechanisms, are able to generate a larger quantity of heat and a higher SAR at lower field amplitudes. Hergt et al. suggested that the optimum size to get particles with a high SAR value is near the transition from superparamagnetic to ferromagnetic behaviour (Hergt et al, 2004). SAR values increase with the frequency  $f$  and the field amplitude  $H$  of the applied field. However, in order to safely apply hyperthermia to patients and avoid any damages on healthy tissues due to electromagnetic radiation exposure, the  $Hf$  factor should not exceed a threshold which was experimentally estimated to equal  $5 \times 10^9 \text{ A m}^{-1} \text{ s}^{-1}$  (Hergt et al., 2007). There is a lack of standardized protocol to measure the heating ability of the MNPs. The ideal device for accurate measurement of the SAR would be an adiabatic setup, but most of the research groups use non-adiabatic and often home-made setups which results in more sources of inaccuracies and increased variability of the SAR values (Natividad et al, 2008), (Huang et al., 2012). Also, each research group measures the nanoparticles heating capabilities under different field conditions. Indeed, there are no standards for the frequency and field amplitude of the applied field used during the measurement, which makes the SAR values difficult to compare with

## I. Introduction

---

each other. Pankhurst et al. introduced a new parameter able to allow a more direct comparison of the heating efficiency of superparamagnetic nanoparticles, the intrinsic loss power (ILP) (Kallumadil et al., 2009). The ILP is obtained by normalizing the SAR by the frequency and field amplitude, and is therefore independent of the magnetic field parameters.

### **Characteristics of magnetic nanoparticles for intracellular hyperthermia**

Nanoparticles (NPs) are defined as particles that have one or more physical dimensions under 100 nm. Thanks to their properties, MNPs have been developed as magnetic resonance imaging (MRI) contrast agents, (Hu et al., 2013) and potential new cancer therapies such as magnetic fluid hyperthermia, (Jordan et al., 1997), (Kallumadil et al., 2009) and nanovectors for controlled drug delivery (Banerjee et al., 2007), (Rahimi et al., 2010). NPs can also be designed to combine several therapeutic functions (hyperthermia and drug delivery) (Wang et al., 2012), (Purushotham et al., 2009) or therapeutic and diagnostic functions (so-called theranostics) (Veiseh et al., 2010), (Sanson et al., 2011). Any magnetic particles that can generate heat under an alternating magnetic field can theoretically be used for intracellular hyperthermia. The most important principle, however, is that the magnetic particles are non-toxic. Because of this, magnetite ( $\text{Fe}_3\text{O}_4$ ) and maghemite ( $\gamma\text{-Fe}_2\text{O}_3$ ) have been the focus of most of the studies. Maghemite is produced by the oxidation of magnetite above  $300^\circ\text{C}$  and the steps required to produce magnetite are simpler than those required to produce maghemite. Therefore, most studies of magnetic particles for intracellular hyperthermia have focused on magnetite. Several types of magnetite nanoparticles have been developed for intracellular hyperthermia and the magnetite core sizes range from 5 to 15 nm. In general, magnetic characteristics depend on particle size and on the preparation methods used to produce the magnetic particles. As the particle sizes decrease, multi-domain ferromagnetic characteristics change to single-domain ferromagnetic, and finally, to superparamagnetic characteristics. Magnetic nanoparticles have controllable sizes ranging from a few nanometres up to tens of nanometres. They can be coated with

## **I. Introduction**

---

biological molecules be more biocompatible and to make them interact with or bind to a specific target. Then, the nanoparticles are magnetic and can be manipulated by an external magnetic field gradient. This action, combined with the intrinsic penetrability of magnetic fields into human tissue, opens up many applications involving the transport and/or immobilization of magnetic nanoparticles. In this way, they can be made to deliver an anticancer drug to a targeted region of the body, such as a tumour. Magnetic nanoparticles can be made to respond to a time-varying magnetic field, with advantageous results related to the transfer of energy from the exciting field to the nanoparticle. For example, the particle can be made to heat up, which leads to their use as hyperthermia agents, delivering toxic amounts of thermal energy to the target such as a tumour; or as chemotherapy and radiotherapy enhancement agents, where tissue warming results in more effective malignant cell destruction. These, and many other potential applications, could be available in biomedicine as a result of the physical properties of magnetic nanoparticles (Corato et al., 2015), (Cazares-Cortes et al., 2018).

### **Nanoparticle delivery to the tumor site**

MNPs must be delivered to the target body site and should be kept in the tumor in order to reach a sufficient concentration to be an efficient hyperthermic agent. There are three different approaches for the delivery of NPs:

1. *Intratumoral injection*, which consists in injecting the NPs into the tumour. This is the easiest way to administer NPs and has already been used in clinical trials of MFH (Maier-Hauff et al., 2007), (Johannsen et al., 2005). The main advantage of this approach is that it is easy to reach a high concentration of MNPs in the tumour. However, it is possible to use this technique only in the case of an easily accessible and localized tumour. Moreover, direct injection results in a non-homogeneous MNPs distribution in the tumour (Huang et al., 2013).

2. *Systemic delivery* which is achieved by injecting MNPs intravenously that will accumulate preferentially in the tumour tissue due to enhanced permeability and retention (EPR) effect, (Acharya et al., 2011). The EPR relies on specific pathophysiological characteristics of tumors in comparison to healthy tissues. In healthy tissues, low-molecular-weight drugs easily extravasate out of blood vessels, while nanoparticles are unable to do so, because of their size. Instead, in tumors, the abnormally wide fenestrations in the blood vessels allow the extravasation of materials with sizes up to several hundreds of nanometers. This, together with the absence of lymphatic drainage, leads to a relatively effective and selective accumulation of nanocompounds in tumors (Torchilin et al., 2011). Within the last couple of years, scientists have increasingly realized that the EPR effect is highly heterogeneous, changing over time during tumor development and possibly also being transient. This pathophysiological phenomenon does not only vary between mouse models and patients, but also among tumor types of the same origin, and among tumors and metastasis within the same patient (Harrington et al., 2001).

As a consequence, the clinical outcome of nanomedicine treatments is also highly heterogeneous, and not as good as anticipated on the basis of preclinical results (Maeda et al., 2018).

The notion that the EPR effect strongly varies between individuals is of high importance, and may lead to misunderstandings and to a too pessimistic view on EPR-mediated passive tumor targeting. To facilitate the translation of nanomedicine to the clinic, and to allow individual and improved anticancer nanomedicine therapies, it is crucial to get a better knowledge of the heterogeneity of the EPR effect in patients. Therefore, EPR-potentiating combination treatments, as well as diagnostic protocols, which are able to visualize and quantify the extent of the EPR-mediated tumor targeting in individual patients, are urgently needed (Greish et al., 2018).

## I. Introduction

---

To take advantage of the EPR effect, the MNPs should be able to circulate long enough in the blood stream. For this purpose, NPs should have a hydrodynamic diameter smaller than 200 nm to avoid liver clearance and bigger than 50 nm to avoid renal clearance (Krishnan et al., 2010). The coating of the NPs can also play an important role in the permeability and retention of the NPs in cancer cells, as well as in the blood retention time of the NPs. Finally, NPs have to be stable in the biological medium to avoid aggregation and keep the hydrodynamic size, which ensures them a long blood circulation time. The systematic delivery of NPs via the EPR effect results in a more homogeneous distribution of the MNPs in the tumour in comparison to an intratumoural injection, and allows also the treatment of most of the types of cancers. However, the principal drawback of this method is the difficulty to reach a concentration of NPs sufficient enough for effective treatment. Although the amount of NPs injected can not be further increased, in order to avoid not-negligible MNP toxicity and to achieve higher deposition and improve tumour uptake of the NPs, they can be driven magnetically inside the body via an external magnetic field and/or can be functionalised with a targeting ligand for active delivery. Active delivery consists of improving the specificity of the NPs functionalising their surface. It usually results in a higher NP accumulation and cellular uptake in the targeted cancer cells. Among the most commonly used targeting agents, we can find antibodies, antibody fragments, receptor ligands, peptides and aptamers.

3. Another targeting system, which can be used to improve the accumulation of MNPs into the tumour site, is *magnetic targeting*. This technique uses an external magnetic field placed near the tumour to magnetically attract the NPs toward this area. Magnetic targeting has already shown efficiency in *in vivo* studies (Fortin-Ripoche et al., 2006), (Fulauf et al., 2013).

### **Cellular effects of hyperthermia**

Hyperthermia may kill or weaken tumor cells and is controlled to limit effects on healthy cells. Hyperthermia may therefore cause cancerous cells to undergo apoptosis in direct response to applied heat, while healthy tissues can more easily maintain a normal temperature. (Hegyí et al., 2013). Increased temperature kills cancer cells through various direct mechanisms: cell cycle arrest, apoptosis, necrosis and autophagy.

It was demonstrated that hyperthermia in the 40-47°C temperature range kills cells in a reproducible time and temperature dependent manner. The changes induced by hyperthermia at cellular level must be due to temperature-induced alterations in molecular pathways, which usually involve inhibition of DNA, RNA, and protein synthesis (Laszlo, 1991). However, while protein synthesis is inhibited during heating at higher temperatures, at milder temperatures and after return to normal growth temperature the induction of heat shock proteins occurs (Kregel et al, 2002), which is an inducing event and closely associated with the induction of thermotolerance. Thus, heat shock can lead to both inactivating and activating responses. During apoptosis, also called programmed cell death, the cells in normal tissues trigger their self-destruction in response to a signal (Kerr et al., 1994). Contrary to the necrosis, there is no associated inflammation. Apoptosis also occurs spontaneously in cancer cells, thereby slowing the tumour growth, and can be increased when subjected to heat, irradiation or anti-cancer drugs. In contrast to apoptosis that is a natural process, necrosis is a form of cellular damage that results in the premature death of cells in body tissues and causes an inflammatory response in the surrounding environment (Golstein et al., 1999). Thus, thermoablation in this temperature range is not the best option due to the potentially important side effects on healthy tissues, and hyperthermia induced apoptosis is therefore preferable. The thermal energy needed to induce cell death has been found to be close to the energy needed for protein denaturation, leading

## **I. Introduction**

---

to the conclusion that the main cytotoxic effect of hyperthermia is based on the denaturation of membrane and cytoplasmic proteins (Hildebrandt et al., 2002), (Lepock et al., 2003). Membrane alteration and cytoskeletal damage such as cell rounding and blebbing (which is a typical feature of apoptosis) are some of the most apparent manifestations of thermal damage at cellular level. Another important consequence of protein denaturation is the alteration of DNA synthesis and repair. Higher sensitivity to heat has been observed for cells in the mitosis phase (with damage to the mitotic apparatus), which makes cancer cells more susceptible to heat than normal cells as they undergo faster cell division. The tumour selective effect of hyperthermia is also due to the physiological differences between normal and tumour tissues. Indeed, the architecture of the vasculature in tumour is disorganised and abnormal compared to normal tissue (one of the principal features is the lower vessel density and capillaries organization). In many cases, tumour blood flow remains greater than in the surrounding healthy tissues, especially in small tumours (tumour blood flow generally decreases with increasing tumour size)(Song et al., 1984). However, when hyperthermia is applied at temperatures over 42 °C, tumour blood flow tends to decrease while in normal tissue it significantly increases. This decreased blood flow results in a lower heat dissipation rate, and hence the temperature in a tumour will rise faster than in normal tissue. This difficulty in dissipating heat may cause cancer cells to undergo apoptosis, while physiological temperatures are more easily maintained in normal tissues.. The disorganised structure of tumour vasculature also leads to oxygen and nutrient deprivation (Siemann et al., 2011). Moreover, regions of hypoxia, energy deprivation and acidosis are even more favoured with the reduction of the blood flow caused by heat exposure (Hildebrandt et al., 2002). These tumour micro-environmental factors also make cancer cells more sensitive to hyperthermia, in addition to its direct cytotoxicity. In fact, hyperthermia may increase or decrease the tumour oxygenation depending on the temperature and the exposure time (Song et al., 2001).

## I. Introduction

---

Hyperthermia applied at temperatures lower than 42 °C is more likely to induce an increase in the tumour blood flow, thereby improving the oxygen supply. This phenomenon can be exploited to make cells more sensitive to radiotherapy (radio- sensitivity is favoured by good tissue oxygenation) or chemotherapy (drug delivery is increased by higher perfusion)(Hildebrandt et al., 2002),(Wust et al., 2002).

### **Biophysical and metabolic differences between healthy and cancerous cells**

The electric properties of the tumor cells differ from normal cells, and the main differences are:

- The capacity of the ATP production in tumor cells is slow. The large ATP request for the proliferative energy consumption allows less ATP for active membrane stabilization by  $K^+$  and  $Na^+$  transport; so the membrane potentiating weakens.
- The cellular membrane of tumor cells is electrochemically different from the normal and its charge distribution also deviates.
- The membrane of the tumor cell differs in its lipid and sterol content from the healthy cells.
- In consequence of the change in the membrane permeability, the efflux of  $K^+$ ,  $Mg^{2+}$  and  $Ca^{2+}$  ions increases, while the efflux of  $Na^+$  decreases together with the water transport from the cell. Consequently, the cell swallows, its membrane potential decreases further (the efflux of  $K^+$  regulates the pH of the cell and takes the protons out of the cytosol). The concentration of  $Na^+$  increases in the cytosol and the negative ion-concentration also grows on the glycocalix shell, decreasing the membrane potential and the tumor will be negatively polarized in average.
- The conductivity and the dielectric constant of the tumor tissue will be higher than normal.

## **I. Introduction**

---

Hyperthermia may therefore cause cancerous cells to undergo apoptosis in direct response to applied heat, while healthy tissues can more easily maintain a normal temperature. Even if cancerous cells do not die, they may become more susceptible to ionizing radiation therapy or chemotherapy, which may allow to use lower doses of drugs. Neoplastic cells do not have a defense system against heat, as normal cells do. Normal cells often express heat shock-induced proteins whose functions are the reactivation of denatured proteins, the degradation of abnormally structured proteins, the inhibition of secretion of abnormal proteins and assisting the transfer of secretory proteins by blockage of folding; normal cells thus can survive in unfavorable circumstances (Ellis et al. 1991).

### **Nanoparticles used for our in vitro studies**

#### **SPIONs**

Because of their numerous advantages, MNPs and especially iron oxide NPs, which have been approved by US Food and Drug Administration, have gained great interest for their applications in biomedicine (Thuy et al., 2012). Indeed, iron oxide NPs are relatively easy to synthesise, biocompatible, non-toxic, chemically stable and can be superparamagnetic. The two main forms of iron oxide are  $\gamma$ - $\text{Fe}_2\text{O}_3$  (maghemite) and  $\text{Fe}_3\text{O}_4$  (magnetite). The phenomenon of local or general rise of the body temperature above its normal value is known as hyperthermia. It can be used as a medical treatment, called hyperthermia therapy or thermotherapy, in which body tissues are exposed to slightly higher temperatures in order to damage or kill cancer cells by inducing cell apoptosis or to make cancer cells more sensitive to the effects of radiation (van der Zee et al., 2002) and/or certain anti-cancer drugs (Issels et al., 2008). Recently, SPIONs proved to affect the expression of obesity and type 2 diabetes mellitus-associated risk genes in human adipocytes (Sharifi et al., 2013), opening interesting perspectives for their use to modulate lipid metabolism. Polyhedral iron oxide nanocrystals (PIOs) were used in vitro studies as hyperthermic mediators in order to test their efficacy in

## I. Introduction

modulating cellular lipid content as a novel strategy to counteract obesity. SPIONs are versatile NPs that can be administered by different routes among which ingestion and transdermal application (Santini et al., 2015). Another important characteristics of these NPs is that PIONs surface can be functionalized and their distribution can be controlled by targeting strategies, thus focusing the hyperthermic treatment in specific tissues.

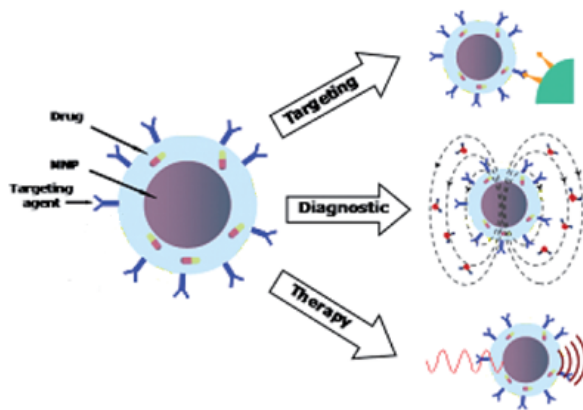


Figure 4. Biomedical applications of magnetic nanoparticles (the image has been reproduced from A Lascialfari et al.)

### Biomimetic magnetic nanoparticles (BMNPs)

Among the potential nanocarriers, magnetic nanoparticles are preferred because of their biocompatibility and their magnetic properties, which allow to reach the target site by the application of external magnetic field and allow the nanoparticle itself to be used as hyperthermia agent (Prozorov et al., 2013). BMNPs mediated by *Magnetococcus marinus* MC-1 magnetosome membrane protein MamC, are promising nanocarriers, able to couple with drugs forming stable nanoassemblies at physiological pH, while efficiently releasing the drug in acidic environments (like tumor one) in response to pH changes. BMNPs present novel features compared to other NPs produced inorganically (García Rubia et al., 2018):

## **I. Introduction**

---

- They are superparamagnetic(single magnetic domain) at room and body temperature.
- They present a large magnetic moment per particle under the influence of an external magnetic field, optimizing their guidance and concentration at the target site.
- They are cytocompatible and produced by means of cost effective, easily scalable method.

BMNPs were tested on a glioblastoma cell line. In order to improve the biocompatibility of these NPs, avoid their oxidation and improve their efficiency to reach the target site, they were enclosed in PLGA-based NPs (50%Lactic acid and 50% Glycolic acid) and functionalized with transactivator of transcription (TAT) peptide. TAT peptide is derived from human immunodeficiency virus and is a cell-penetrating peptide. Cell-penetrating peptides have been used to overcome the lipophilic barrier of the cellular membranes and deliver large molecules and even small particles inside the cell for biological actions.

BMNPs were functionalized with a ChoK $\alpha$ 1 inhibitor with the goal of obtaining a potential nanoassembly suitable for a targeted chemotherapy that avoids possible side effects related to the inhibition of the choline uptake. Moreover, the simultaneous use of hyperthermia is explored to optimize the effect of the targeted chemotherapy in terms of increasing the cytotoxic effect of the nanoassembly. The in vitro antitumor activity and the internalization of these complexes are investigated in the human hepatoblastoma cell line, HepG2 (Jabalera et al., 2019).

## **I. Introduction**

---

### **Colloidal polymer-coated Zn-doped iron oxide nanoparticles**

At present, the most commonly investigated magnetic heat mediators are superparamagnetic SPIONs, which convert magnetic energy to thermal energy through Brownian-Néel relaxations and hysteresis losses. (Das et al., 2019), (Hervault et al., 2014).

Nowadays, SPIONs-based magnetic hyperthermia(MH) is clinically approved in Europe as an adjuvant therapy for recurrent glioblastoma multiforme and several clinical trials are still ongoing for other cancer types (Mahmoudi et al., 2018), (Chang et al., 2018).

However, the low magnetic properties of nanoparticles available for preclinical and clinical studies cause poor heating efficiency, leading to a low SAR. As a result, very high dosages of SPIONs are needed to obtain high performances in cancer therapy. In order to contribute overcoming the clinical limitations reported both for MRI and MH, an efficient SPIONs-based theranostic nanosystem with superior magnetic properties was developed for glioblastoma cell treatment. Iron (III) ions in the tetrahedral sites of inverse spinel structure of  $\text{Fe}_3\text{O}_4$  were partially replaced by non-magnetic zinc(II) ions(Noh et al., 2017), (Abenojar et al., 2016). Then, the synthesized non-spherical zinc-doped superparamagnetic iron oxide nanoparticles (Zn-SPIONs) were successfully coated with an amphiphilic polymer producing water dispersible nanoparticles that exhibited high colloidal stability in biological media. This biocompatible nanoconstruct was designed to efficiently interact with glioblastoma cells, demonstrating both contrast agent as well as heat mediator capabilities.

## I. Introduction

### Magnetic nanosystems for thermo- chemotherapy

The application of hyperthermia enhances chemotherapy effects. Several mechanisms are involved in this thermal enhancement, such as increased antineoplastic drug accumulation in tumours and enhanced drug cytotoxicity (improved intracellular uptake of drugs and increased sensitivity of cells to drugs) (Rao et al., 2010). The first one is due to the physiological effect of mild hyperthermia on tumour vasculature, including an increased blood flow, perfusion, and blood vessel pore size of the already leaky tumour vasculature. All these factors help drug extravasation in tumor tissues. The mechanisms responsible for the enhanced drug cytotoxicity are not yet fully understood, but generally involve improved intracellular uptake of drugs due to increased cell membrane permeability, inhibition of DNA-repair of the chemically induced lethal or sublethal damage, and acceleration of the cytotoxic chemical reaction in the case of alkylating or platinum-based antineoplastic agents at elevated temperatures (Issels et al., 2008).

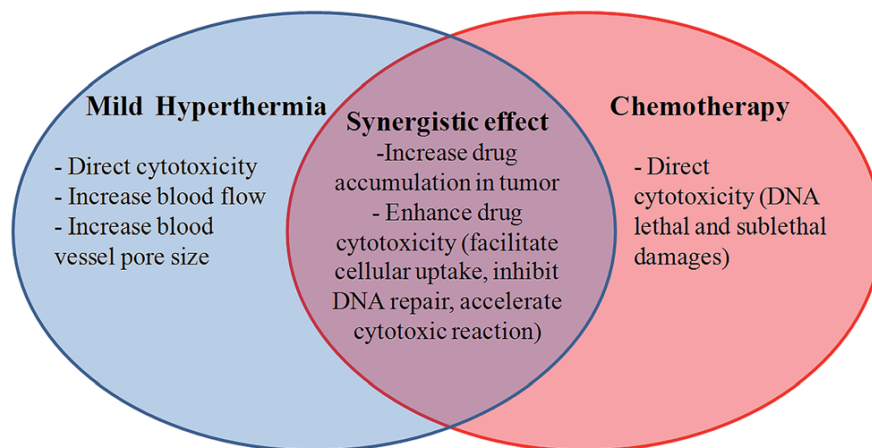


Figure 5. Mechanism responsible for the synergistic effect of the combined therapy (the image has been reproduced from Hervault et al., 2014)

## **I. Introduction**

---

Anti-cancer agents are highly cytotoxic for both cancer and healthy tissues, hence the controlled release of drugs in a localized area would be an important achievement in chemotherapy, as it would minimize the side effects and would reduce the amount of drug used in therapy. This could become possible using nanoparticles for drug delivery. Different nanoformulations incorporating both MNPs and drugs have been created for the purpose of thermo-chemo-therapy (Figure4). A growing area in drug and gene delivery is the use of stimuli-responsive compounds, and especially thermosensitive polymers, to trigger the release of drugs (Ward et al., 2011). The use of MNPs for local hyperthermia is therefore particularly relevant for this aim. Indeed, heat produced by the MNPs under application of an AMF will trigger the release of the drug, and increase the efficacy of the treatment due to the synergistic effect of the simultaneous application of hyperthermia and chemotherapy. The incorporation of MNPs also offers the possibility of guiding the magnetic nanosystems in the body to target the tumour applying a static external magnetic field. Stimuli-responsive polymers, also called smart polymers, have the ability to change properties in response to a change in their environment such as the temperature, pH, light, magnetic field (Theato et al., 2013). Thermo-responsive polymers respond to temperature: they undergo a conformational change at a specific temperature, called the lower critical solution temperature; pH-responsive polymers are also often exploited for drug delivery applications because of the pH changes found in the human body. The pH in the tumour environment is often more acidic than the pH in the blood or healthy tissue. pH-sensitive drug delivery systems can target the tumour site and release the drug due to the pH difference. Hence, hyperthermia and chemotherapy therapeutic functions may be combined in the same nanosystem taking advantage of the great potential of MFH and controlled drug delivery in the treatment of cancer.

## I. Introduction

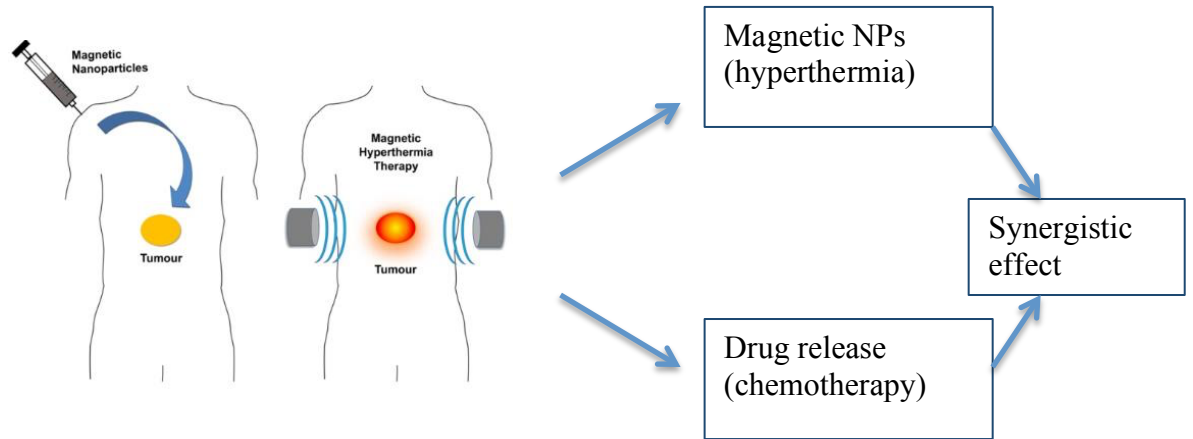


Figure 6. Magnetic nanoparticle-based therapeutic agents for thermo-chemotherapy treatment of cancer.

### Aim of the work

During my doctoral program, I focused my attention on MNPs which were used to induce hyperthermia *in vitro* by applying an external alternating magnetic field. As already reported different MNPs were tested *in vitro* and hyperthermia was applied with different aims. U87MG glioblastoma cells were treated with either Zn-SPIONs or biomimetic MNPs (BMNPs). Iron oxide NPs were used to induce delipidation in 3T3 adipocytes and human adipose-derived adult stem cells. BMNPs, synthesized from magnetotactic bacteria, may act as both drug carriers and hyperthermic agents. They were successfully tested also on a Hep-G2 human hepatocyte carcinoma cells after functionalization with a Choline Kinase inhibitor (this chemical modification would allow the local treatment of cancer, avoiding possible systemic side-effects). Therefore, the main goal of my work was to find efficient hyperthermic nanoparticles for different biomedical applications.

To this aim:

1. The suitability of different MNPs was tested *in vitro* on established cell lines;
2. Their thermic profile was verified and quantified;
3. NPs were optimized and functionalized to improve their biocompatibility and uptake
4. Their efficacy in inducing cell delipidation or death was verified with hyperthermic treatments on cells

The studies on the relationships between MNPs and the biological environment were mainly performed by light microscopy and transmission electron microscopy.

## **II. RESULTS**

---

## II. Results

---

Overweight and obesity are involved in the pathogenesis and worsening of several diseases, such as type 2 diabetes mellitus, stroke, heart and liver disease and cancer. Moreover, obesity causes inflammatory states (De Pergola and Silvestris, 2013). At present, the reduction of adipose tissue is obtained by different invasive and non-invasive techniques and pharmacological agents have serious side effects. It is known that heat shock produces alterations in white adipose tissue metabolism leading to a release of glycerol and fatty acids (Bernabucci et al., 2009). Among the available NPs for thermotherapy, superparamagnetic iron oxide NPs (SPIONs) are becoming very popular because they are able to produce heat when submitted to an alternating magnetic field (Jordan et al., 1993; Mannucci et al. 2014) and they have already been approved for human use by FDA. Recently SPIONs proved to be efficient for the expression of obesity and type 2 diabetes mellitus-associated risk genes in human adipocytes (Sharifi et al. 2013), suggesting their use to modulate lipid metabolism. In our study, we demonstrate that, under appropriate administration conditions, polyhedral iron oxide nanoparticles (PIOs) are efficiently and safely internalized by 3T3 cell line-derived adipocytes (3T3 adipocytes) *in vitro*. Since these nanoparticles proved to generate heat when subjected to alternating magnetic field, 3T3 adipocytes were submitted to magnetic fluid hyperthermia, in order to cause a controlled lipid reduction. The treatment resulted in a significant delipidation persisting for at least 24 h, and in the absence of cell death, damage or dedifferentiation. Interestingly, transcript expression of adipose triglyceride lipase (ATGL), a key gene involved in lipolysis, was not modulated upon MFH, suggesting the involvement of a novel/ alternative mechanism in the effective lipolysis observed. By applying the same experimental conditions successfully used for 3T3 adipocytes, MFH was able to induce delipidation also in primary cultures of human adipose-derived adult stem cells. The success of this approach *in vitro* suggests the application of MFH *in vivo* as an innovative safe and physiologically mild strategy against obesity, potentially useful in association with balanced diet and healthy lifestyle.

*MR Marinozzi, L Pandolfi, M Malatesta, M Colombo, V Collico, P M-J Lievens, S Tambalo, C Lasconi, F Vurro, F Boschi, S Mannucci, A Sbarbati, D Prospero, L Calderan (2017): Innovative approach to safely induce controlled lipolysis by superparamagnetic iron oxide nanoparticles-mediated hyperthermic treatment. The International Journal of Biochemistry & Cell Biology DOI: 10.1016/j.biocel.2017.10.013*



Contents lists available at ScienceDirect

International Journal of Biochemistry  
and Cell Biologyjournal homepage: [www.elsevier.com/locate/biociel](http://www.elsevier.com/locate/biociel)

Research paper

Innovative approach to safely induce controlled lipolysis by  
superparamagnetic iron oxide nanoparticles-mediated hyperthermic  
treatment

Maria Rosaria Marinozzi<sup>a</sup>, Laura Pandolfi<sup>b</sup>, Manuela Malatesta<sup>a</sup>, Miriam Colombo<sup>b</sup>,  
Veronica Collico<sup>b</sup>, Patricia Marie-Jeanne Lievens<sup>a</sup>, Stefano Tambalo<sup>a,d</sup>, Chiara Lasconi<sup>a</sup>,  
Federica Vurro<sup>a</sup>, Federico Boschi<sup>c</sup>, Silvia Mannucci<sup>a</sup>, Andrea Sbarbati<sup>a</sup>, Davide Proserpi<sup>b,\*</sup>,  
Laura Calderan<sup>a,\*</sup>

<sup>a</sup> Dipartimento di Neuroscienze, Biomedicina e Movimento, Università di Verona, 37134 Verona, Italy<sup>b</sup> Dipartimento di Biotecnologie e Bioscienze, Università di Milano-Bicocca, 20126 Milano, Italy<sup>c</sup> Dipartimento di Informatica, Università di Verona, 37134 Verona, Italy<sup>d</sup> Center for Neuroscience and Cognitive Systems @UniTn, Istituto Italiano di Tecnologia, 38068 Rovereto, Italy

## ARTICLE INFO

## Keywords:

Lipolysis  
Obesity  
Magnetic hyperthermia  
Polyhedral iron oxide nanoparticles  
Nanomedicine

## ABSTRACT

During last years, evidence has been provided on the involvement of overweight and obesity in the pathogenesis and aggravation of several life-threatening diseases. Here, we demonstrate that, under appropriate administration conditions, polyhedral iron oxide nanoparticles are efficiently and safely taken up by 3T3 cell line-derived adipocytes (3T3 adipocytes) *in vitro*. Since these nanoparticles proved to effectively produce heat when subjected to alternating magnetic field, 3T3 adipocytes were submitted to superparamagnetic iron oxide nanoparticles-mediated hyperthermia treatment (SMHT), with the aim of modulating their lipid content. Notably, the treatment resulted in a significant delipidation persisting for at least 24 h, and in the absence of cell death, damage or dedifferentiation. Interestingly, transcript expression of adipose triglyceride lipase (ATGL), a key gene involved in canonical lipolysis, was not modulated upon SMHT, suggesting the involvement of a novel/alternative mechanism in the effective lipolysis observed. By applying the same experimental conditions successfully used for 3T3 adipocytes, SMHT was able to induce delipidation also in primary cultures of human adipose-derived adult stem cells. The success of this pioneering approach *in vitro* opens promising perspectives for the application of SMHT *in vivo* as an innovative safe and physiologically mild strategy against obesity, potentially useful in association with balanced diet and healthy lifestyle.

## 1. Introduction

Overweight and obesity represent a major risk factor for human health with prevalent incidence in, although not restricted to, developed countries (Ogden et al., 2007; Report of a WHO Consultation on Obesity, 2000). Several life-threatening diseases, including type 2 diabetes mellitus, stroke, heart and liver disease, and cancer have been associated to body overweight and account for a relevant proportion of morbidity and mortality (De Pergola and Silvestris, 2013; Ahima and Lazar, 2013; Bhaskaran et al., 2014; Renehan et al., 2015; Klil-Drori et al., 2017). In addition, obesity promotes inflammatory states and orthopedic impairments leading to chronic and painful general disorders (Lerner et al., 2016; Bjorge et al., 2008). Although epidemiological evidence is convincing, mechanisms mediating the adverse

metabolic effects of obesity remain only partially elucidated, multiple factors have been suggested, including elevated release of free fatty acids from adipocytes, modified spectrum of adipose tissue secreted endocrine factors (adipokines) or induction of low-grade pro-inflammatory state. Excessive lipid accumulation in adipocytes is a central feature of obesity and metabolic syndrome. Excess energy is primarily stored as triacylglycerol in the lipid droplets of mammalian adipose tissue, and these triacylglycerol reserves are hydrolyzed to supply fatty acids to various tissues by a process called lipolysis. To control lipid mobilization there are numerous lipid droplet-associated proteins such as perilipin, hormone sensitive lipase (HSL), adipose triglyceride lipase (ATGL), that play important roles in regulating fat storage and mobilization (Brasaemle, 2007; Granneman and Moore, 2008; Granneman et al., 2009; Hashimoto et al., 2012). White adipose

\* Corresponding authors: Laura Calderan and Davide Proserpi

E-mail addresses: [davide.proserpi@unimib.it](mailto:davide.proserpi@unimib.it) (D. Proserpi), [laura.calderan@univr.it](mailto:laura.calderan@univr.it) (L. Calderan).<sup>1</sup> Equal contribution.<http://dx.doi.org/10.1016/j.biociel.2017.10.013>

Received 20 July 2017; Received in revised form 19 October 2017; Accepted 23 October 2017

Available online 27 October 2017

1357-2725/© 2017 Elsevier Ltd. All rights reserved.

tissue is an energy storage, endocrine and immune organ consisting of several cell types including mature adipocytes and the stromal vascular fraction (pre-adipocytes, fibroblasts, vascular endothelial cells and a variety of immune cells), all interspersed by a cytokine-rich extracellular matrix and blood vessels (Hassan et al., 2012). White adipose tissue has different anatomical districts in the body and different chemical composition (different polyunsaturation degree and hydrophilic ratio) (Calderan et al., 2006), and this fact entails distinct roles related also to the cross talk with the closed tissues.

Mature adipocytes are highly metabolically active cells containing a single large lipid droplet forcing the nucleus to be squeezed into a thin rim at the periphery. Because of their endocrine function, these cells can directly affect the physiologic processes in neighboring and distant cells by activating paracrine and endocrine pathways through an increase in adipokines and cytokines production (Hotamisligil et al., 1995; Hajer et al., 2008).

The growth of adipose tissue may be due to either an increase in the volume of preexisting adipocytes (hypertrophy) or an excessive number of adipocytes (hyperplasia) (Rutkowski et al., 2015); both processes result in a dysregulation in circulating hormones that affects systemic energy balance and activates macrophage and monocyte migration inducing local inflammation (Xu et al., 2003). As a consequence, the accumulation of adipose tissue is a critical predictor of metabolic disorders, such as insulin resistance, hyperinsulinemia, elevated triglyceride levels, low HDL-cholesterol and hypertension (Arner et al., 2010; Jo et al., 2009).

At present, the reduction of adipose tissue is obtained by different invasive and non-invasive techniques, including bariatric surgery, liposuction, laser, ultrasounds, cryo-lipolysis, and radiofrequency. However, surgical removal of fat could have “esthetic” effects but does not change the energy balance equation (Lambert et al., 1991; Kopelman, 1997). Pharmacological agents, including amphetamine, orlistat, rimonabant, and sibutramine are also used in the management of obesity, but most of these drugs have serious side effects (Renehan et al., 2015). Several studies proved that heat shock produces alteration in energy metabolism of white adipose tissue resulting in the release of glycerol and fatty acids (Bernabucci et al., 2009).

Among the available heat mediators for thermotherapy, superparamagnetic iron oxide nanoparticles (SPIONs) are becoming increasingly popular. Taking advantage of the unique magnetic properties of magnetite at the nanoscale, these nanoparticles are able to produce heat when subjected to an alternating magnetic field (AMF) (Jordan et al., 1993; Lee et al., 2011; Guardia et al., 2012; Lartigue et al., 2012; Mannucci et al., 2014; Orlando et al., 2016). SPIONs have already been approved for human use by FDA due to their good biodegradability (Colombo et al., 2012), and SPION-mediated magnetic hyperthermia (SMHT) has been experimentally applied to cancer cells with promising results (Johannsen et al., 2007; Maier-Hauff et al., 2007; Matsumine et al., 2007).

Recently, SPIONs proved to affect the expression of obesity and type 2 diabetes mellitus-associated risk genes in human adipocytes (Sharifi et al., 2013), opening interesting perspectives for their use to modulate lipid metabolism.

Based on these data, in the present study we investigated the effectiveness of SMHT in modulating cellular lipid content using an *in vitro* model of 3T3 cell line-derived adipocytes (3T3 adipocytes), and provide evidence that SMHT may promote a controlled lipid reduction without causing cell damage, thus pointing to SMHT as an innovative strategy to safely counteract obesity. In addition, we proved the suitability of our SPIONs for primary cultures of human adipose-derived adult stem (hADAS) cells.

## 2. Materials and methods

### 2.1. Synthesis and characterization of SPIONs

Polyhedral iron oxide nanocrystals (PIOs) were synthesized by solvothermal decomposition starting from iron-oleate complex. Iron-oleate

(80 mmol) was dissolved in 200 g of 1-octadecene at room temperature and 5.7 g of oleic acid (20 mmol) were added. The reaction mixture was heated to 110 °C for 1 h to remove solvent humidity, then raised to 200 °C and maintained at this temperature for additional 2 h. Next, the temperature was gradually raised (3 °C/min) to reflux (320 °C) and refluxed for 2.5 h. The dark solution was finally cooled to room temperature, diluted with ethanol (100 mL) and centrifuged. The precipitate was washed several times with a mixture of hexane/acetone and the polyhedral magnetite nanoparticles were collected and dispersed in chloroform. A PMA amphiphilic polymer, namely the poly(isobutylene-alt-maleic anhydride)-graft-dodecyl (Pellegriano et al., 2004; Lin et al., 2008; Mazzucchelli et al., 2013) (252 µL of 0.5 M in chloroform) was added to PIOs (18.5 mg). After removing the organic solvent by rotary evaporator, sodium borate buffer (5 mL of sodium borate buffer (SBB) pH 12) was added obtaining a stable colloidal dispersion that was concentrated by centrifugation at 3500 rpm (10 min). The resulting water-soluble nanoparticles (PIOs) were washed twice with deionized water (5 min at 3500 rpm) and suspended in distilled water. The carboxylate functionalities of PMA were partly labelled with the fluorescent dye fluoresceine amine (FA), limited to the experiments in which fluorescent labeling was required.

Fluorescent PMA was obtained by conjugation of 0.5 M PMA solution in CHCl<sub>3</sub> (5 mL) with 1.0 M FA (0.5 mL dimethylsulfoxide, DMSO).

Hydrodynamic size and surface charge of nanoparticles were measured using a Malvern Zetasizer Nano ZS ZEN3600 (Worcestershire, UK) operating at a λ of 633 nm and a fixed scattering angle of 173°. The sample concentration was adjusted to keep attenuator values between 7 and 9. The refractive index was 1.524. The measurements were performed in triplicate after dilution with MilliQ® water.

Hyperthermic efficiency of nanoparticles. Hyperthermic properties of PIOs were determined by calorimetric measures on samples exposed to an AMF with frequency 521 kHz and strength 25 mT (Magnetherm, NanoTherics Ltd, UK). Samples (10 mg/mL) were placed inside an induction coil and exposed for 20 min and temperature variations were then recorded with a multichannel optical fiber thermometer (Potemp4, Optocon Systems, DE). The optical probe was placed slightly beneath the surface of the medium; a second one was placed near the induction coil and used as reference for ambient temperature. The thermal efficiency was expressed as specific absorption rate. Because it was not possible to ensure the completely adiabatic condition of the experimental setup, this value was determined as the initial slope of the temperature increase, estimated by considering the linear term of a polynomial fitting of the heating curve of the samples (Lartigue et al., 2011).

### 2.2. Cell culture

3T3-L1 pre-adipocytes (ECACC, Sigma-Aldrich, St. Louis, MO, USA) were subcultured in Dulbecco's modified Eagle's medium nutrient mixture F12 containing 10% fetal bovine serum, 100 units mL<sup>-1</sup> penicillin and 100 µg mL<sup>-1</sup> streptomycin in a humidified incubator at 37 °C with 5% CO<sub>2</sub>. To stimulate differentiation into mature 3T3 adipocytes, the pre-adipocytes were grown to confluency in 35 × 10 mm Petri dish and then treated with the 3T3-L1 Differentiation Kit (Sigma-Aldrich, St. Louis, MO, USA) according to the manufacturer's protocol. Eight-days post-induction cells were subjected to the different treatments described below.

### 2.3. Cell viability assay

3T3 adipocytes were seeded (5 × 10<sup>3</sup> cells per well) in a 96-well plate and grown for 24 h in a humidified incubator at 37 °C with 5% CO<sub>2</sub>, then the medium was replaced with fresh medium containing different PIOs concentrations (10, 20, 50, 100 µg mL<sup>-1</sup>). The MTT (3-(4,5-dimethylthiazol-2-yl)-2,5-diphenyltetrazolium bromide) assay (Sigma) was used to evaluate cell viability after 6, 12, 24, 48 h of

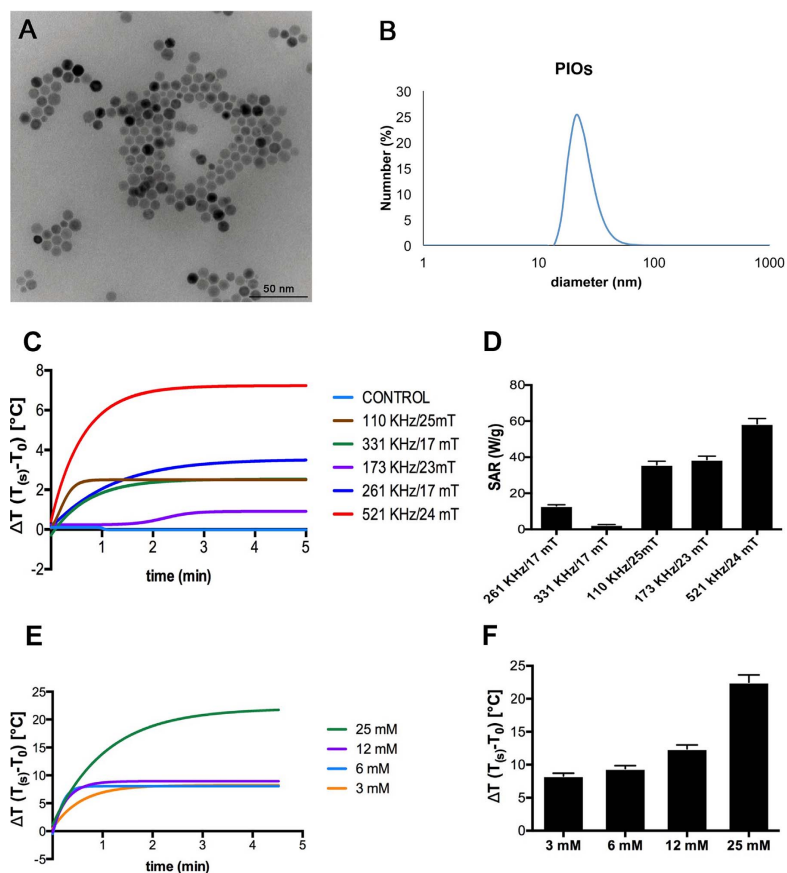


Fig. 1. A) Transmission electron microscopy of PIOS. B) Size distribution of PIOS by DLS. C, D) Temperature increase of PIOS suspension after 5 min for different AMF. E, F) Heat generation (temperature increase) by PIOS in suspension as a function of iron concentration.

exposure to PIOS at 37 °C. Absorbance was read by a microplate reader (CHROMATE 4300 Awareness Technology, USA). The test was conducted in triplicate. Statistical comparisons between treated and control samples were performed by using the non-parametric Mann Whitney *U* test.

Only PIOS concentrations proving to be safe for 3T3 adipocytes were used for the following experimentations.

#### 2.4. Flow cytometry analysis of PIOS internalization

3T3 adipocytes were incubated with different concentrations (10, 20 and 50  $\mu\text{g mL}^{-1}$ ) of fluorescently labelled PIOS for 15 min, 4 h, 24 h and 48 h at 37 °C. After washing with PBS, the cells were analyzed by flow cytometry to quantify the percentage of cells containing nanoparticles. Sample acquisition (10,000 events) was performed by Gallios Flow cytometer (Beckman Coulter Inc.) and analyzed by FlowJo

Software. Statistical analysis was performed by using the one-way Anova test.

#### 2.5. Confocal fluorescence microscopy analysis of PIOS internalization

3T3 adipocytes grown on coverslips were incubated with different concentrations (10, 20 and 50  $\mu\text{g mL}^{-1}$ ) of fluorescently labelled PIOS for 15 min, 4 h, 24 h and 48 h at 37 °C. The cells were then fixed with 4% buffered formalin for 30 min at room temperature, washed with PBS, permeabilized with 0.5% Triton X-100 in PBS and then incubated for 1 h at room temperature with the AlexaFluor® 647-labelled antibody NBP1-49533AF647 (final concentration 14  $\mu\text{g/mL}$  in BSA), recognizing the glucose transporter Glut4 typically overexpressed in adipocytes (Novus Biologicals Europe, Abingdon Oxon, UK). After washing in PBS, cell nuclei were stained with Hoechst 33342 and coverslips mounted with Entellan® (Merck KGaA, Darmstadt, Germany). Observations were

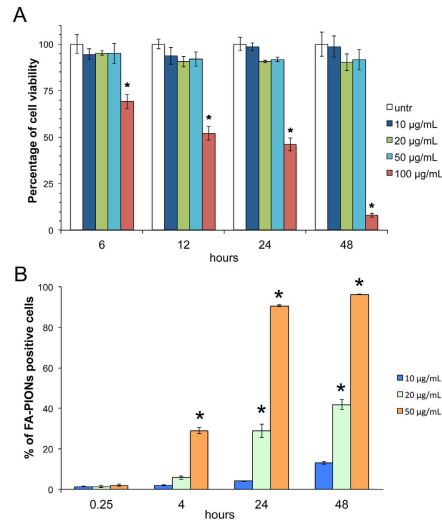


**Fig. 2.** A) Viability (MTT assay) of 3T3-L1 adipocytes after incubation with different PIO concentrations for 6, 12, 24 and 48 h. Asterisks indicate significantly different values ( $P < 0.05$ ) between treated and control samples. 100  $\mu\text{g mL}^{-1}$  PIOs induced a significant increase in cell death; consequently, this concentration was excluded from the subsequent experimentation. B) Flow cytometry analysis of fluorescently labelled PIOs internalization by 3T3 adipocytes, expressed as the percentage of positive cells compared to untreated cells. Histograms show a dose- and time-dependent uptake. Asterisks indicate significantly different values ( $P < 0.05$ ) between treated and control samples.

made with a Leica TCS SP5 inverted DM IRE2 confocal microscope equipped with an argon/krypton laser; three laser wavelengths were activated: UV (405 nm), blue (488 nm) and red (633 nm). A 40 x oil

immersion objective (numerical aperture 1) was used. The Leica LAS AF software was used for image collection and analysis.

## 2.6. Transmission electron microscopy analysis of PIOs internalization and lipolysis

The 3T3 adipocytes were grown as monolayers on glass coverslips, treated with 50  $\mu\text{g mL}^{-1}$  of PIOs for 24 h and 48 h at 37 °C, and then fixed with 2.5% (v/v) glutaraldehyde and 2% (v/v) paraformaldehyde in 0.1 M phosphate buffer, pH 7.4, at 4 °C for 1 h, post-fixed with 1% osmium tetroxide and 1.5% potassium ferrocyanide for 1 h, dehydrated with acetone and embedded in Epon resin. The 3T3 adipocyte samples submitted to SMHT were processed for transmission electron microscopy immediately after the SMHT and 24 h post-treatment as described above. Ultrathin sections were stained with lead citrate and observed in a Philips Morgagni transmission electron microscope (FEI Company Italia Srl, Milan, Italy) operating at 80 kV and equipped with a Megaview II camera for digital image acquisition.

## 2.7. SMHT effects

Based on the results of cell viability and internalization tests, 3T3 adipocytes were incubated for 24 h at 37 °C with 50  $\mu\text{g mL}^{-1}$  of PIOs, placed in an induction coil and exposed for 20 min to an AMF (521 KHz, 25 mT). Immediately after the SMHT, the cells were processed for triglyceride quantification; in addition, ultrastructural morphology and qRT-PCR were performed immediately after and 24 h post-hyperthermia. Statistical comparisons between treated and control samples were performed by using the Mann Whitney *U* test.

The amount of intracellular lipid was evaluated in triplicate by staining cytoplasmic triglycerides with Oil Red O (Bio-Optica, Milan, Italy). Briefly, the cells were fixed with 4% buffered formalin for 30 min, rinsed with PBS and stained for 20 min with 0.5% Oil Red O. Cell nuclei were counterstained with Mayer's hematoxylin solution (Sigma). Stained droplets were dissolved in isopropanol and then quantified by measuring absorbance at 490 nm with a VICTOR x series multilabel plate readers (PerkinElmer, Inc., Shelton, CT, USA). The results were expressed as the relative triglyceride content compared with the control (Lartigue et al., 2011). Statistical evaluations were

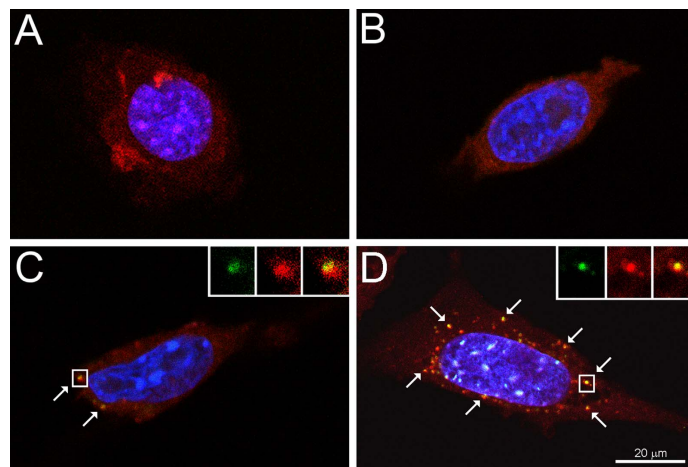


**Fig. 3.** Intracellular localization of PIOS. Confocal microscopy merged images of 3T3-L1 adipocytes after 24 h incubation with A) 0  $\mu\text{g mL}^{-1}$  (control), B) 10  $\mu\text{g mL}^{-1}$ , C) 20  $\mu\text{g mL}^{-1}$ , and D) 50  $\mu\text{g mL}^{-1}$  FA-PIOS (green). Cell membrane receptors were detected with the anti-Glut4 antibody (red) and nuclei were stained with Hoechst (blue). Arrows indicate internalized FA-PIOS. The insets show the overlapping of PIOS green signal with the Glut4 red signal thus appearing as yellow dots. Note the evident staining of Glut4 (overexpressed in 3T3 adipocytes) in all samples, demonstrating that treatment does not induce dedifferentiation. (For interpretation of the references to color in this figure legend, the reader is referred to the web version of this article.)

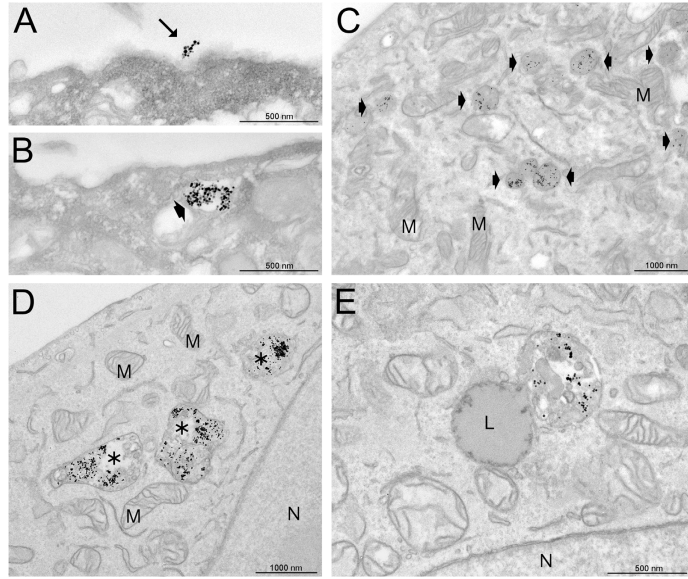


**Fig. 4.** Transmission electron microscopy images of PIOS uptake and intracellular distribution in 3T3-L1 adipocytes after 24 h incubation with PIOS ( $50 \mu\text{g mL}^{-1}$ ). A) PIOS were internalized by 3T3 adipocytes via endocytosis (arrow) and B) compartmentalized into endosomes (arrowhead). C) PIOS accumulated inside many endosomes (arrowheads) ubiquitously distributed in the cytoplasm, D) as well as in residual bodies (asterisks) also containing heterogeneous cell remnants. Mitochondria (M) and endoplasmic reticulum cisternae were abundant and well structured, demonstrating the absence of cell damage. E) Residual bodies containing PIOS also occurred very close to lipid droplets (L). N: cell nucleus.

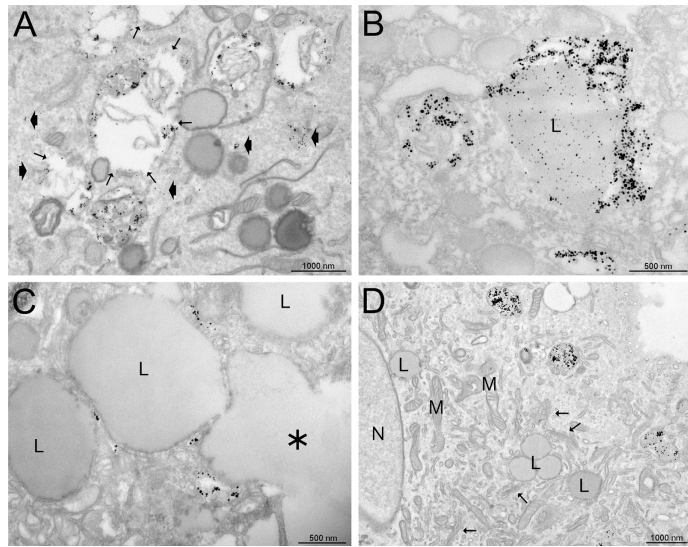


**Fig. 5.** Transmission electron microscopy images of 3T3 adipocytes after PIOS-mediated SMHT. A) After SMHT, some residual bodies containing PIOS appeared as damaged, with interruptions along their membranes (thin arrows), thus allowing the release of PIOS into the cytoplasm (arrowheads). B) Once free in the cytoplasm, some PIOS were found around and inside lipid droplets (L). C) Lipid droplets (L) approached the cell surface and were extruded (asterisk). D) 24 h after the hyperthermic treatment, a few lipid droplets of small size (L) were found in the cytoplasm, while mitochondria (M), endoplasmic reticulum and Golgi complexes (arrowheads) were well developed. N: cell nucleus.

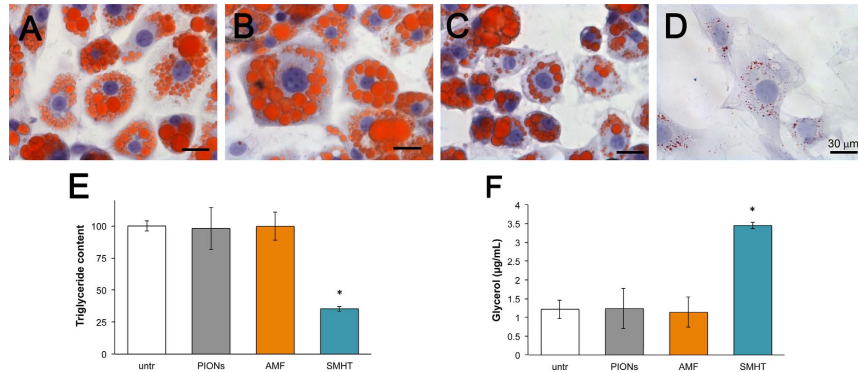


Fig. 6. A–D. Brightfield microscopy images (Oil Red O and hematoxylin staining) of control 3T3 adipocytes (A), 3T3 adipocytes incubated with PIONs (B), 3T3 adipocytes exposed to AFM (C) and 3T3 adipocytes immediately after SMHT (D). It is evident that the hyperthermic treatment induces a remarkable reduction of lipid droplets. E) Spectrophotometric evaluation of 3T3 adipocyte triglyceride content. Asterisk indicates significant difference from control ( $P < 0.05$ ). F) Colorimetric evaluation of the amount of glycerol in the culture medium. Asterisk indicates significant difference from control ( $P < 0.05$ ). (For interpretation of the references to color in this figure legend, the reader is referred to the web version of this article.)

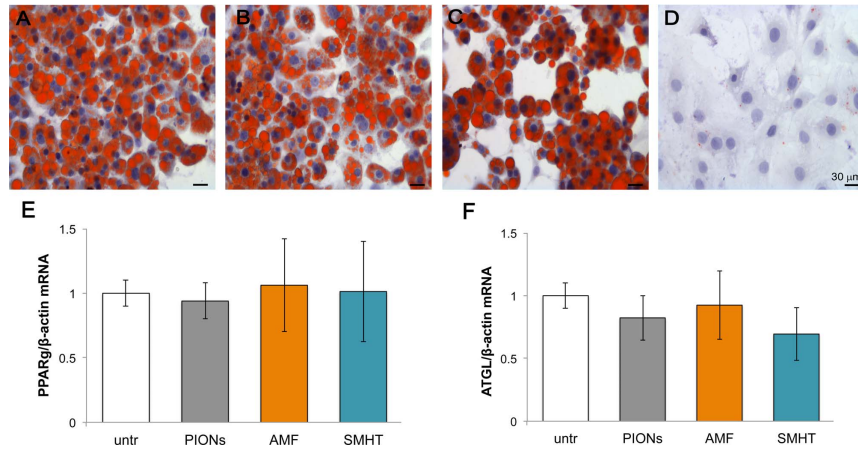


Fig. 7. A–D. Brightfield microscopy images (Oil Red O and hematoxylin staining) of control 3T3 adipocytes (A), 3T3 adipocytes incubated with PIONs (B), 3T3 adipocytes exposed to AFM (C) and 3T3 adipocytes 24 h after SMHT. Lipid depletion is maintained and the cells appear morphologically unaltered. E, F) Relative mRNA expression of PPAR $\gamma$  (E) and ATGL (F) genes in control 3T3 adipocytes, 3T3 adipocytes incubated with PIONs, 3T3 adipocytes exposed to AFM and 3T3 adipocytes 24 h after SMHT. No statistically significant difference was found. (For interpretation of the references to color in this figure legend, the reader is referred to the web version of this article.)

performed by using the Mann Whitney  $U$  test. Glycerol release from 3T3 adipocytes exposed to hyperthermia. The lipolytic effect of SMHT was determined in triplicate by measuring the amount of glycerol released into the medium (Ramirez-Zacarias et al., 1992) immediately after hyperthermia. Glycerol concentration was measured using a Glycerol Assay Kit (Sigma-Aldrich, St. Louis, MO, USA). Statistical comparisons were performed by using the Mann Whitney  $U$  test.

Total RNA was isolated from control and treated 3T3 adipocytes (in triplicate) using RNeasy Plus Mini Kit (QIAGEN; Milan, Italy). RNA (1.5  $\mu$ g) was reverse transcribed using High Capacity cDNA Reverse Transcription Kit (Applied Biosystems; Monza, Italy) and amplified using a StepOnePlus Real-Time PCR System (Applied Biosystems; Monza, Italy). The target

cDNAs were amplified using SYBR<sup>®</sup> Green PCR Master Mix (Invitrogen; Monza, Italy) together with gene-specific primers for peroxisome proliferator-activated receptor  $\gamma$ , PPAR $\gamma$  (fwd: AGAGATGTGCAAACAGGGCT, rev: GCAAAGGGTTGGTTGGTTC); adipin (fwd: GTGCAGAGTGT AGTGCCCTCA, rev: CCAACGAGGCATTCTGGGAT); adipose triglyceride lipase, ATGL (fwd: AGAGATGTGCAAACAGGGCT, rev: GCAAAGGGTTGG GTTGGTTC); p53 (fwd: AAACGCTTCGAGATGTCCG, rev: CTTCAGGT AGCTGGAGTGAGC);  $\beta$  -actin (fwd: CATCGTGGGCCGCTCTA, rev: CACCCACATAGGAGTCCITCTG). PCR conditions were 95 °C for 20 s, 95 °C for 3 s, and 60 °C for 30 s for 40 cycles. PCR products were measured using a StepOnePlus Real-time PCR System (Applied Biosystems; Monza, Italy) and relative ratios were calculated using the  $2^{-\Delta\Delta C_t}$  method

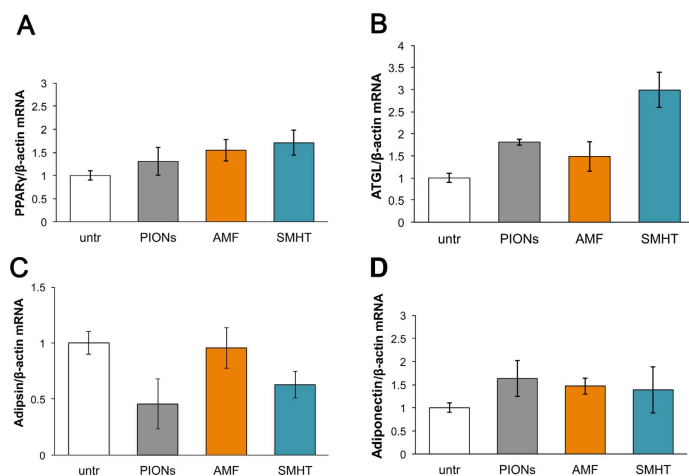


Fig. 8. Relative mRNA expression of PPAR $\gamma$ (A), ATGL (B), adipisin (C), and adiponectin (D) genes in control 3T3 adipocytes, 3T3 adipocytes incubated with PIONs, 3T3 adipocytes exposed to AMF and 3T3 adipocytes immediately after SMHT. No statistically significant difference was found.

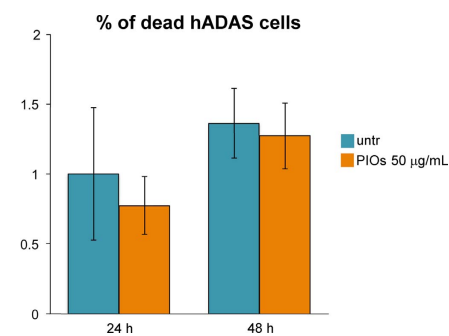


Fig. 9. Percentage of dead hADAS cells (trypan blue exclusion test) after incubation with 50  $\mu$ g/mL PIONs for 24 h and 48 h. No significant difference was found between PION-treated and untreated (untr) samples. (For interpretation of the references to color in this figure legend, the reader is referred to the web version of this article.)

(Schmittgen and Livak, 2008). Results were expressed as fold changes to control. Statistical analysis was conducted by using the Mann Whitney *U* test.

### 2.8. SMHT effects in hADAS cells

In order to evaluate preliminarily the suitability of PIONs for human adipocytes, hADAS cells were treated with the PIONs concentration demonstrated to have the best effect on 3T3 adipocytes (50  $\mu$ g mL $^{-1}$ ).

hADAS cells were grown, in Dulbecco's modified Eagle's medium nutrient mixture F12 containing 10% fetal bovine serum, 1% of a mix of penicillin/streptomycin and 1% fungizone, in a humidified incubator at 37 °C with 5% CO $_2$ . When at confluence, cells were treated with trypsin-EDTA 1% (GIBCO Life Technologies, USA), harvested and centrifuged at 1200 rpm for 5 min. The supernatant was discarded and cells pellet was resuspended in complete medium. The cells were then seeded

either on 24-multi-well plastic microplates (4  $\times$  10 $^3$  cells) for cell viability evaluation or glass coverslips in 12-multi-well (8  $\times$  10 $^3$  cells) plastic microplates for light and transmission electron microscopy. Twenty-four hours after seeding, to induce the differentiation into adipocytes, cells were switched to adipogenic medium (DMEM F12, 10% fetal bovine serum, 1% of penicillin/streptomycin, IBMX 100X, dexametason 100X, rosiglitazone 100X, 10  $\mu$ g/mL of insulin) and maintained in this medium for 12 days. Then, fresh medium containing 50  $\mu$ g mL $^{-1}$  of sterilized PIONs was administered for either 24 h or 48 h.

To estimate the effect of PIONs on hADAS cell viability, the trypan blue exclusion test was performed since this test is more suitable than MTT assay for these cells. Cells were detached by mild trypsinization and stained in suspension for 2 min with 0,01% trypan blue in the culture medium, and the percentage of non-viable trypan blue-permeable cells was estimated by counting on a Burker Turk hemocytometer. Cell samples not exposed to PIONs were considered as controls. Results were expressed as the mean  $\pm$  standard error (SE) of three independent experiments. Statistical comparisons between treated and control samples were performed by using the non-parametric Mann Whitney *U* test.

Transmission electron microscopy was applied to analyse PIONs internalization and hADAS cell structural preservation after treatment; cells were processed and observed as described for 3T3 adipocytes.

The hADAS cells were then submitted to SMHT similarly to 3T3 adipocytes and the effects evaluated by morphological analysis at light microscopy immediately and 24 h after treatment. To observe lipid accumulation, hADAS cells were fixed and stained with Red Oil O as described for 3T3 adipocytes.

## 3. Results

### 3.1. Synthesis of SPIONs and determination of their hyperthermic efficiency

As several works have highlighted the importance to have iron oxide nanocrystals with edged shape to improve the heat power of nanomediators in hyperthermia, we synthesized polyhedral iron oxide nanocrystals (PIONs) and assessed their hyperthermic efficiency (Fig. 1). These nanoparticles were produced in octadecene at elevated temperature of crystallization and were first isolated in chloroform due to

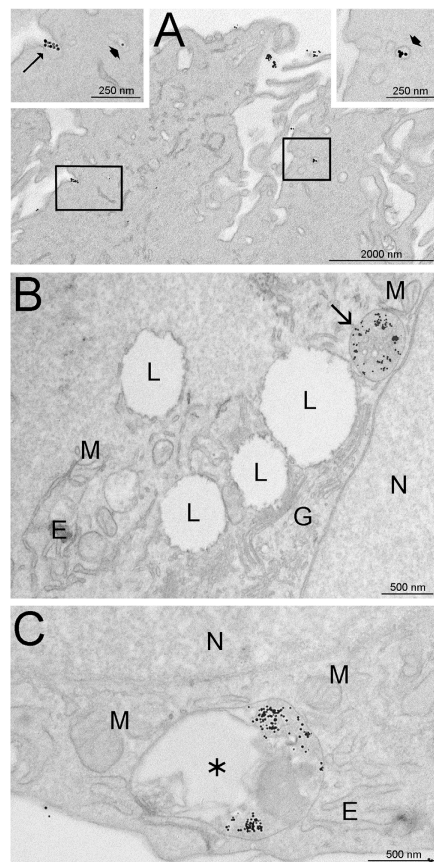


Fig. 10. Transmission electron microscopy images of PIOS uptake and intracellular distribution in ADAS cells after 24 h (A and B) and 48 h (C) incubation with  $50 \mu\text{g mL}^{-1}$  PIOS. A) PIOS were internalized via endocytosis as very small clusters (thin arrow in left inset), and compartmentalized into small vesicles (arrowheads in insets). B) PIOS accumulated inside secondary lysosomes (arrow); no PIOS was found free in the cytosol or inside cell nucleus (N), mitochondria (M), Golgi apparatus (G), endoplasmic reticulum (E) or lipid droplets (L). C) After 48 h incubation, PIOS were also found inside residual bodies (asterisk) containing heterogeneous cell remnants; cell nucleus (N), mitochondria (M) and endoplasmic reticulum (E) did not show structural damage.

oleic surfactant coating and then transferred to water phase by wrapping their surface individually with the PMA amphiphilic polymer. The nanocrystals were both highly colloidal stable in PBS for at least six months. The hydrodynamic sizes of PIOS were  $12.6 \pm 0.4 \text{ nm}$  (Fig. 1A and B), as measured by dynamic light scattering (DLS), with  $\zeta$ -potential of  $-59.3 \pm 2.3 \text{ mV}$ .

PIOS exhibited frequency-dependent heat capacity with an optimal response at 521 KHz and 25 mT (Fig. 1C). The magnetic hyperthermia efficiency test (Fig. 1D) confirmed that PIOS were able to act as hyperthermic mediators (Guardia et al., 2012). The amount of heat

produced by SMHT increased linearly with PIO concentration (Fig. 1E and F). Fig. 1E shows the temperature profile at  $[\text{Fe}] = 25 \text{ mM}$  (corresponding to  $\sim 6.5 \text{ mg mL}^{-1}$  concentration of nanoparticles), with MHT frequency at 521 KHz, 25 mT field amplitude. The application of MHT to the sample resulted in a temperature increase of  $20^\circ\text{C}$  after 120 s reaching a plateau after 6 min with a maximal  $\Delta T$  of  $22.5^\circ\text{C}$ . Because the measurements were performed in non-adiabatic conditions, the curve slopes were fitted only in the first 30 s. Under the frequency and amplitude conditions reported in Fig. 1E, a SAR of  $157.2 \text{ W/g}$  was calculated. This value is consistent with a specific loss power in a good range suitable for hyperthermia considering that to date the maximum SAR obtained with iron oxide nanoparticles was around  $1000 \text{ W/g}$  using MHT alone (Lartigue et al., 2012). SAR is dependent on MHT frequency and field amplitude: SAR values relative to the different conditions are summarized in Fig. 1C and D.

### 3.2. PIOS uptake and 3T3 adipocytes viability

As an in vitro model to test the impact of different concentrations of PIOS we employed 3T3-L1 pre-adipocytes differentiated into mature 3T3 adipocytes. MTT assay demonstrated that PIOS were safe up to the concentration of  $50 \mu\text{g mL}^{-1}$  at short and long (48 h) incubation times, whereas  $100 \mu\text{g mL}^{-1}$  PIOS induced a significant increase in cell death already after 6 h incubation (Fig. 2A). Flow cytometry analysis of fluorescently labelled PIOS uptake (Fig. 2B) demonstrated that 3T3 adipocytes treated with  $50 \mu\text{g mL}^{-1}$  PIOS efficiently internalized the nanoparticles, showing about 20% positive cells after 4 h incubation and reaching about 100% between 24 and 48 h. Confocal fluorescence microscopy (Fig. 3) confirmed flow cytometry data, showing that the maximal PIO internalization occurred at the concentration of  $50 \mu\text{g mL}^{-1}$  (Fig. 3D). Most of the internalized green fluorescent PIOS appeared as yellow dots due to the overlap with the red signal of the membrane receptor Glut4, thus suggesting an endocytosis-mediated uptake (Fig. 3C and D). Moreover,  $50 \mu\text{g mL}^{-1}$  of PIOS did not change the expression of Glut4 receptor, a key marker of 3T3-L1 adipocyte differentiation, indicating that PIOS uptake did not interfere with the differentiation process (Fig. 3, compare panel A with panel D). These observations were validated by ultrastructural analysis (Fig. 4) demonstrating that PIOS were internalized via endocytosis and entrapped into endosomes (Fig. 4A and B). Once in the cytoplasm, PIOS were always observed inside both endosomes (Fig. 4C) and residual bodies (Fig. 4D), often occurring very close to lipid droplets (Fig. 4E). PIOS were never found free in the cytoplasm or in contact with any organelle. Large amounts of PIOS were found into 3T3 adipocytes up to 48 h, suggesting a long-lasting cytoplasmic persistence. No ultrastructural cell damage was observed following PIO internalization until 48 h incubation, confirming the safety of these nanoparticles at the concentration of  $50 \mu\text{g mL}^{-1}$ .

### 3.3. Lipolytic effect of SMHT

SMHT proved to be a safe procedure for 3T3 adipocytes. In fact, the MTT assay demonstrated that the percentage of cell viability was unaffected by SMHT in comparison with control conditions (untreated cells subjected to AMF and cells treated only with PIOS but not exposed to AMF) both immediately after and 24 h after the treatment (Fig. S1, A and B). Further confirmation on the safety of SMHT was provided by qRT-PCR analysis of tumor suppressor p53 mRNA expression, a marker of growth rate, in 3T3 adipocytes immediately and 24 h post-treatment (Fig. S1, C and D, respectively). Our data demonstrated that neither PIOS, AMF or SMHT affected significantly p53 expression in comparison to untreated 3T3 adipocytes. Accordingly, ultrastructural analysis demonstrated that no ultrastructural cell damage occurred immediately after and 24 h after SMHT (Fig. 5). Immediately after SMHT, interruptions of residual bodies membranes enclosing PIOS were observed (Fig. 5A), and PIOS freely distributed in the cytoplasm were found to

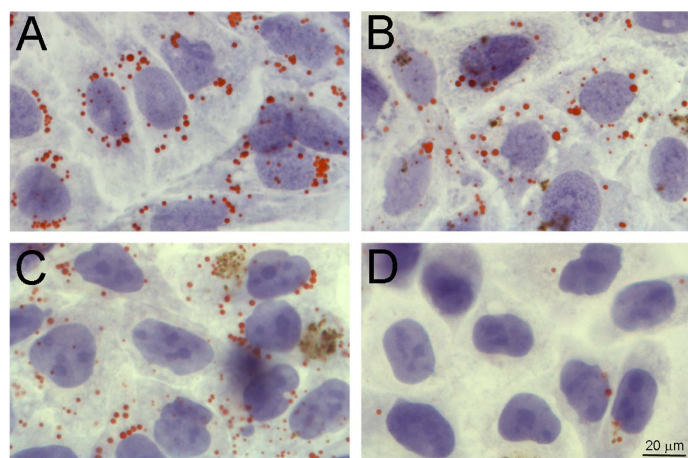


**Fig. 11.** Brightfield microscopy images (Oil Red O and hematoxylin staining) of control hADAS cells (A), hADAS cells incubated with PIOS for 24 h (B), hADAS cells immediately after SMHT (C) and hADAS cells 24 h after SMHT (D). Note the loss of lipid droplets in D. (For interpretation of the references to color in this figure legend, the reader is referred to the web version of this article.)

accumulate around and even into lipid droplets (Fig. 5B). Some lipid droplets were extruded from the cell (Fig. 5C). Twenty-four hours after SMHT, a few lipid droplets of small size were found in the cytoplasm, while mitochondria, endoplasmic reticulum and Golgi complexes were well developed, confirming no cell damage at long term (Fig. 5D). The lipolytic effect of SMHT was demonstrated by light microscopy observation of Oil Red O stained 3T3 adipocytes, which showed a remarkable decrease in lipid droplet content after hyperthermia (Fig. 6A–D). This lipid depletion was confirmed by the significantly decreased absorbance values of Oil Red O-extracted stain corresponding to triglycerides amount (Fig. 6E), as well as by the concomitant increase in glycerol content in the culture medium after SMHT (Fig. 6F). Both light (Fig. 7A–D) and electron microscopy (Fig. 5D) demonstrated that 3T3 adipocytes maintained a low lipid content up to 24 h after SMHT.

#### 3.4. SMHT affects triglycerides metabolism in 3T3 adipocytes

To start getting insight into the molecular basis of the observed SMHT-induced lipolysis, we performed qRT-PCR analysis to assess the expression levels of key genes involved in lipid metabolism. We focused our attention on PPAR $\gamma$  and ATGL, as both genes play key roles in the adipolysis process (Kershaw et al., 2007; Zechner et al., 2012). PPAR $\gamma$  mediates several processes among which the regulation of ATGL expression. ATGL is the limiting-step enzyme in the triglyceride metabolism, producing diacylglycerol, subsequently metabolized by hormone-sensitive lipase into glycerol and fatty acids. Therefore, ATGL plays a prominent role in triglyceride mobilization (Duncan et al., 2007; Arner and Langin, 2014). As shown in Fig. 8, A and B, no significant differences were observed immediately after SMHT for both PPAR $\gamma$  and ATGL transcripts, compared with untreated, PIOS- and AFM-treated cells, although p value of ATGL variation between untreated and SMHT samples is close to the statistical significance ( $p = 0.067$ ). Similar results were obtained 24 h after SMHT (Fig. 7E and F). Lipid metabolism is a balance between adipolysis and adipogenesis (Nielsen et al., 2014). Adipsin is acknowledged as a critical adipokine regulating adipogenesis through the regulation of the acylation stimulating protein (ASP), a key mediator of adipose tissue triglyceride storage (Cianflone et al., 2003). On this basis, we sought to investigate whether variations in adipsin expression had occurred as a cell attempt to compensate for lipid

depletion (lipolysis), by promoting de novo triacylglycerol storage. As shown in Fig. 8C, neither PIOS, AMF or SMHT significantly affected adipsin expression in comparison to untreated 3T3 adipocytes. We also examined Adiponectin expression, a cytokine highly expressed in differentiated adipocytes with a broad range of system-wide actions including glucose regulation and fatty acid oxidation (Rutkowski et al., 2015). Under our experimental conditions no alteration of the expression for adiponectin was detected (Fig. 8D).

#### 3.5. SMHT effects in hADAS cells

After 12 day in the adipogenic medium, the treatment with  $50 \mu\text{g mL}^{-1}$  PIOS did not increase hADAS cell death until 48 h incubation, as demonstrated by the trypan blue exclusion test (Fig. 9).

Observation at transmission electron microscope showed that uptake occurred by endocytosis of very small clusters of PIOS, which were then found inside small vesicles close to the plasma membrane (Fig. 10A). Higher amounts of PIOS were found inside secondary lysosomes mostly located in the inner cytoplasmic region (Fig. 10B). After long (48 h) incubation time, PIOS were also found inside residual bodies containing heterogeneous cellular debris (Fig. 10C). Similarly to 3T3 adipocytes, in hADAS cells PIOS were never found free in the cytoplasm or in contact with any organelle, and no morphological alteration was observed following PIOS internalization until 48 h incubation, demonstrating the safety of these nanoparticles at the concentration of  $50 \mu\text{g mL}^{-1}$  also for hADAS cells.

The SMHT induced an evident delipidation after 24 h from treatment (Fig. 11).

## 4. Discussion

The main aim of this study was to explore the capability of SPIONs to reduce the lipid content in mature 3T3 adipocytes, as a novel strategy to counteract obesity alternatively to pharmacological and surgical approaches and hyperthermic treatments (Franco et al., 2010; Ito and Saito, 2011; Otto, 2016). These nanoparticles, approved by FDA for human use due to their good biodegradability (Kim et al., 2013), produce heat when subjected to an AMF (Jordan et al., 1993; Lee et al., 2011; Guardia et al., 2012; Lartigue et al., 2012; Mannucci et al., 2014;

Orlando et al., 2016). In particular, the polyhedral nanoparticles synthesized in our study, termed PIOs, proved to provide a good frequency-dependent heat capacity suitable for their utilization as hyperthermic mediators for our purposes. So far, SPIONs have been explored in the treatment of different tumors (Johannsen et al., 2007; Maier-Hauff et al., 2007; Matsumine et al., 2007), i. e., as therapeutic mediators able to induce targeted cell death. In our study we applied SMHT to modulate lipid metabolism. With this purpose, in order to ensure controlled experimental conditions, we used 3T3-L1 adipocyte cell line as a standardized in vitro model widely used for studies relevant to adipose tissue.

The first step of our study was the accurate selection of a PIOs concentration ensuring both efficient internalization and absence of cell death and damage. In particular, the high resolution of transmission electron microscopy excluded any short and long-term (48 h post-treatment) cell organelle alteration, which could prelude to necrotic or apoptotic processes responsible for inflammatory events in vivo. Microscopic analyses also demonstrated that, once internalized, PIOs remained confined in the cytoplasm, never entering the nucleus even at the longest incubation times. This is indubitably an advantage since entering the nucleus may represent a risk due to the possible interactions between PIOs and nucleic acids and/or nuclear factors, which could unpredictably alter cell function. A further advantage is that PIOs occurring in the cytoplasm are always enclosed in vesicular structures, i.e., endosomes formed during the endocytic process and residual bodies derived from the lytic pathways. Thus, the iron contained in PIOs, representing a potential source of oxidative stress (Mahmoudi et al., 2012), never makes direct contact with cytosolic or organelle components, even after long incubation times. Finally, molecular analyses excluded alterations (up to 48 h of PIO exposure) in the expression of the tumor suppressor p53 gene, involved in cell cycle progression, DNA repair and apoptosis (Biegging et al., 2014).

It has been reported that SPIONs are able *per se* of modulating gene clusters considered as a potential risk for obesity or type 2 diabetes (Sharifi et al., 2013). However, in our study, the expression of some key genes involved in lipid metabolism (among which PPAR $\gamma$ , one of the high risk genes linked with type 2 diabetes) proved to be unaffected by PIOs treatment. This discrepancy could be related to different experimental conditions i.e., our PIOs have been differently synthesized, have different physico-chemical characteristics, and we used them at different concentrations and exposure time in comparison to the work of Sharifi et al. (2013). Moreover, while the altered expression of a few genes, as reported by Sharifi et al., may contribute to cell metabolic dysfunctions, under our experimental conditions, 3T3 adipocytes features were preserved during the treatments.

Therefore, the absence of transcriptional modulation of the selected genes in 3T3 adipocytes further demonstrates the safety of PIOs treatment chosen for the application of SMHT.

SMHT was then applied under the mildest conditions for 3T3 adipocytes. Possible structural and/or functional alterations of 3T3 adipocytes related only to AFM exposure were also excluded. Moreover, the temperature decrease in culture medium occurring during the whole SMHT process (taking 20 min out of the incubator) was about 2 °C, thus excluding a concomitant hypothermic shock. Consequently, we can conclude that the remarkable lipolytic effect observed under our experimental conditions is exclusively due to the SMHT. Although the hyperthermic property of PIOs is clearly demonstrated by tests in aqueous solution, we have no data about the  $\Delta T$  occurring inside 3T3 adipocytes during the SMHT. Our unpublished data (Mannucci et al., submitted) demonstrated that a SMHT-mediated  $\Delta T$  of 0.5 °C causes massive cell death in tumors; it is therefore likely that the intracellular temperature rise in 3T3 adipocytes was even lower. We can therefore hypothesize that the massive lipolysis is due to the sudden temperature rise occurring in the intracellular compartment. We demonstrated that in our samples no cell death or damage was found up to 24 h after SMHT. The biological reasons of such a rapid and massive lipolytic

effect remain unclear. Transmission electron microscopy revealed that, following SMHT, the membrane of residual bodies containing PIOs may undergo rupture, thus allowing the nanoparticles to freely spread into the cytosol. This phenomenon does not induce cell damage probably because residual bodies do not contain lytic enzymes and/or membrane integrity is rapidly restored, similarly to the process of endosomal escape (Varkouhi et al., 2011). Free PIOs seem to preferentially migrate close to and even inside lipid droplets: this preference could be associated to the amphiphilic character of nanoparticle coating. Similarly, lipid droplets have been described to accumulate liposome components internalized by HeLa cells (Costanzo et al., 2016); in both 3T3 adipocytes and HeLa cells, lipid droplets are finally extruded in the culture medium. This particular delipidation process has been recently investigated in detail in human 3T3 adipocytes: it is an active process triggered by cell stress, and lipid droplets are extruded through micropores transitory forming in the plasmalemma, thus allowing cell structural preservation and viability (Conti et al., 2014). Accordingly, 3T3 adipocytes subjected to SMHT not only remain fully vital up to 24 h post-treatment, but also show well-preserved ultrastructural features and unaltered expression of genes involved in lipid metabolism. Our results therefore demonstrate that, if appropriately applied to 3T3 adipocytes, SMHT can act as a mild controlled stress able to efficiently activate a physiological lipolytic process. Importantly, no apparent dedifferentiation effect or cellular reprogramming is associated to SMHT, as suggested by the persistence of Glut4 and adiponectin expression, key features of mature 3T3 adipocytes, suggesting that this approach can reduce lipid content concomitantly maintaining adipose cell commitment. Interestingly, the observed lipolytic process is not accompanied by increased expression of ATGL, whose mRNA expression is normally elevated by peroxisome proliferator-activated receptor (PPAR $\gamma$ ) agonists (Zechner et al., 2012). This suggests that a pathway involving other than PPAR $\gamma$  and ATGL effectors may be involved in the lipolysis effect by SMHT and yet to be defined. Alternatively, one can hypothesize the occurrence of a “thermal stimulus” responsible for lipid extrusion to be further investigated. Interestingly, mRNA expression of adipisin, the major adipokine released by adipose cells promoting triglyceride storage in adipocytes (Sniderman and Cianflone, 1994; Lo et al., 2014) was not upregulated as a means to counteract the significant lipid loss, thus establishing a possible correlation with the prolonged (24 h) delipidated state of the SMHT-treated 3T3 adipocytes. Accordingly, gene expression of adiponectin, a protein hormone involved in fatty acid oxidation and reduction of triglyceride content (Karbowska and Kochan, 2006), was not altered by SMHT as well. These observations further argues in favor of a lipolytic mechanism independent of the canonical events regulating the process.

PIOs proved to be safe and effective for SMHT also in hADAS cells. These cells internalized lower amounts of PIOs in comparison to 3T3 adipocytes, probably because metabolic activity of cultured primary cells is reduced in comparison to established cell lines. Nevertheless, despite the lower amounts of accumulated PIOs SMHT induced a marked delipidation in hADAS cells. In 3T3 adipocytes, this lipid loss occurs immediately after SMHT while in hADAS it becomes evident after 24 h from treatment: this discrepancy may be related to various factors, such as the reduced uptake of PIOs or the different content of lipid droplets in hADAS cells or to species-specific differences. Anyway, the positive results obtained in hADAS cells, although still preliminary, provide a promising experimental background for future applications of SMHT to human adipose tissue.

The success of this pioneering approach in vitro opens promising perspectives for the application of SMHT in vivo as an innovative safe and physiologically mild strategy against obesity, potentially useful in combination with balanced diet and healthy lifestyle. SMHT seems to have advantages over conventional hyperthermic approaches (Franco et al., 2010; Ito and Saito, 2011; Otto, 2016) because heat-generating nanoparticles may be easily injected, thus avoiding macroscopic implants. In addition, SPIONs are versatile nanoparticles that can be

administered by different routes among which ingestion (Chamorro et al., 2015) and transdermal application (Santini et al., 2015). It is worth noting that, similarly to many other nanoparticles, SPION surface may be functionalized and their distribution controlled by targeting strategies, thus focusing the hyperthermic treatment in specific tissues.

The present study therefore represent an original starting point to advance in the research aimed at counteracting obesity and the multiple pathologies associated.

#### Author contributions

The manuscript was written through the contributions of all authors. All authors have given approval to the final version of the manuscript.

#### Acknowledgment

This research was supported by FRRB (Fondazione Regionale per la Ricerca Biomedica) (NANODRUG platform project) and Fondazione Umamo Progresso.

#### Appendix A. Supplementary data

Supplementary data associated with this article can be found, in the online version, at <http://dx.doi.org/10.1016/j.biocel.2017.10.013>.

#### References

- Ahima, R.S., Lazar, M.A., 2013. The health risk of obesity—better metrics imperative. *Perspect. Physiol. Sci.* 341 (6148), 856–858. <http://dx.doi.org/10.1126/science.1241244>.
- Arner, P., Langin, D., 2014. Lipolysis in lipid turnover, cancer cachexia, and obesity-induced insulin resistance. *Trends Endocrinol. Metab.* 25, 255–262.
- Arner, E., Westermark, P.O., Spalding, K.L., Britton, T., Rydén, M., Frisén, J., Bernard, S., Arner, P., 2010. Adipocyte turnover: relevance to human adipose tissue morphology. *Diabetes* 59, 105–109.
- Bernabucci, U., Basiricò, L., Morera, P., Lacetera, N., Ronchi, B., Nardone, A., 2009. Heat shock modulates adipokines expression in 3T3-L1 adipocytes. *J. Mol. Endocrinol.* 42, 139–147.
- Bhaskaran, K., Douglas, I., Forbes, H., dos-Santos-Silva, I., Leon, D.A., Smeeth, L., 2014. Body-mass index and risk of 22 specific cancers: a population-based cohort study of 5.24 million UK adults. *Lancet* 384, 755–765.
- Bieganski, K.T., Mello, S.S., Attardi, L.D., 2014. Unravelling mechanisms of p53-mediated tumor suppression. *Nat. Rev. Cancer* 14, 359–370.
- Bjorge, T., Engeland, A., Tverdal, A., Smith, G.D., 2008. Body mass index in adolescence in relation to cause-specific mortality: a follow up of 230,000 Norwegian adolescents. *Am. J. Epidemiol.* 168, 30–37.
- Brasaele, D.L., 2007. Thematic review series: adipocyte biology. The perilipin family of structural lipid droplet proteins: stabilization of lipid droplets and control of lipolysis. *J. Lipid Res.* 48, 2547–2559.
- Calderan, L., Marzola, P., Nicolato, E., Fabene, P.F., Milanese, C., Bernardi, P., Giordano, A., Cinti, S., Sbarbati, A., 2006. In vivo phenotyping of the ob/ob mouse by magnetic resonance imaging and <sup>1</sup>H-magnetic resonance spectroscopy. *Obesity* 3, 405–414.
- Chamorro, S., Gutierrez, L., Vaquero, M.P., Verdoy, D., Salas, G., Luengo, Y., Brenes, A., Teran, F.J., 2015. Safety assessment of chronic oral exposure to iron oxide nanoparticles. *Nanotechnology* 26, 205101.
- Cianflone, K., Xia, Z., Chen, Y., 2003. Critical review of acylation-stimulating protein physiology in humans and rodents. *BBA* 1609, 127–143.
- Colombo, M., Carregal-Romero, S., Casula, M.F., Gutiérrez, L., Morales Böhm, M.P.I.B., Heverhagen, J.T., Prosperi, D., Parak, W.J., 2012. Biological applications of magnetic nanoparticles. *Chem. Soc. Rev.* 41, 4306–4334.
- Conti, G., Benati, D., Bernardi, P., Jurga, M., Rigotti, G., Sbarbati, A., 2014. The post-adipogenic phase of the adipose cell cycle. *Tissue Cell* 46 (6), 520–526.
- Costanzo, M., Carton, F., Marengo, A., Berlier, G., Stella, B., Arpico, S., Malatesta, M., 2016. Fluorescence and electron microscopy to visualize the intracellular fate of nanoparticles for drug delivery. *Eur. J. Histochem.* 60 (2), 2640.
- De Pergola, G., Silvestris, F., 2013. Obesity as a major risk factor for cancer. *J. Obesity* 11. <http://dx.doi.org/10.1155/2013/291546>. (Article ID 291546).
- Duncan, R., Ahmadian, M., Jaworski, K., Sarkadi-Nagy, E., Sul, H.S., 2007. Regulation of lipolysis in adipocytes. *Annu. Rev. Nutr.* 27, 79–101.
- Franco, W., Kothare, A., Ronan, S.J., Grekin, R.C., McCalmont, T.H., 2010. Hyperthermic injury to adipocyte cells by selective heating of subcutaneous fat with a novel radiofrequency device: feasibility studies. *Lasers Surg. Med.* 42 (5), 361–370.
- Granneman, J.G., Moore, H.P., 2008. Location, location: protein trafficking and lipolysis in adipocytes. *Trends Endocrinol. Metab.* 19, 3–9.
- Granneman, J.G., Moore, H.P., Krishnamoorthy, R., Rathod, M., 2009. Perilipin controls lipolysis by regulating the interactions of AB-hydrolase containing 5 (Abhd5) and adipose triglyceride lipase (Atgl). *J. Biol. Chem.* 284, 34538–34544.
- Guardia, P., Di Corato, R., Lartigue, L., Wilhelm, C., Espinosa, A., Hernandez, M.G., Gazeau, F., Manna, L., Pellegrino, T., 2012. Water-soluble iron oxide nanocubes with high values of specific absorption rate for cancer cell hyperthermia treatment. *ACS Nano* 6, 3080–3091.
- Hajer, G.R., van Haeflert, T.W., Visseren, F.L., 2008. Adipose tissue dysfunction in obesity, diabetes, and vascular diseases. *Eur. Heart J.* 29, 2959–2971.
- Hashimoto, T., Segawa, H., Okuno, M., Kano, H., Hamauchi, H.O., Harauchi, T., Hiraoka, Y., Hattai, S., Yamaguchi, T., Hirose, F., Osumi, T., 2012. Active involvement of micro-lipid droplets and lipid droplet-associated proteins in hormone-stimulated lipolysis in adipocytes. *J. Cell Sci.* 125, 6127–6136.
- Hassan, M., Latif, N., Yacoub, M., 2012. Adipose tissue: friend or foe? *Nat. Rev. Cardiol.* 9, 689–702.
- Hotamisligil, G.S., Arner, P., Caro, J.F., Atkinson, R.L., Spiegelman, B.M., 1995. Increased adipose tissue expression of tumor necrosis factor- $\alpha$  in human obesity and insulin resistance. *J. Clin. Invest.* 95, 2409–2415.
- Ito, K., Saito, K., 2011. Development of microwave antennas for thermal therapy. *Curr. Pharm. Des.* 17 (22), 2360–2366.
- Ja, J., Gavriloa, O., Pack, S., Joo, W., Mullen, S., Sumner, A., Cushman, S.W., Periwai, V., 2009. Hypertrophy and/or hyperplasia: dynamics of adipose tissue growth. *PLoS Comput. Biol.* 5 (March (3)), e1000324. <http://dx.doi.org/10.1371/journal.pcbi.1000324>.
- Johannsen, M., Gneveckow, U., Thiesen, B., Taymorian, K., Cho, C.H., Waldöfner, N., Scholz, R., Jordan, A., Loening, S.A., Wust, P., 2007. Thermotherapy of prostate cancer using magnetic nanoparticles: feasibility, imaging, and three-dimensional temperature distribution. *Eur. Urol.* 52, 1653–1662.
- Jordan, A., Wust, P., Fahling, H., John, W., Hinz, A., Felix, R., 1993. Inductive heating of ferrimagnetic particles and magnetic fluids: physical evaluation of their potential for hyperthermia. *Int. J. Hyperthermia* 9, 51–68.
- Karbowska, J., Kochan, Z., 2006. Role of adiponectin in the regulation of carbohydrate and lipid metabolism. *J. Physiol. Pharmacol.* 57, 103–113.
- Kershaw, E.E., Schupp, M., Guan, H.P., Gardner, N.P., Lazar, M.A., Flier, J.S., 2007. PPAR $\gamma$  regulates adipose triglyceride lipase in adipocytes in vitro and in vivo. *Am. J. Physiol. Endocrinol. Metab.* 6, 293.
- Kim, D., Park, J., Kweon, D., Han, D.G., 2013. Bioavailability of nanoemulsified conjugated linoleic acid for an antiobesity effect. *Int. J. Nanomed.* 8, 451–459.
- Klii-Drori, A.J., Azoulay, L., Pollak, M.N., 2017. Cancer, obesity, diabetes, and anti-diabetic drugs: is the fog clearing? *Nat. Rev. Clin. Oncol.* 14, 85–99. <http://dx.doi.org/10.1038/nrclinonc.2016.120>.
- Kopelman, P.G., 1997. The effects of weight loss treatments on upper and lower body fat. *Int. J. Obes. Relat. Metab. Disord.* 21 (8), 619–625.
- Lambert, E.V., Hudson, D.A., Bloch, C.E., Koeslag, J.H., 1991. Metabolic response to localized surgical fat removal in nonobese women. *Aesthetic Plast. Surg.* Spring 15 (2), 105–110.
- Lartigue, L., Innocenti, C., Calaivani, T., Awwad, A., Sanchez Duque Mdel, M., Guari, Y., Larionova, J., Guérin, C., Montero, J.L., Barragan-Montero, V., Arosio, P., Lascialfari, A., Gatteschi, D., Sangregorio, C., 2011. Water-dispersible sugar-coated iron oxide nanoparticles. An evaluation of their relaxometric and magnetic hyperthermia properties. *J. Am. Chem. Soc.* 133 (27), 10459–10472. <http://dx.doi.org/10.1021/ja111448t>.
- Lartigue, L.N., Hugouenon, P., Alloyear, D., Clarke, S.P., Lévy, M., Bacci, J.C., Bazzi, R., Broggham, D.F., Wilhelm, C., Gazeau, F., 2012. Cooperative organization in iron oxide multi-core nanoparticles potentiates their efficiency as heating mediators and MRI contrast agents. *ACS Nano* 6, 10935–10949.
- Lee, J.H., Jang, J.T., Choi, J.S., Moon, S.H., Noh, S.H., Kim, J.W., Kim, J.G., Kim, I.S., Park, K.I., Cheon, J., 2011. Exchange-coupled magnetic nanoparticles for efficient heat induction. *Nat. Nanotechnol.* 6, 418–422.
- Lerner, Z.F., Board, W.J., Browning, R.C., 2016. Pediatric obesity and walking duration increase medial tibiofemoral compartment contact forces. *J. Orthop. Res.* 34, 97–105.
- Lin, C.A.J., Sperling, R.A., Li, J.K., Yang, T.Y., Li, P.Y., Zamella, M., Chang, W.H., Parak, W.J., 2008. Design of an amphiphilic polymer for nanoparticle coating and functionalization. *Small* 4, 334–341.
- Lo, J.C., Ljubicic, S., Leibiger, B., Kern, M., Leibiger, B.I., Moede, T., Kelly, M.E., Bhowmick, D.C., Murano, L., Cohen, P., Banks, A.S., Khandekar, M.J., Dietrich, A., Flier, J.S., Cinti, S., Blüher, M., Danial, N.N., Berggren, P.O., Spiegelman, B.M., 2014. Adipin is an adipokine that improves (cell function in diabetes). *Cell* 158, 41–53.
- Mahmoudi, M., Hofmann, H., Rothen-Rutishauser, B., Petri-Fink, A., 2012. Assessing the in vitro and in vivo toxicity of superparamagnetic iron oxide nanoparticles. *Chem. Rev.* 112, 2323–2338.
- Maler-Hauff, K., Rothe, R., Scholz, R., Gneveckow, U., Wust, P., Thiesen, B., Feussner, A., von Deimling, A., Waldöfner, N., Felix, R., Jordan, A., 2007. Intracranial thermotherapy using magnetic nanoparticles combined with external beam radiotherapy: results of a feasibility study on patients with glioblastoma multiforme. *J. Neuro-oncol.* 81, 53–60.
- Mannucci, S., Ghin, L., Conti, G., Tambalo, S., Lascialfari, A., Orlando, T., Benati, D., Bernardi, P., Betterle, N., Bassi, R., Marzola, P., Sbarbati, A., 2014. Magnetic nanoparticles from Magnetosphaerium Gryphiswaldense increase the efficacy of thermotherapy in a model of colon carcinoma. *PLoS One* 9, e108959.
- Matsumine, A., Kusuzaki, K., Matsubara, T., Shintani, K., Satonaka, H., Wakabayashi, T., Miyazaki, S., Morita, K., Takegami Uchida, K.A., 2007. Novel hyperthermia for metastatic bone tumors with magnetic materials by generating an alternating electromagnetic field. *Clin. Exp. Metastasis* 24, 191–200.
- Mazzucchelli, S., Colombo, M., Verderio, P., Rozek, E., Andreatta, F., Galbiati, E., Tortora, P., Corsi, F., Prosperi, D., 2013. Orientation-controlled conjugation of haloalkane dehalogenase fused homing peptides to multifunctional nanoparticles for the specific recognition of cancer cells. *Angew. Chem. Int. Ed.* 52, 3121–3125.

- Nielsen, T.S., Jessen, N., Jørgensen, J.O.L., Møller, N., Lund, S., 2014. Dissecting adipose tissue lipolysis: molecular regulation and implications for metabolic disease. *J. Mol. Endocrinol.* 52, 199–222.
- Ogden, L., Yanovski, S.Z., Carroll, M.D., Flegal, K.M., 2007. The epidemiology of obesity. *Gastroenterology* 132, 2087–2102.
- Orlando, T., Mannucci, S., Fantechi, E., Conti, G., Tambalo, S., Busato, A., Innocenti, C., Ghin, L., Bassi, R., Arosio, P., Orsini, F., Sangregorio, C., Corti, M., Casula, M.F., Marzola, P., Lascialfari, A., Sberbati, A., 2016. Characterization of magnetic nanoparticles from *Magnetospirillum Gryphiswaldense* as potential theranostics tools. *Contrast Media Mol. Imaging* 11, 139–145.
- Otto, M.J., 2016. The safety and efficacy of thermal lipolysis of adipose tissue via ultrasound for circumference reduction: an open label, single-arm exploratory study. *Lasers Surg. Med.* 48 (8), 734–741.
- Pellegrino, T., Manna, L., Kudera, S., Liedl, T., Koktysh, D., Rogach, A.L., Keller, S., Radler, J., Natlle, G., Parak, W.J., 2004. Hydrophobic nanocrystals coated with an amphiphilic polymer shell: a general route to water soluble nanocrystals. *Nano Lett.* 4, 703–707.
- Ramirez-Zacarias, J.L., Castro Muñozledo, F., Kuri-Harcuch, W., 1992. Quantitation of adipose conversion and triglycerides by staining intracellular lipids with Oil red O. *Histochemistry* 97, 493–497.
- Renehan, A.G., Zwahlen, M., Egger, M., 2015. Adiposity and cancer risk: new mechanistic insights from epidemiology. *Nat. Rev. Cancer* 15, 484–498.
- Rutkowski, J.M., Stern, J.H., Scherer, P.E., 2015. The cell biology of fat expansion. *J. Cell Biol.* 208, 501–512.
- Santini, B., Zononi, L., Marzi, R., Cigni, C., Bedoni, M., Gramatica, F., Palugan, L., Corsi, F., Granucci, F., Colombo, M., 2015. Cream formulation impact on topical administration of engineered colloidal nanoparticles. *PLoS One* 10, e0126366.
- Schmittgen, T.D., Livak, K.J., 2008. Analyzing real-time PCR data by the comparative CT method. *Nat. Prot.* 3, 1101–1108.
- Sharifi, S., Daghighi, S., Motazacker, M., Badlou, B., Sanjabi, B., Akbarkhanzadeh, A., Rowshani, A., Laurent, S., Peppelenbosch, M., Rezaee, F., 2013. Superparamagnetic iron oxide nanoparticles alter expression of obesity and T2D-associated risk genes in human adipocytes. *Sci. Rep.* 3, 2173.
- Sneiderman, A.D., Cianflone, K., 1994. The adipin-ASP pathway and regulation of adipocyte function. *Ann. Med.* 26, 389–393.
- Varkouhi, A.K., Scholte, M., Storm, G., Haisma, H.J., 2011. Endosomal escape pathways for delivery of biologicals. *J. Controlled Release* 151, 220–228.
- World Health Organization, 2000. Obesity: Preventing and Managing the Global Epidemic: Report of a WHO Consultation on Obesity. World Health Organization, Geneva.
- Xu, H., Barnes, G.T., Yang, Q., Tan, G., Yang, D., Chou, C.J., Sole, J., Nichols, A., Ross, J.S., Tartaglia, L.A., Chen, H., 2003. Chronic inflammation in fat plays a crucial role in the development of obesity related insulin resistance. *J. Clin. Invest.* 112, 1821–1830.
- Zechner, R., Zimmermann, R., Eichmann, T.O., Kohlwein, S.D., Haemmerle, G.V., Lass, A., Madeo, F., 2012. FAT SIGNALS—lipases and lipolysis in lipid metabolism and signaling. *Cell Metab.* 15, 279–291.

### **Biomimetic Magnetic Nanocarriers optimization and functionalization**

- 1) PLGA Encapsulation and TAT peptide Functionalization of Biomimetic Magnetic Nanoparticles Increase their uptake in human brain glioblastoma (U87MG) and in mouse embryonic fibroblast (3T3L1) cell lines

BMNPs with sizes larger than most common superparamagnetic NPs were produced in the presence of MamC protein from *Magnetococcus marinus* MC-1. The biomimetic synthesis of BMNPs mediated by magnetosome membrane-associated proteins has emerged as an alternative to produce a magnetosome-like NP without the need of culturing magnetotactic bacteria (Prozorov et al., 2013). In particular, Mam-C is one of the magnetosome membrane-associated proteins that have been studied more thoroughly for the production of magnetic NPs. One of the advantages of MamC-mediated BMNPs is the fact that MamC attaches to the BMNPs surface and provides it with functional groups that allow functionalization based on electrostatic interactions. Moreover, the BMNPs are larger than conventional inorganic magnetites and this feature give them a larger magnetic moment (Garcia Rubia et al., 2018). To improve the biocompatibility of these NPs and avoid their oxidation they were enclosed in PLGA-based NPs and functionalized with transactivator of transcription (TAT) peptide. The TAT peptide is derived from human immunodeficiency virus and is a cell-penetrating peptide. Cell-penetrating peptides have been used to overcome the lipophilic barrier of the cellular membranes and deliver large molecules and even small particles inside the cells. NPs thermic profile was characterized and quantified and for the *in vitro* studies U87MG glioblastoma cell line was used and the cells were treated with different concentrations of BMNPs, PLGA-BMNPs and TAT-PLGA-BMNPs. The studies on the relationships between MNPs and the biological environment were mainly performed by light microscopy and transmission electron microscopy.

## II. Results

---

U87MG cell line (purchased by ATCC Manassas, VA), was cultured in Eagle's Minimum Essential Medium (EMEM) with 10% (v/v) FBS, 1% (w/v) Gln, 0.5% (v/v) AmpB, 100 units/ml of PS (Gibco, MA, USA), at 37°C in a 5% CO<sub>2</sub> humidified atmosphere. Medium and L-glutamine were purchased by Sigma-Aldrich (Italy), while serum and antibiotic mix were acquired by GIBCO Life Technologies (USA). 3T3L1 (ECACC, Sigma-Aldrich, St. Louis, MO, USA) were subcultured in Dulbecco's modified Eagle's medium nutrient mixture F12 containing 10% (v/v) FBS, 100 units/ml of PS (Gibco, MA, USA) at 37°C in a 5% CO<sub>2</sub> humidified atmosphere. Cells were trypsinized when subconfluent (about 80%) and seeded on 96 multiwell plastic microplates for cell viability evaluation, or on glass coverslips in 24-multiwell microplates for electron microscopy. Cells were treated with different concentrations of BMNPs, BMNPs enclosed in PLGA-based NPS NPs (50% Lactic acid and 50% Glycolic acid) and BMNPs enclosed in PLGA-based NPS NPs functionalized with TAT peptide. U87MG and 3T3L1 cells were seeded (3000 cells per well) in a 96-well plate and grown for 24h in a humidified incubator at 37°C with 5% CO<sub>2</sub>, then the medium was replaced with fresh medium containing NPs. The MTT assay (3-(4,5-dimethylthiazol-2-yl)-2,5-diphenyltetrazolium bromide) assay (Sigma) was used to evaluate the cytotoxicity of NPs after 2-24-48-72h. Absorbance was read by a microplate reader (CHROMATE 4300 Awareness Technology, USA). The test was conducted in triplicate. Statistical comparisons between treated and control samples were performed by using the KRUSKAL-WALLIS test. U87MG and 3T3L1 cells were grown as monolayers on glass coverslips, treated with 10  $\mu$ g/mL of NPs for 24h at 37°C, and then fixed with 2.5% (v/v) glutaraldehyde and 2% (v/v) paraformaldehyde in 0.1 M phosphate buffer, pH 7.4, at 4 °C for 1 h, post-fixed with 1% osmium tetroxide and 1.5% potassium ferrocyanide for 1 h, dehydrated with acetone and embedded in Epon resin. Ultrathin sections were observed in a Philips Morgagni transmission electron microscope (FEI Company Italia Srl, Milan, Italy) operating at 80 kV and equipped with a Megaview II camera for digital image acquisition.

## II. Results

Cell viability was evaluated after 2h, 24h, 48h, 72h after treatment at different concentrations with NPs with MTT test. U87MG cells, treated with TAT-PLGA-BMNPs, showed a significant decrease in viability after 48 and 72 hours after treatment at the concentrations of  $10 \mu\text{g/ml}$  and  $5 \mu\text{g/ml}$  (Figure 15); 3T3L1 showed a decrease only after 24 hours at the concentration of  $10 \mu\text{g/ml}$  (figure 12).

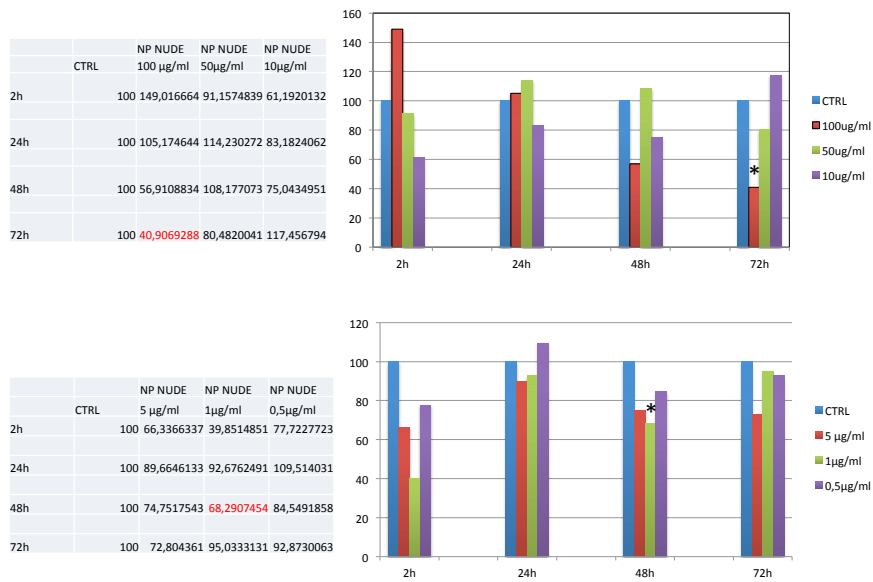


Figure 10. Viability (MTT assay) of 3T3L1 after incubation with different BMNPs concentrations for 2, 24, 48 and 72 h. Asterisks indicate significantly different values ( $P < 0.05$ ) between treated and control samples.

## II. Results

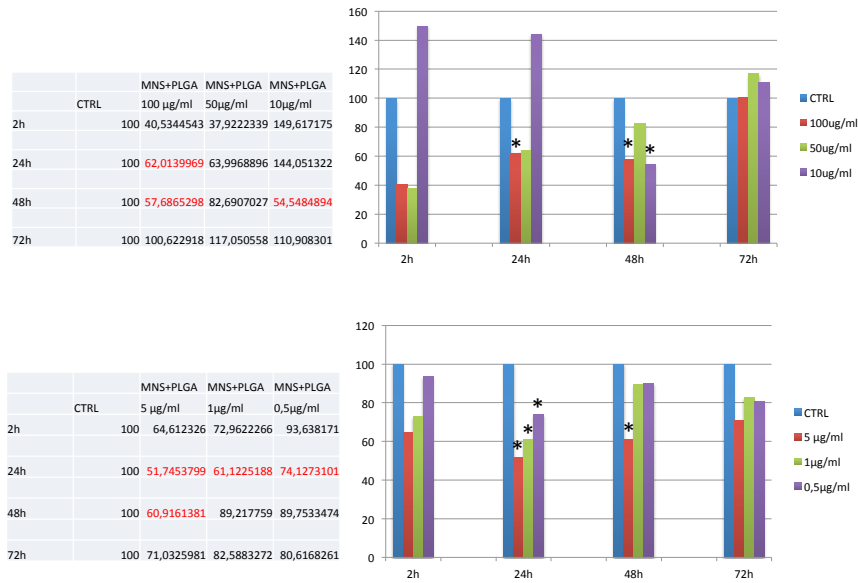


Figure 11. Viability (MTT assay) of 3T3L1 after incubation with different PLGA-BMNPs concentrations for 2, 24, 48 and 72 h. Asterisks indicate significantly different values ( $P < 0.05$ ) between treated and control samples.

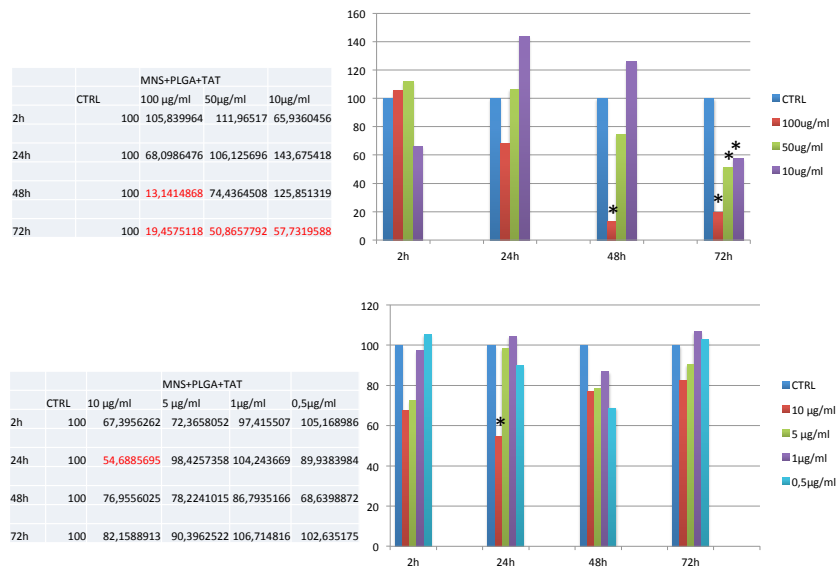


Figure 12. Viability (MTT assay) of 3T3L1 after incubation with different TAT-PLGA-BMNPs concentrations for 2, 24, 48 and 72 h. Asterisks indicate significantly different values ( $P < 0.05$ ) between treated and control samples.

## II. Results

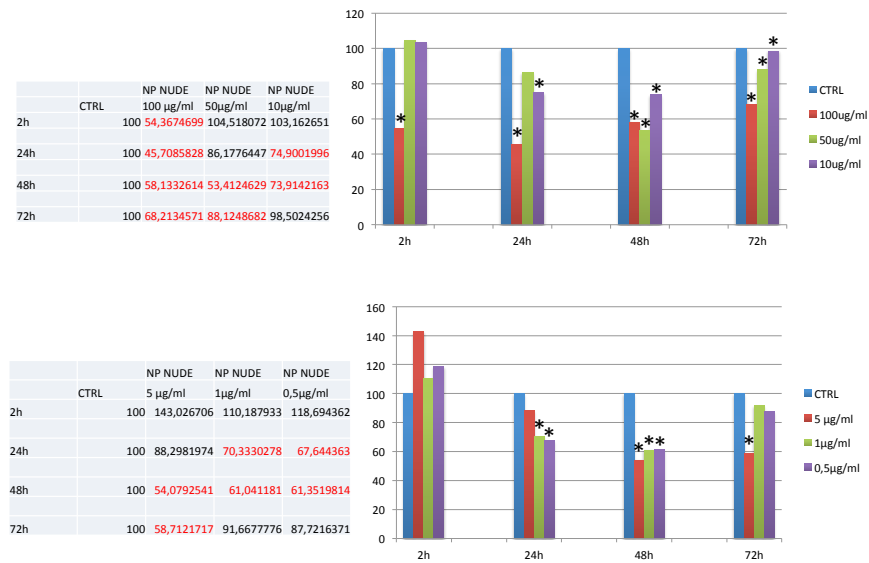


Figure 13. Viability (MTT assay) of U87MG after incubation with different BMNPs concentrations for 2, 24, 48 and 72 h. Asterisks indicate significantly different values ( $P < 0.05$ ) between treated and control samples.

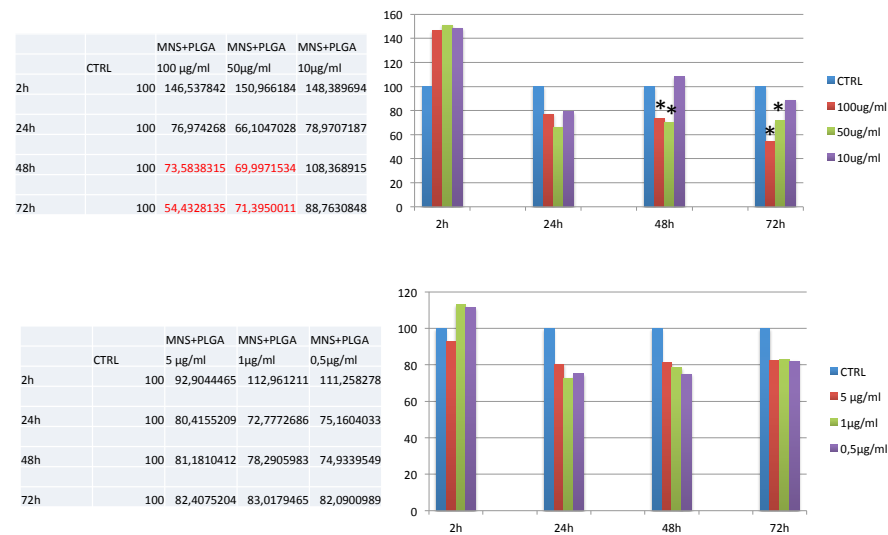


Figure 14. Viability (MTT assay) of U87MG after incubation with different PLGA-BMNPs concentrations for 2, 24, 48 and 72 h. Asterisks indicate significantly different values ( $P < 0.05$ ) between treated and control samples.

## II. Results

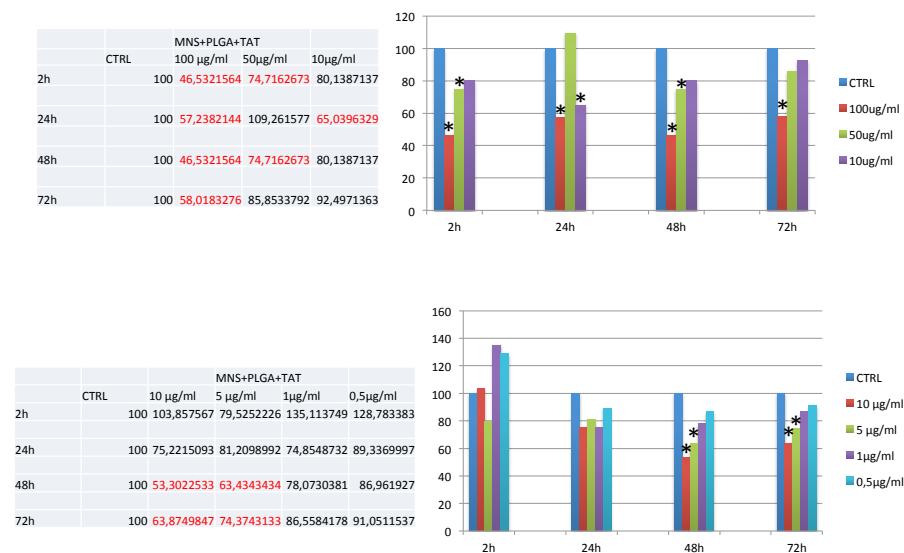


Figure 15. Viability (MTT assay) of U87MG after incubation with different PLGA-BMNPs concentrations for 2, 24, 48 and 72 h. Asterisks indicate significantly different values ( $P < 0.05$ ) between treated and control samples.

### *NPs uptake*

Ultrastructural analysis showed that these NPs enter inside the cells by endocytosis and phagocytosis, in the case of large clusters (figure 16a and b). As we expected, PLGA-based NPs functionalized with TAT peptide enter the cells in a larger amount in comparison to unfunctionalized PLGA-based NPs (data not shown). The TAT cell-penetrating peptides have been used to overcome the lipophilic barrier of the cellular membranes and deliver large molecules and even small particles inside the cell for biological actions. In the cytoplasm NPs are enclosed in a cytoplasmic vacuole (figure 16c).

## II. Results

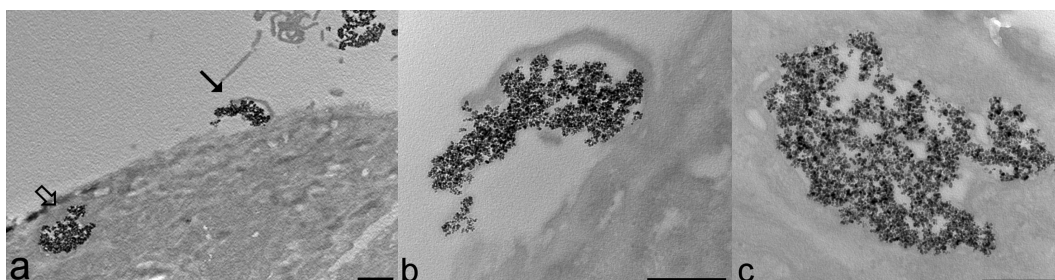


Figure 16. Transmission electron micrographs of a human fibroblast treated with nanoparticles for 24 h. a) Clusters of nanoparticles occur both at the surface (arrow) and inside (open arrow) the cell. b) High magnification of the nanoparticles at the cell surface (arrow in a): note the cell protrusion indicating a phagocytic process. c) High magnification of nanoparticles enclosed in a cytoplasmic vacuole (open arrow in a). Bars: 1000 nm (a), 500 nm (b,c).

### *Magnetic hyperthermia effect*

Solution of BMNPs is placed in the AMF apparatus (Figure 17), in an induction coil and exposed for 20 minutes to an alternated magnetic field (AMF) and a  $\Delta T$  of 4-5°C was registered. To assess temperature variation ( $\Delta T$ ), in the NPs solution, a multichannel thermometer equipped with optical fiber probes (FOTEMP4, Optocon AG, Germany) was used.



Figure 17. AMF apparatus (Magnetherm, nanoTherics, UK)

## II. Results

These results seem to indicate that BMNPs, synthesized with the protein MamC from magnetotactic bacteria are effective as heating mediators but they are toxic at concentrations higher than 5µg/ml for 3T3L1 and 1µg/ml for U87MG and at these concentrations we were not able to measure an increase of temperature in the medium by the digital IR camera (that is unable to measure fine  $\Delta T$ ) during the hyperthermic treatment. Since these NPs designed for thermotherapy that have been tested in this study are intended for in vivo administration, to have an effect in vivo, their biocompatibility or their hyperthermic profile should be improved. To this aim, BMNPs were enclosed in liposomes, and tested on glioblastoma cells at different concentrations (Figure 18).

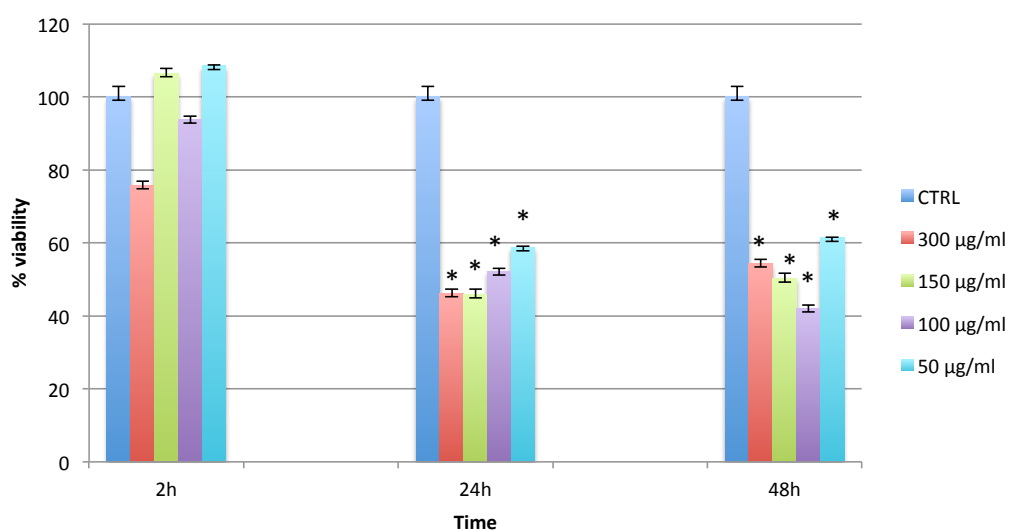


Figure 18. Viability (MTT assay) of HFL1 after incubation with different magnetoliposomes concentrations for 2, 24, 48 h. Asterisks indicate significantly different values ( $P < 0.05$ ) between treated and control samples.

### 2) Biomimetic Magnetic Nanocarriers Drive Choline Kinase Alpha Inhibitor inside Cancer Cells for Combined Chemo-Hyperthermia Therapy

**(Jabalera et al., 2019)**

Among the potential nanocarriers, magnetic nanoparticles have several advantages since they are biocompatible, their magnetic properties allow their guidance to the target site and they can be used as hyperthermia agents. BMNPs, mediated by *Magnetococcus marinus* MC-1 magnetosome membrane protein MamC, could be promising nanocarriers, able to couple with drugs forming stable nanoassemblies at physiological pH, while efficiently releasing the drug in acidic environment. In this second approach, BMNPs were coupled with a Choline kinase  $\alpha$  1 (ChoK  $\alpha$  1) inhibitor, Ff35. ChoK  $\alpha$  1 has been considered as biomarker of tumor progression (Glunde et al., 2011), (Cao et al., 2016) and could be a promising target in cancer therapy. ChoK catalyzes the phosphorylation of choline to generate phosphocholine which, through cytidine 5'-diphosphocholine (CDP-choline) (Van der Veen et al., 2017), produces phosphatidylcholine. ChoK  $\alpha$  1 also regulates the mitogen-activated protein kinase (MAPK) and phosphoinositide 3-kinase (PI3K/AKT) signaling pathways (Yalcin et al., 2010). Soluble Ff35 is capable of inhibiting choline uptake, making the inhibitor not selective for ChoK  $\alpha$  1. It is important to prevent the inhibition of choline uptake and a possibility is to use carriers to introduce the inhibitor inside the cells without interacting with the choline transporters. In this study we proposed to couple Ff35 with BMNPs in order to obtain a potential nanoassembly suitable for chemotherapy without side effects related to the inhibition of choline uptake. Moreover the use of hyperthermia is studied to increase the effect of chemotherapy. For the *in vitro* experiments the human hepatoblastoma cell line (HepG2) was used.

To take part to this work was possible thanks to my stay in Prof Concepcion Jimenez Lopez lab, at University of Granada,

## II. Results

---

### *BMNPs functionalization with Ff35-BMNPs:*

An aliquot of 5 mg of BMNPs was mixed with 1 mL of Ff35 100  $\mu\text{M}$  in HEPES buffer (10 mM HEPES, 150 mM NaCl, pH 7.2) for 6 hours under continuous stirring. After the incubation time, the Ff35-BMNPs nanoassemblies were collected with a magnet and washed twice with HEPES buffer. Then, the supernatants were measured by UV-Vis spectroscopy at a wavelength of 304 nm and these measurements were used to calculate the percentage of the absorbed compound. The molar absorptivity of Ff35 in HEPES buffer at 304 nm was determined as  $2677.5 \text{ L mol}^{-1}$  ( $R^2 = 0.9991$ ) from the slope of a standard calibration straight line.

### *Cell Culture*

The human hepatoblastoma HepG2 cell line was acquired from the European Collection of Animal Cell Cultures (Salisbury, UK). The cells were grown in Minimum Essential Medium (MEM) containing 10% heat-inactivated fetal bovine serum (FBS) supplemented with 2 mM l-glutamine, 1% nonessential amino acids, 100 U mL<sup>-1</sup> penicillin, and 100  $\mu\text{g mL}^{-1}$  streptomycin in a humid atmosphere with 5% CO<sub>2</sub> at 37 C.

### *Cell Viability Assay*

HepG2 cells were seeded onto 96-well plates (10000 cells/well) and grown in MEM/10% FBS for 24 h. After 24 h, the medium was removed and 100  $\mu\text{L}$  of fresh medium containing Ff35 (1, 5, and 10  $\mu\text{M}$ ), BMNPs (300  $\mu\text{g mL}^{-1}$ ), or Ff35-BMNPs (Ff35 1  $\mu\text{M}$  and BMNPs 300  $\mu\text{g mL}^{-1}$ ) were added for different time points. Cell viability was assayed by the MTT (3-(4,5-dimethylthiazol-2-yl)-2,5-diphenyltetrazolium bromide). Formazan crystals were dissolved in 100  $\mu\text{L}$  of DMSO, and the absorbance was read at a wavelength of 570 nm using a microplate reader (HTX Microplate Reader BioTek Instruments, Winooski, VT, USA).

## **II. Results**

HepG2 cells were grown in six-well dishes for 24 h. Then, BMNPs ( $300 \mu\text{g mL}^{-1}$ ) or Ff35-BMNPs (concentration of Ff35 was  $1 \mu\text{M}$  and BMNPs was  $300 \mu\text{g mL}^{-1}$ ) or only MEM/10% FBS medium, as a control, were added for 24 h. Cells were collected using trypsin and centrifuged at 1500 rpm for 5 min in MEM/10% FBS. Cell pellets were fixed in 2.5% glutaraldehyde and 2% paraformaldehyde in 0.05 M cacodylate buffer for 4 h at 4 C. The samples were washed three times with cacodylate buffer and postfixed in an aqueous solution of 1%  $\text{OsO}_4$  containing 1% potassium ferrocyanide for 1 h at 4 C in darkness. The following washes were done (25 C): 0.15% tannic acid in cacodylate buffer, cacodylate buffer, and  $\text{H}_2\text{O}$ . The samples were left in 2% uranyl acetate for 2 h and washed several times with  $\text{H}_2\text{O}$ . Then, dehydration in ethanol solutions rising from 50% to 100% was done at 4 C. The samples were embedded in resin (EMbed 812/100% ethanol (1/1)) for 60 min at room temperature, the same resin at a 2/1 ratio for 60 min, and then resin without ethanol overnight. For polymerization, the samples were incubated in pure resin for 48 h at 60 C. Ultrafine sections (50–70 nm) were cut using a Leica Ultramicrotome R and contrasted using 1% aqueous uranyl acetate for 5 min and lead citrate in a  $\text{CO}_2$ -depleted atmosphere for 4 min. A Zeiss Libra Plus 120 electron microscope was used to visualize the sections.

### *Hyperthermia Analysis*

Magnetic hyperthermia experiments were carried out using a laboratory-built AC current generator, based on a Royer-type oscillator. The AC source was connected to a double five-turn coil built with a copper tube 4 mm in diameter. This allowed control of the temperature of the coil by flowing thermostated water. The coil was 20 mm in diameter and 45 mm long. The magnetic field frequency was  $197 \pm 3$  kHz, and its strength was  $H = 21 \text{ kA/m}$  ( $B = 26.4 \text{ mT}$  in air) at the center of the coil, where the samples were placed, measured with a NanoScience Laboratories Ltd., Probe (Newcastle, UK), with  $10 \mu\text{T}$  resolution. All samples were previously prethermostated at 37 C. Prior to any determination, the adiabatic condition of the

system was verified by subjecting a sample of Milli-Q water as control, in order to

## II. Results

ensure that any temperature changes in the samples under study were due to the action of the magnetic field, and not a consequence of environmental temperature gradient. A preliminary experiment was performed with a suspension of bare BMNPs ( $300 \mu\text{g mL}^{-1}$ ) to set the conditions (frequency and strength of the field and time of application) needed to guarantee that a temperature of 43 C was reached. The sample temperature was determined with an optical fiber thermometer (Optocon AG, Dresden, Germany).

For actual hyperthermia experiments, HepG2 cells were incubated for 24 h at 37 C with either  $300 \mu\text{g mL}^{-1}$  BMNPs or Ff35-functionalized BMNPs and exposed to the AC magnetic field for time lapses ranging between 1 and 3 h. Immediately after the hyperthermia treatment, the cells were processed for the MTT test.

Cell viability was evaluated after 2h, 24h, 48h after treatment at different concentrations with NPs with MTT test. MTT assay reveals that Ff-35 BMNPs significantly decrease cell viability after 24h and 48h of treatment. HepG2 viability was not affected by the presence of BMNPs, which demonstrates the cytocompatibility of the BMNPs (Figure 7).

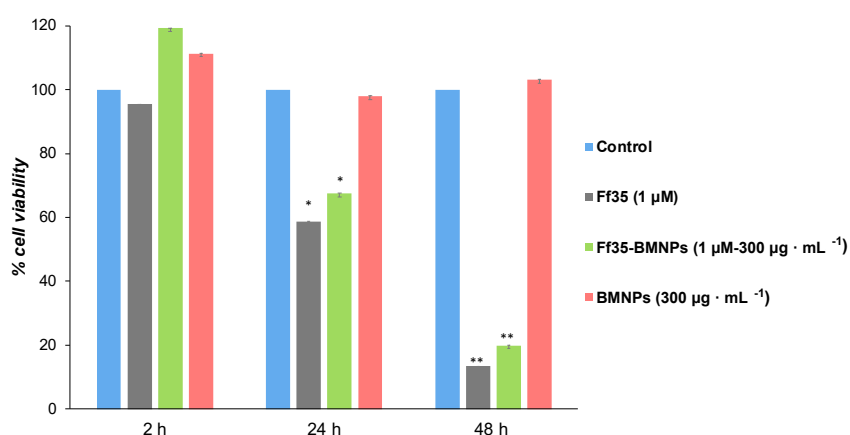


Figure 7 Cell viability was determined by MTT assay and normalized to that of the respective control cells. These experiments were performed twice in triplicate. \*  $p < 0.05$ ,

\*\* p < 0.001 compared to their respective controls.

---

## **II. Results**

TEM was used to visualize the internalization of BMNPs or Ff35-BMNPs (concentration of Ff35 was 1  $\mu\text{M}$  and BMNPs was 300  $\mu\text{g mL}^{-1}$ ), and to determine the possible morphological changes caused by Ff35-BMNPs exposure. Ultrastructural analysis by TEM showed that BMNPs were internalized by endocytosis (Figure 8). Control cells (Figure 8A and B) showed mitochondria having a dense matrix as well as many *cisternae* of rough endoplasmic reticulum

(ER) well structured, indicating absence of cell damage.

No ultrastructural cell damage was observed following BMNPs internalization until 24h incubation (Figure 8C and D). Both the BMNPs (Figure 8C and D) and Ff35-BMNPs (Figure 8E and F) were internalized via endocytosis and sorted into endosomes.

Cells treated with Ff35-BMNPs showed ultrastructural alteration (ultrastructural alteration, such as a notable dilatation of perinuclear space, loss of mitochondrial density and an abnormal shape. These experiments confirm the cell damage following the Ff35-BMNPs administration and explain why, while soluble Ff-35 inhibits Choline uptake, Ff-35-BMNPs do not. Soluble Ff-35 requires choline transporter to enter the cells, while Ff-35-BMNPs enter the cells by endocytosis.

## II. Results

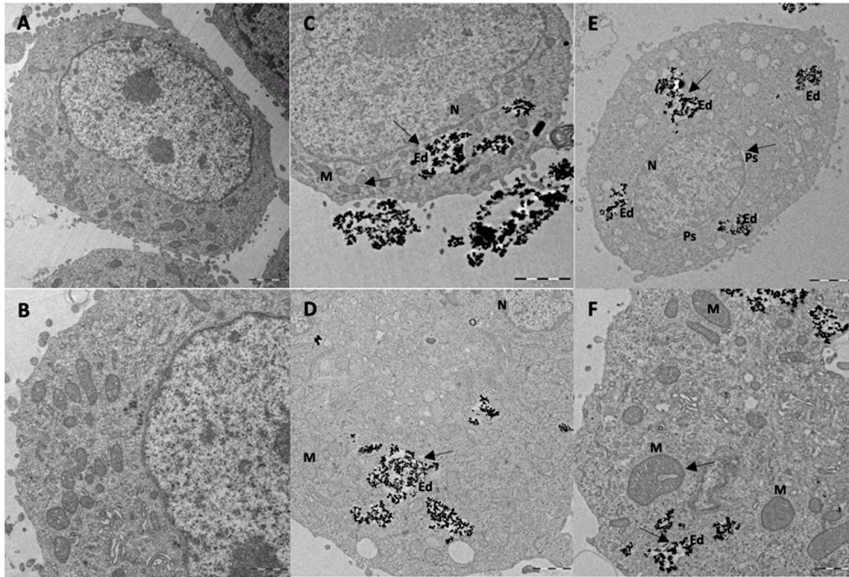


Figure 8 Internalization of BMNPs and Ff35-BMNPs. Ultrastructural alterations produced by Ff35-BMNPs. (A,B): Control HepG2 cells. (C,D): HepG2 cell exposed to BMNPs has ultrastructure similar to control cells.(E,F):TreatmentwithFf35 BMNPs (concentration of BMNPs was  $300\mu\text{g mL}^{-1}$  to control cells. Perinuclear space (Ps) is visible. The two nuclear membranes were separated showing a dilatation of the Ps. It is notably mitochondrial (M) rarefaction, disorganization, and dilatation. Both BMNPs and

Ff35-BMNPs were internalized by HepG2 cells via endocytosis and compartmentalized in endosomes (Ed). Scale bar corresponds to  $2\mu\text{m}$  (A,C,E) and  $1\mu\text{m}$  (B,D,F).

Figure 9 shows the effect of hyperthermia on cell viability. Hyperthermia reinforced cytotoxicity on both cells treated with BMNPs and much more on cells treated with Ff-35 BMNPs.

## II. Results

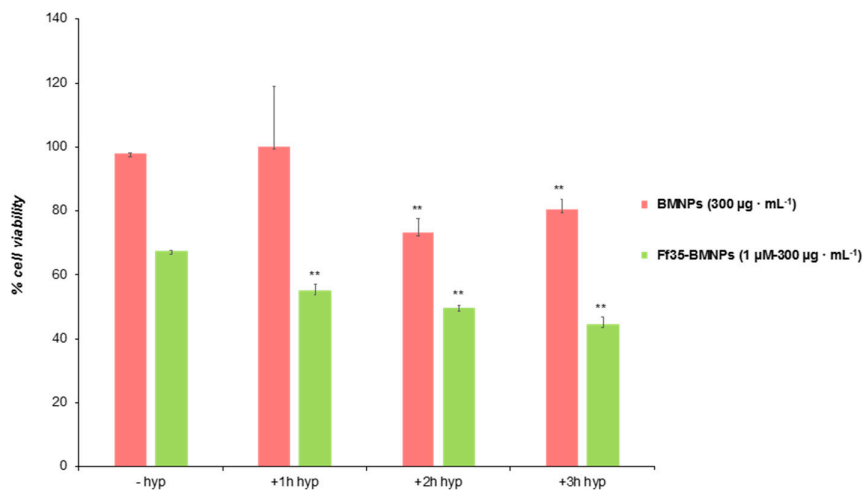


Figure 9 Effects of Ff-35 BMNPs and hyperthermia on Hep-G2 cells viability. Hep-G2 cells were incubated with MEM, 10% FBS with or without Ff35-BMNPs, (concentration of Ff35 was 1  $\mu\text{M}$  and BMNPs was 300  $\mu\text{g mL}^{-1}$ ) for 24 h, and exposed to an alternating magnetic field for 1,2,3 hours Cell number was determined by the MTT assay and expressed as percentage of control cells. Percentage of viability is normalized to that for the control cells. Results represent the mean  $\pm$  SEM of three independent experiments conducted in triplicate. \*\* $p < 0.001$ , when compared with their respective control values.

### **Colloidal polymer-coated Zn-doped iron oxide nanoparticles with high relaxivity and specific absorption rate for efficient magnetic resonance imaging and magnetic hyperthermia**

Several types of colloidal magnetic NPs have been designed and successfully developed over the past decades. Therefore, they have attracted huge attention in recent years for different biomedical applications, including bioimaging, drug delivery, and therapy, because of their unique intrinsic magnetic as well as physicochemical properties. Among them, superparamagnetic iron oxide nanoparticles (SPIONs) in the form of magnetite or maghemite nanocrystals have demonstrated promising performance as contrast agents for magnetic resonance imaging (MRI) and as heat mediators for magnetic hyperthermia. Magnetic hyperthermia is a promising non-invasive therapeutic modality for cancer treatment based on the production of heat from magnetic nanoparticles under an applied alternating magnetic field. The objective of our study was to develop an efficient SPIONs-based theranostic nanosystem with improved magnetic properties and colloidal stability for glioblastoma cell treatment. U87MG and HFL1 cell lines were used for the *in vitro* studies and the cells were treated with different concentrations of Zn-SPIONs. The studies on the relationships between MNPs and the biological environment were mainly performed by light microscopy and transmission electron microscopy.

## II. Results

---

U87MG cell line (purchased by ATCC Manassas, VA), was cultured in Eagle's Minimum Essential Medium (EMEM) with 10% (v/v) FBS, 1% (w/v) Gln, 0.5% (v/v) AmpB, 100 units/ml of PS (Gibco, MA, USA), at 37°C in a 5% CO<sub>2</sub> humidified atmosphere. Medium and L-glutamine were purchased by Sigma-Aldrich (Italy), while serum and antibiotic mix were acquired by GIBCO Life Technologies (USA). HFL1 cell line (purchased by ATCC Manassas, VA) was cultured in Dulbecco's modified Eagle medium with 10% (v/v) FBS, 1% (w/v) Gln, 0.5% (v/v) AmpB, 100 units/ml of PS (Gibco, MA, USA), at 37°C in a 5% CO<sub>2</sub> humidified atmosphere. Cells were trypsinized when subconfluent (about 80%) and seeded on 96 multiwell plastic microplates for cell viability evaluation, or on glass coverslips in 24-multiwell microplates for ematoxilin and eosin staining. U87MG and HFL1 cells were seeded (3000 cells per well) in a 96-well plate and grown for 24h in a humidified incubator at 37°C with 5% CO<sub>2</sub>, then the medium was replaced with fresh medium containing NPs. The MTT assay (3-(4,5-dimethylthiazol-2-yl)-2,5-diphenyltetrazolium bromide) assay (Sigma) was used to evaluate the cytotoxicity of NPs after 2-24-48-72h and to assess cell viability of U87MG cells after 2h of exposure to NPs and 20 minutes of exposure to an AMF. Absorbance was read by a microplate reader (CHROMATE 4300 Awareness Technology, USA). The test was conducted in triplicate. Statistical comparisons between treated and control samples were performed by using the KRUSKALL-WALLIS test. For transmission electron microscopy analysis of S1 NPs internalization U87MG cells were grown as monolayers on glass coverslips, treated with 10µgmL<sup>-1</sup> of S1 NPs for 24h at 37°C, and then fixed with 2.5% (v/v) glutaraldehyde and 2% (v/v) paraformaldehyde in 0.1 M phosphate buffer, pH 7.4, at 4 °C for 1 h, post-fixed with 1% osmium tetroxide and 1.5% potassium ferrocyanide for 1 h, dehydrated with acetone and embedded in Epon resin. Ultrathin sections were observed in a Philips Morgagni transmission electron microscope (FEI Company Italia Srl, Milan, Italy) operating at 80 kV and

## II. Results

---

equipped with a Megaview II camera for digital image acquisition.

To verify and quantify the thermic profile, NPs were placed in the AMF apparatus (Magnetherm, nanoTherics UK), in an induction coil and exposed for 20min to an alternated magnetic field (AMF). To assess temperature variation ( $\Delta T$ ), in the NPs solution, a multichannel thermometer equipped with optical fiber probes (FOTEMP4, Optocon AG, Germany) was used. Based on the results of cell viability and internalization tests U87MG cells were treated for 2h at 37°C with  $100\mu\text{g mL}^{-1}$  of S1 nanoparticles one day after seeding, placed in the induction coil and exposed for 20 minutes to an AMF (334 KHz, 2,2mT Field amplitude. Immediately after the treatment and after 24h cells were processed for ematoxilin and eosin staining or for MTT assay. To estimate the effect of hyperthermia, cells were fixed with 4% buffered formalin for 15 min, rinsed with PBS, cell nuclei were stained with Mayer's hematoxylin and the cythoplasm was counterstained with Eosin. In order to evaluate the occurrence of apoptotic cells, ten images of each sample were considered and the percentage of dead cells was evaluated making a comparison between the treated samples and the controls. U87MG cells were observed at 10x, 20x, and 40x magnification using an optical Olympus microscope (BX-URA2, Olympus optical, GMBH, Hamburg, Germany) equipped with Image ProPlus software (Media Cybernetics, Rockville, USA).

## II. Results

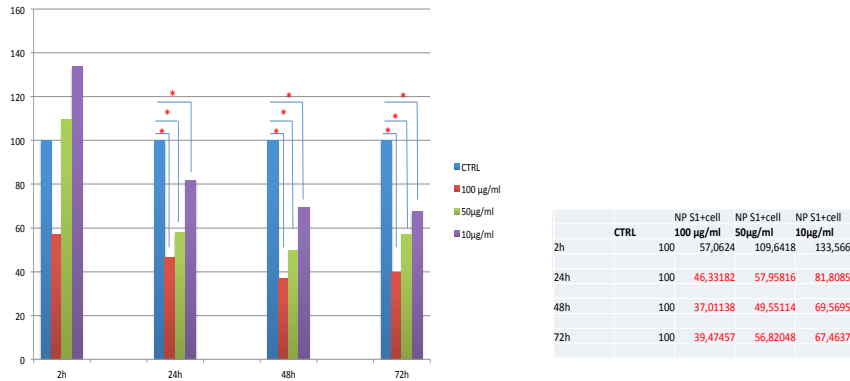


Figure 19. Viability (MTT assay) of HFL1 after incubation with different S1 NPs concentrations for 2, 24, 48 and 72 h. Asterisks indicate significantly different values ( $P < 0.05$ ) between treated and control samples. All the concentrations tested induced a significant increase in cell death; consequently, these concentrations were excluded from the subsequent experimentation.

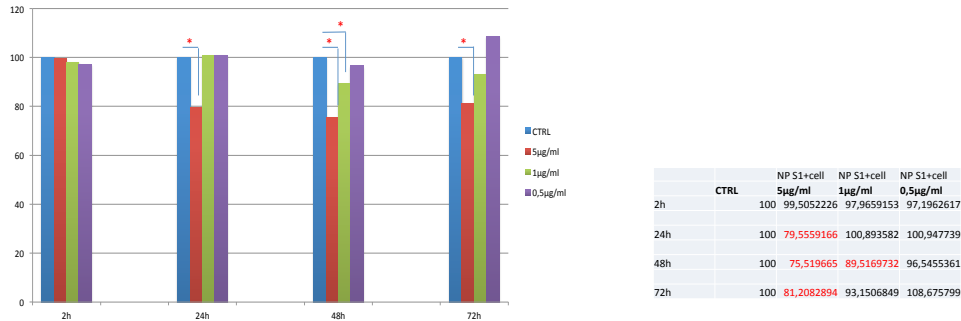


Figure 20. Viability (MTT assay) of HFL1 after incubation with different S1 NPs concentrations for 2, 24, 48 and 72 h. Asterisks indicate significantly different values ( $P < 0.05$ ) between treated and control samples. 5 µg/mL and 1 µg/mL concentrations induced a significant increase in cell death; consequently, these concentrations were excluded from the subsequent experimentations.

## II. Results

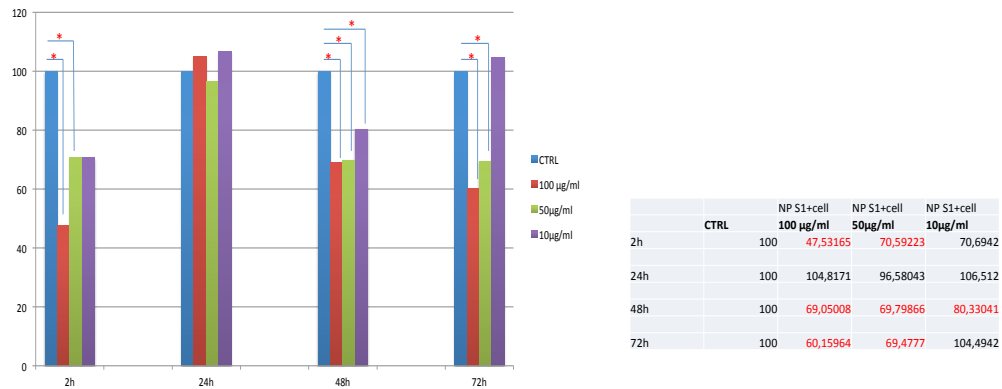


Figure 21. Viability (MTT assay) of U87MG after incubation with different S1 NPs concentrations for 2, 24, 48 and 72 h. Asterisks indicate significantly different values ( $P < 0.05$ ) between treated and control samples. All the concentrations tested induced a significant increase in cell death; consequently, these concentrations were excluded from the subsequent experimentation.

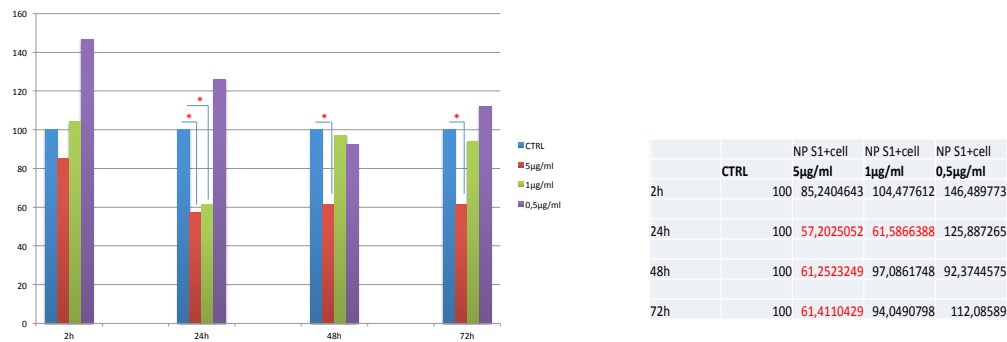


Figure 22. Viability (MTT assay) of U87MG after incubation with different S1 NPs concentrations for 2, 24, 48 and 72 h. Asterisks indicate significantly different values ( $P < 0.05$ ) between treated and control samples. 5 µg/mL and 1 µg/mL concentrations induced a significant increase in cell death; consequently, these concentrations were excluded from the subsequent experimentations.

## II. Results

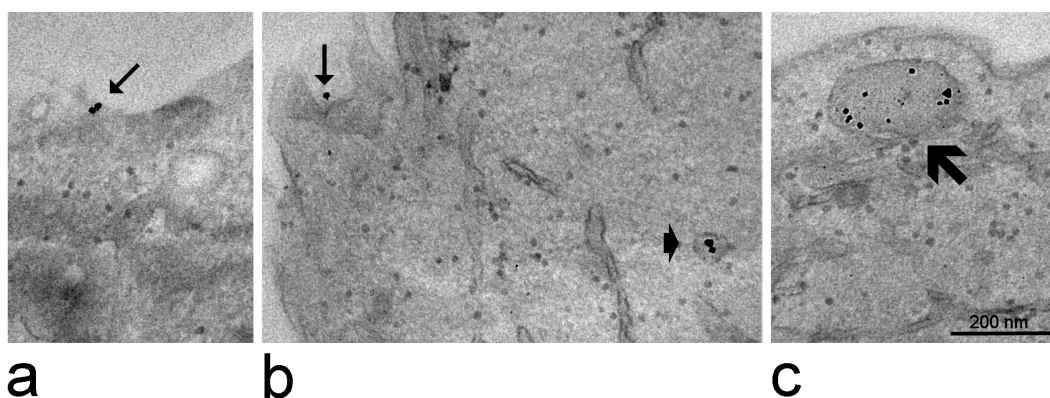


Figure 23. Transmission electron micrographs of U87MG cells incubated for 24 hours with S1 nanoparticles. (a) Two nanoparticles are adhering to the cell surface (arrow). (b) A nanoparticle occurs into a cell surface invagination (arrow), while two nanoparticles are enclosed in a small endosome (arrowhead). (c) A large vacuole (thick arrow), probably a secondary lysosome, contains many nanoparticles.

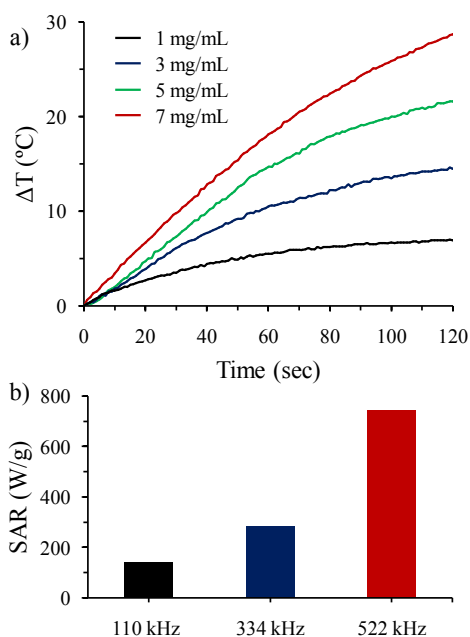


Figure 24. (a) Time-dependent temperature curves of polymer-coated Zn-SPIONs at different NP concentrations in water in presence of an external alternating magnetic field. (b) the calculated specific absorption rate (SAR) of polymer coated Zn-SPIONs as a function of the applied magnetic field.

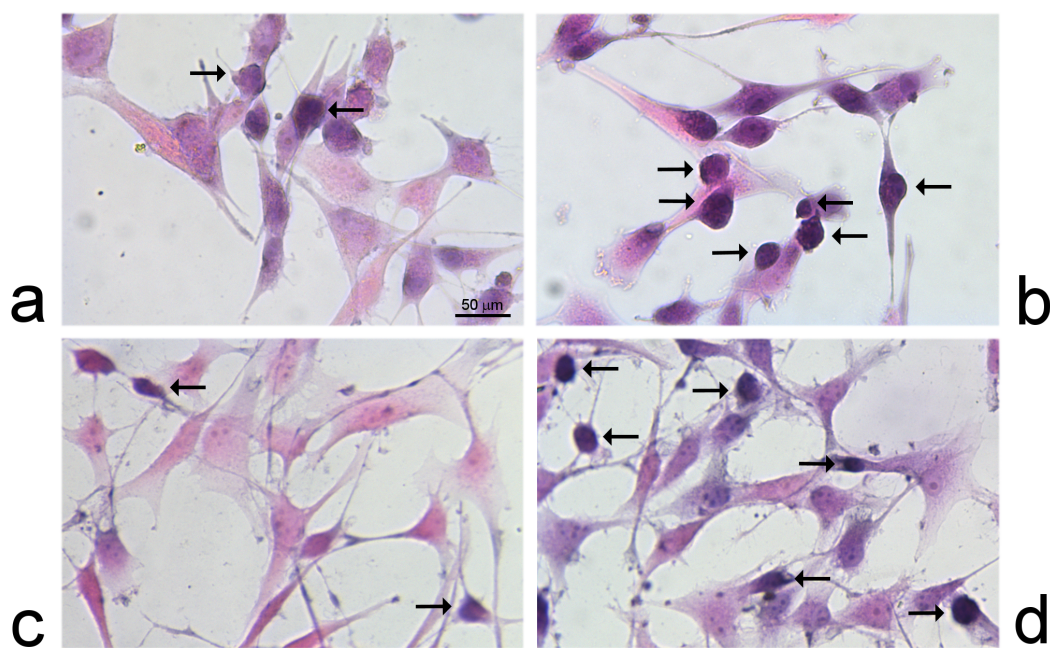


Figure 25. Light microscopy micrographs of U87MG cells. In **a** and **c** the cells were incubated for 24 hours with S1 nanoparticles and then placed in the induction coil without undergoing hyperthermic treatment. In **b** and **d** the cells were incubated for 24 hours with S1 nanoparticles, submitted to hyperthermia and observed immediately after (**b**) or after 24 h (**d**) from the treatment. Note the high number of dead cells (arrows) in **b** and **d** in comparison to **a** and **c**.

## II. Results

---

Several types of colloidal magnetic nanoparticles have been designed and successfully developed, and they have attracted attention in recent years for different biomedical applications because of their properties. Among them, superparamagnetic iron oxide nanoparticles (SPIONs) in the form of magnetite or maghemite nanocrystals have demonstrated promising performance as contrast agents as heat mediators for hyperthermia. We were able to see that after 24 h of incubation, the nanoparticles were distributed on the cell surface as well as in endosomes and lysosomes. Moreover, these results indicate that efficient SPIONs-based NPs were developed with magnetic properties for hyperthermic treatment of glioblastoma cells. In fact, an *in vitro* MH was performed to evaluate the efficiency of these Zn-SPIONs as heat mediators and the images showed a more pronounced cell death effect when the cells incubated with polymer-coated Zn-SPIONs were subjected to an alternating magnetic field in comparison with the unexposed sample. In conclusion, these NPs proved to be efficient in increasing both culture medium temperature and cell death rate as demonstrated by light microscopy analysis.

### **III. DISCUSSION**

---

### **III. Discussion**

---

Some Magnetic nanoparticles are known to generate heat because of molecular vibration in the presence of alternating magnetic field. SPIONs, approved by FDA for human use due to their good biodegradability (Kim et al., 2013) produce heat when subjected to an AMF (Jordan et al., 1993; Mannucci et al., 2014). In particular, PIOs proved to provide a good frequency-dependent heat capacity suitable for their use as hyperthermic mediators for our purposes. So far, SPIONs have been explored in the treatment of different tumors (Johannsen et al., 2007; Matsumine et al., 2007) since they are able to induce cell death. In our study MFH was applied at first to modulate lipid metabolism. The first step of the study was the selection of a PIOs concentration that could ensure the internalization and the absence of cell death or damage and at the same time was able to cause an increase of intracellular temperature on an alternating magnetic field. Immediately and 24h after PIOs administration cell organelle alteration was excluded with transmission electron microscopy analysis and we were able to demonstrate that, once internalized, PIOs remained confined in the cytoplasm, enclosed in vesicular structures. 3T3 adipocytes subjected to MFH not only remained vital up to 24 h post-treatment, but also showed well-preserved ultrastructural features and unaltered expression of genes involved in lipid metabolism. Our results therefore demonstrate that, if appropriately applied to 3T3 adipocytes, MFH can act as a mild controlled stress able to efficiently activate a physiological lipolytic process. PIOs proved to be safe and effective for MFH also in hADAS cells. These cells internalized lower amounts of PIOs in comparison to 3T3 adipocytes, probably because metabolic activity of cultured primary cells is reduced in comparison to established cell lines. Nevertheless, despite the lower amounts of accumulated PIOs MFH induced a marked delipidation in hADAS cells. In 3T3 adipocytes, this lipid loss occurs immediately after MFH while in hADAS it becomes evident after 24 h from treatment: this difference may be related to various factors, such as the reduced uptake of PIOs or the different content of lipid droplets in hADAS cells or to species-specific differences. Anyway, the positive results obtained in hADAS cells, although still preliminary, provide a promising experimental

### III. Discussion

---

background for future applications of MFH to human adipose tissue. It is worth noting that, similarly to many other nanoparticles, SPION surface may be functionalized and their distribution controlled by targeting strategies, thus focusing the hyperthermic treatment in specific tissues. Our study therefore represents an original starting point to advance in the research aimed at counteracting obesity and the multiple pathologies associated.

Magnetic fluid hyperthermia finds its applications also in the treatment of different types of cancers previously loaded with magnetic nanoparticles and exposed to an alternating magnetic field.

SPIONs have demonstrated promising performance as mediators for magnetic hyperthermia. Nowadays, SPIONs-based MH is clinically approved in Europe as an adjuvant therapy for recurrent glioblastoma multiforme and several clinical trials are still ongoing for other cancer types (Mahmoudi et al., 2018; Chang et al., 2018). However, the low magnetic properties of nanoparticles available for preclinical and clinical studies cause poor heating efficiency, that leads to a low specific absorption rate SAR (Das et al., 2019; Hervault et al., 2014). As a result, very high dosages of SPIONs are needed to accomplish high performances in cancer therapy. The objective of our study was to develop an efficient SPIONs-based nanosystem with superior magnetic properties and improved colloidal stability for glioblastoma cell treatment. Iron(III) ions in the tetrahedral sites of inverse spinel structure of  $\text{Fe}_3\text{O}_4$  were partially replaced by non-magnetic zinc(II) ions (Abenojar et al, 2016; Jang et al., 2009). Then, the synthesized non-spherical zinc-doped superparamagnetic iron oxide nanoparticles (Zn-SPIONs) were successfully coated with an amphiphilic polymer producing water dispersible nanoparticles that exhibited high colloidal stability in biological media. The results of the evaluation of contrast enhancement abilities of polymer-coated Zn-SPIONs for MRI performed measuring the longitudinal ( $T_1$ ) and transverse ( $T_2$ ) relaxation times of water protons as a

### III. Discussion

---

function of iron molar concentration with a 0.47 T NMR relaxometer demonstrated that nanoformulations efficiently reduced both  $T_1$  and  $T_2$ .  $r_1$  and  $r_2$  values were calculated and the observed  $r_2$  value is larger compared to previously reported SPION-based contrast agents, including commercially available Resovist®. (Shen et al., 2017; Lee et al., 2011; Lee et al., 2012) This superior performance is presumably due to the high saturation magnetization and the unique surface chemistry of polymer coated Zn-SPIONs. Zn-SPIONs exhibited the capability to increase the solution temperature by 4-7 °C within 120 s exposure, which is sufficient for MH. Furthermore, the essential temperature (41-46 °C) for moderate hyperthermia was easily achieved using highly concentrated Zn-SPIONs solutions (*e.g.*, 7 mgmL<sup>-1</sup>) in a very short time (few seconds), depending on the nanoparticle concentration and magnetic field strength (H) and frequency. The heating capacity was demonstrated to be dependent on the properties of the magnetic field. The heating efficiency of polymer-coated Zn-SPIONs was quantitatively evaluated by its specific absorption rate (SAR). SAR values were higher than the ones previously reported for most SPIONs (Das et al., 2019; Marinozzi et al., 2017,) suggesting that our Zn-SPIONs with improved heating efficiency may lower the dosage required for MH purposes.

The produced heat from Zn-SPIONs-labeled U-87 MG cells efficiently killed cancer cells when exposed to an alternating magnetic field in the biological safe range. In conclusion, this system could be proposed as a valid tool for cancer

### III. Discussion

---

theranostics, especially for glioblastoma. The coating polymer confers the additional advantage of allowing straight forward functionalization with targeting ligands and drug conjugation, which could allow combination therapy.

The biomimetic synthesis of magnetosome-like magnetite nanoparticles (BMNPs) mediated by membrane-associated proteins has emerged as an alternative to produce a magnetosome-like nanoparticle without the need of culturing magnetotactic bacteria (Prozorov et al., 2013). In particular, in the study described above, BMNPs with a magnetosome membrane-associated protein (MamC from *Magnetococcus marinus*) were produced. This protein controls magnetite nucleation and/or growth, altering the size and morphology of crystals. One of the advantages of MamC-mediated BMNPs is the fact that MamC attaches to the BMNPs surface and provide them functional groups that allow functionalization based on electrostatic interactions (Gracia Rubia et al., 2018). The study showed that BMNPs, since they are magnetic, could be guided to the target site under the application of continuous magnetic field; moreover, there is the possibility to use them as hyperthermia agents. It was possible to combine the cytotoxic effect of the molecule, bound to the NPs surface, with the cytotoxic effect induced by hyperthermia and to trigger the release of the drug from the BMNPs. Finally, the coupling between ChoK $\alpha$ 1 inhibitor offers the potential of Ff35 entering the cell independently of the choline transporters. This is crucial, as the coupling of Ff35-BMNPs allows the compound to exert a cytotoxic activity comparable to that of the soluble compound avoiding the secondary effect due to the inhibition of choline uptake. It provides also a protocol that could be used with other molecules to disentangle the cytotoxic effect of the drug due to the enzyme inhibition and/or inhibition of choline uptake. Therefore, the novel design of the nanoassemblies of Ff35-BMNPs showed in the study and the demonstration of the activity of such a compound without interfering in the choline uptake are important results, as they would allow the potential use of these ChoK $\alpha$ 1 inhibitors as antitumoral drugs

### III. Discussion

---

that would otherwise be compromised. Several studies have shown that these NPs exhibit low to no toxicity in humans due to their possible degradation in the liver and spleen, which results in the release of Fe<sup>3+</sup> ions that participate in iron metabolism (Mou et al., 2015).

To improve the biocompatibility on glioblastoma cells, BMNPs were enclosed in poly(lactic-co-glycolic acid) (PLGA)-based NPs (50% glycolic acid and 50% lactic acid). Among the various polymeric materials, PLGA, a pharmaceutical excipient in the US Pharmacopeia and National Formulary (USP/NF) monograph, has become very popular in drug delivery systems due to its modified particle sizes, stable solid structure, facile surface functionalization, and excellent biocompatibility and biodegradability (Hamdy et al., 2011; Bowerman et al., 2017). Moreover, surface modification of PLGA NPs with functional polymers can confer them additional favorable characteristics. In our study, PLGA NPs were functionalized with TAT peptide. Studies have shown that cell-penetrating peptides play an important role in carrying molecules across body barriers (Farkhani et al., 2014). In fact TAT-PLGA-BMNPs are efficiently internalized inside U87MG cells.

Moreover, MNPs proved to induce cytotoxicity *via* hyperthermia in single cells and these data -although obtained under *in vitro* conditions only- suggest that these NPs may be potentially suitable therapeutic tools. However, the biocompatibility of these nanocarriers needs to be improved to envisage a safe administration in patients.

In conclusion, all the studies described supported evidence on the efficacy of different magnetic nanoparticle-mediated hyperthermic treatment for multiple therapeutic purposes. However, magnetic nanoparticles are made of potentially toxic components and their formulation as well as their administration conditions must be carefully evaluated in appropriate experimental models to design a safe utilization for medical purposes. In this view, this work described represents the first step of a long but promising way.

## **IV. APPENDIX**

---

## **IV. Appendix**

---

During my Doctoral program, besides my research on hyperthermic nanoparticles for biomedical applications, I gave my contribution to two collaborative studies:

- In the frame of a collaboration with Prof. Pasquina Marzola (Department of Informatics, University of Verona, Italy) liposomes functionalized with doxorubicine and bombesine analogue peptide were tested in mice bearing xenografts of PC-3 cells. My task was to culture cells and make histological analysis.
- In the frame of a collaboration with Dott. Silvia Arpicco and Dott. Barbara Stella (Department of Drug Science & Technology, University of Turin, Italy) Liposomes, mesoporous silica NPs (MSN), and two different formulations of Poly Lactic-co-Glycolic Acid (PLGA) NPs (50% lactic acid and 50% glycolic acid [PLGA 50:50], and 75% lactic acid and 25% glycolic acid [PLGA 75:25]) were tested on the murine myoblast cell line C2C12. My task was to culture cells and prepare the samples for confocal microscopy and transmission electron microscopy.

As a result of these collaborative researches, two scientific articles were published (the articles have been reproduced with the permission of the journals' Publishers).

*A. Accardo, S. Mannucci, E. Nicolato, F.Vurro, C. Diaferia, P. Bontempi, P. Marzola, G.Morelli (2018). Easy formulation of liposomal doxorubicin modified with a bombesin peptide analogue for selective targeting of GRP receptors overexpressed by cancer cells, Drug Delivery and Translational Research, 9:215–226, DOI: 10.1007/s13346-018-00606*



## Easy formulation of liposomal doxorubicin modified with a bombesin peptide analogue for selective targeting of GRP receptors overexpressed by cancer cells

Antonella Accardo<sup>1,2</sup> · Silvia Mannucci<sup>3</sup> · Elena Nicolato<sup>3</sup> · Federica Vurro<sup>3</sup> · Carlo Diaferia<sup>1</sup> · Pietro Bontempi<sup>4</sup> · Pasquina Marzola<sup>4</sup> · Giancarlo Morelli<sup>1,2</sup>

Published online: 19 December 2018  
© Controlled Release Society 2018

### Abstract

The article concerns the obtainment of liposomal doxorubicin (Dox) in which liposomes are externally modified with a targeting peptide able to drive the formulation in a selective way on membrane receptors overexpressed in tumors. We developed a kit composed by three different vials: (A) a vial containing a sterile, translucent, red dispersion of the liposomal doxorubicin drug (Doxil®), (B) a vial filled with a lyophilized powder of a modified phospholipid with a reactive function (DSPE-Peg-maleimide), and (C) a vial containing a 1–9 bombesin peptide analogue (Cys-BN-AA1) chemically modified to react in stoichiometric ratio respect to DSPE-Peg-maleimide. The chosen peptide is a stable analogue antagonist of the wild-type 1–9 bombesin peptide; it is very stable in serum; maintains high specificity, with nanomolar affinity, towards gastrin release peptide receptors (GRPRs indicated also as BB2); and is overexpressed in some cancer cells. Results on animal studies clearly indicate that in mice treated with the kit product (i.e., pegylated liposomal Dox modified with the bombesin analogue, Doxil-BN-AA1), tumor growth is reduced, with an improved efficacy respect to mice treated with non-modified pegylated liposomal Dox or with saline solution.

**Keywords** Bombesin peptide · Liposomes · Doxorubicin delivery · Anticancer efficacy · Formulation kit

### Introduction

Therapeutic effectiveness of many drugs, especially for antitumoral ones, is influenced by their pharmacokinetic profiles. Inefficient delivery affects the total bioavailability dose and it can be the cause of severe adverse effects on non-target organs [1]. To overcome these problems, nanostructured drug delivery tools were designed and proposed. Liposomes are some

of the most common and well-investigated nanocarriers for drug delivery [2–5]. They are able to improve the efficacy and the safety of many therapeutic compounds by stabilizing the active principle, overcoming obstacles to cellular and tissue uptake, and improving their biodistribution curves in the target sites in vivo.

Liposomes are phospholipid vesicles consisting of one (monolamellar) or more (oligo- and multilamellar) concentric lipid bilayers enclosing discrete aqueous compartments. Prepared using different lipid compositions and different formulation procedures, monolamellar liposomes are classified according to their dimensions as small (<100 nm, small unilamellar vesicles, SUV), medium (100–250 nm, medium unilamellar vesicles, MUV), and large (>250 nm, large and giant unilamellar vesicles, LUV and GUV respectively). According to their surface charge nature, they can be categorized as neutral, cationic, or anionic too. Their large aqueous cavity allows them to encapsulate and deliver drugs and macromolecules, such as nucleic acids [6], peptides [7], and imaging agents [8, 9]. In addition, liposomes present unique characteristics as pharmaceutical systems such as biocompatibility, capacity for self-assembly, ability to carry large drug

✉ Pasquina Marzola  
pasquina.marzola@univr.it

✉ Giancarlo Morelli  
gmorelli@unina.it

<sup>1</sup> Department of Pharmacy and Interuniversity Research Centre on Bioactive Peptides (CIRPeB), IBB CNR, University of Naples “Federico II”, via Mezzocannone 16, 80134 Naples, Italy

<sup>2</sup> Invectors srl, Naples, Italy

<sup>3</sup> Department of Neurological Biomedical and Movement Sciences, University of Verona, Str. Le Grazie 8, 37134 Verona, Italy

<sup>4</sup> Department of Computer Science, University of Verona, Str. Le Grazie 15, 37134 Verona, Italy

payloads, protection of the encapsulated compounds from early inactivation, degradation, and dilution in the circulation. Moreover, a wide range of their physicochemical and biophysical properties can be modified in order to control their biological characteristics. For example, the external modification of vehicle surface with a protective crown of polyethylene glycol (PEG) polymer increases the in vivo circulation time of the entire drug, giving “stealth liposomes” [10–12]. Notwithstanding the large literature concerning the development of liposomes as drug delivery systems, and presenting interesting results both in vitro and in animal studies, only a limited number of compounds reached the clinic.

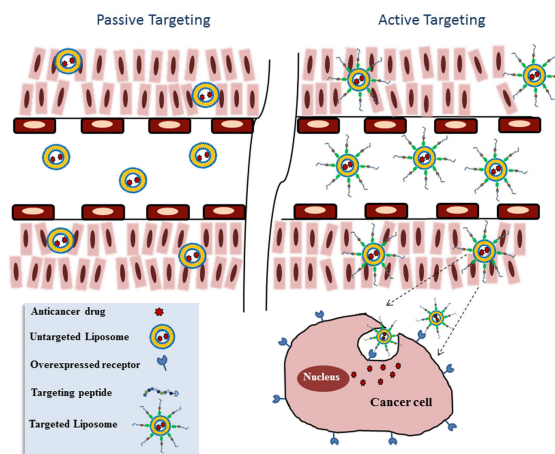
Another peculiar characteristic of liposomes as drug delivery systems is the possibility to modify their external surface with targeting moieties such as peptides [13] or antibodies [14, 15], producing targeted liposomal drugs. The presence of a targeting molecule changes the delivery properties of the carriers going from a passive targeting to an active one. Indeed, generally untargeted liposomes reach the target using the fenestrations present around the tumor sites, using the well-known enhanced permeability and retention (EPR) effect [12]. On the contrary, liposomes modified with targeting molecules, able to bind the target cells by using specific receptors overexpressed by cancer cells (see Fig. 1), strongly raise drug delivery efficacy and selectivity on the site of interest [3, 13].

An extensive number of liposomes externally modified with targeting peptides have been proposed as target selective drug delivery systems for cancer therapy [16–20]. They essentially differ each other for the following properties: (i) the liposome components, (ii) the encapsulated anticancer

drug, (iii) the targeting exposed peptide, (iv) the amount of peptide on the liposome surface, and (v) the preparation mode. Most of the selected peptides were chosen for their ability to bind with high affinity receptors overexpressed by cancer cells. A lot of different receptor targets for peptides are overexpressed on both cancer vasculature and cancer cells. Strong interest has been devoted in targeting receptors of integrins [3, 21, 22], growth factor receptors [23–25], and G protein coupled receptors [3, 9, 14, 17]. Two different strategies have been proposed for the introduction of the targeting peptides on the liposome surface: according to a pre-formulation mode, an amphiphilic peptide is introduced directly during liposome preparation, while applying a post-formulation strategy the peptide is bound to a modified surface of a preformed liposome. Very interesting in vitro and in vivo results have been obtained by modulating different factors in design and in preparation of the peptide modified liposomal drugs. It is well known from literature that peptide modified liposomal drugs have higher efficacy in vivo respect to the same system lacking of the targeting peptide [3, 14]. Despite the efforts in designing and in studying of peptide modified liposomal drugs, any compound of this class has still reached the clinic until now. This evidence could be essentially due to two different factors: (1) the difficulty in the industrial scaling up of the peptide modified liposomal drug that also accomplish the regulatory issues and (2) the fate of the exposed peptide after in vivo administration that is often unpredictable.

In this paper, we report the development of a novel peptide modified liposomal drug in which the preparation mode should favor an easy industrial preparation, while the in vivo

**Fig. 1** Passive versus active targeting of liposomal drugs and peptide modified liposomal drugs, respectively. In tumor tissues, blood vessels undergo rapid proliferation around tumor site and the large vascular fenestrae and the impaired lymphatic drainage promote extravasation of exogenous liposomal drugs. After extravasation, targeted liposomes, exposing a bioactive peptide on their surface, are able to bind the membrane receptors overexpressed by cancer cells, thus promoting intracellular uptake by receptor-mediated endocytosis and an accumulation of the active drug



efficacy in animals should encourage translation to the human studies. The studied compound is the liposomal doxorubicin (Dox) modified with a bombesin analogue peptide able to target GRP (gastrin releasing peptide) receptors [26–28]. The overexpression of GRP receptors is well documented in several tumor types [29–32]. In particular, these receptors have been found overexpressed not only in prostate cancer [33–35] but also in ovarian cancer and in estrogenic positive breast cancers [36–38]. Experimental evidence indicates that bombesin peptide promotes breast cancer progression and growth. In more details, a synergistic effect between GRP receptors and epidermal growth factor (EGF) receptors was detected in a human breast cancer cell lines (MDA-MB-231), regulating cell migration and Interleukin-8 (IL-8) expression. No effect was found on proliferation [39].

According to an easy procedure based on a kit, targeted liposomal drug is prepared starting from pegylated liposomal Dox (Doxil®), an approved liposomal formulation.

## Materials and methods

### Instrumentation

Preparative RP-HPLCs were carried out on a LC8 Shimadzu HPLC system (Shimadzu Corporation, Kyoto, Japan) equipped with a UV lambda-Max Model 481 detector using a Phenomenex (Torrance, CA) C4 (300 Å, 250 × 21.20 mm, 5 µm) column eluted with an H<sub>2</sub>O/0.1% trifluoroacetic acid (TFA) (A) and acetonitrile CH<sub>3</sub>CN/0.1% TFA (B) from 5 to 70% over 30 min at 20 mL/min flow rate. Analytical HPLCs were carried on a LC8 Shimadzu HPLC system (Shimadzu Corporation, Kyoto, Japan) equipped with a UV lambda-Max Model 481 detector using a C18 Column (Jupiter, Phenomenex 150x25mm); eluents: H<sub>2</sub>O/0.1% TFA (A) and CH<sub>3</sub>CN /0.1% TFA (B); method from 5% (B) to 70% (B) over 10 min at 250 µL/min; and UV revelation at 210 nm. LC-MS analyses were performed by using Finnigan Surveyor MSQ single quadrupole electrospray ionization (Finnigan/Thermo Electron Corporation San Jose, CA). UV measurements were performed on a UV-Vis Jasco V-5505 spectrophotometer equipped with a Jasco ETC-505T Peltier temperature controller with a 1.0-cm quartz cuvette (Hellma). Emission fluorescence spectra were recorded at room temperature using a Jasco Model FP-750 spectrofluorimeter in 1.0 cm path length quartz cell. Equal excitation and emission bandwidths were used throughout experiments, with a recording speed of 125 nm/min and automatic selection of the time constant. To analyze the tryptophan fluorescence, emission spectra were recorded between 290 and 450 nm using an excitation wavelength of 280 nm.

### Pharmaceutical materials and reagents

Protected N<sup>α</sup>-Fmoc-amino acid derivatives, coupling reagents, and Rink amide MBHA resin were purchased from Calbiochem-Novabiochem (Laufelfingen, Switzerland). Fmoc-21-amino-4,7,10,13,16,19-hexaoxaheneicosanoic acid (Fmoc-Ahoh-OH) was purchased from Neosystem (Strasbourg, France). Doxorubicin hydrochloride (Dox•HCl) was obtained from Sigma Chemical Co. (St. Louis, MO, USA). DSPE-Peg2000-maleimide ammonium salt was purchased from Avanti Polar Lipids (Alabaster, AL, USA). Pegylated liposomal Dox (commercial name of Doxil®) vials, containing 25 mL of solution, were kindly gifted by the Italian Cancer Institute in Naples (Italy) “Fondazione G. Pascale.” All the other chemicals were commercially available by Sigma-Aldrich, Fluka (Bucks, Switzerland) or LabScan (Stillorgan, Dublin, Ireland) and were used as received unless otherwise stated. All solutions were prepared by weight using doubly distilled water.

### Peptide synthesis and chemical details

Synthesis of H-Cys-Ahoh-DPhe-Gln-Trp-Ala-Val-N (Me)Gly-His-Sta-Leu-NH<sub>2</sub> (Cys-BN-AA1). Synthesis of Cys-BN-AA1 was carried out in solid-phase under standard Fmoc strategy [40]. Rink-amide MBHA resin (0.78 mmol/g, 0.5 mmol scale, 0.640 g) was used. The elongations of BN-AA1 peptide (sequence: H-DPhe-Gln-Trp-Ala-Val-N (Me)Gly-His-Sta-Leu-NH<sub>2</sub>) were achieved by sequential addition of Fmoc-aa-OH with benzotriazol-1-yl-oxytrityrrolidinophosphonium hexafluorophosphate/1-hydroxy-1,2,3-benzotriazole/*N,N*-diisopropylethylamine (PyBOP/HOBt/DIPEA) (1:1:2) as coupling reagents, in *N,N*-dimethylformamide (DMF) in pre-activation mode. All couplings were performed twice for 1 h, by using an excess of 4.0 equivalents for the single amino acid derivative. Fmoc deprotections were obtained by 30% solution of piperidine in DMF. When the peptide synthesis was complete, the Fmoc N-terminal protecting group was removed and a monodisperse residue of Fmoc-Ahoh-OH was condensed in a single coupling using an excess of two equivalents. After the Fmoc removal, Fmoc-Cys (Trt)-OH (1.170 g, 2.0 mmol) was coupled on the resin stirring the slurry suspension in standard conditions. The N-terminal Fmoc protecting group was removed and peptide derivative was cleaved from the resin with TFA (5 mL) containing 2.5% (v/v) water and 2.0% (v/v) triisopropylsilane (TIS) as a scavenger at room temperature for 3 h. Free peptide was precipitated in cold ethyl ether and lyophilized. Crude peptide was purified by reversed phase HPLC, and each fraction was characterized by LC-MS analysis.

H-Cys-Ahoh-DPhe-Gln-Trp-Ala-Val-NMeGly-His-Sta-Leu-NH<sub>2</sub>; Cys-BN-AA1:  $R_t = 8.0$  min; MS (ESI<sup>+</sup>):  $m/z$  1565.8 calcd. for C<sub>74</sub>H<sub>116</sub>N<sub>16</sub>O<sub>19</sub>S<sub>4</sub>[M+2H]<sup>+</sup>/2 = 784.4 a.m.u.

#### Preparation of liposomal doxorubicin modified with BN-AA1 peptide

Preparation of liposomal Dox modified with Cys-BN-AA1 peptide (formulation identified as Doxil-BN-AA1) was obtained according a two-steps procedure by using a three-vials (vials A, B and C) kit: vial (A) is filled with a sterile, translucent, red liposomal dispersion of the doxorubicin drug (pegylated liposomal Dox, volume = 25.0 mL, Dox quantity 2.0 mg/mL, corresponding to 50.0 mg of drug). The pharmaceutical preparation containing fully hydrogenated soy phosphatidylcholine (HSPC), cholesterol and N-(carbonyl-methoxypolyethylene glycol 2000)-1,2-distearoyl-sn-glycero-3-phosphoethanolamine sodium salt (DSPE-Peg2000). Each mL also contained ammonium sulfate, approximately 0.6 mg; histidine as a buffer; hydrochloric acid and/or sodium hydroxide for pH control; and sucrose to maintain isotonicity. Vial (B) contained 32.3 mg of DSPE-Peg2000-maleimide (2% mol/mol ratio of the total phospholipids) in its lyophilized form. Vial (C) contained 17.2 mg of the Cys-BN-AA1 lyophilized peptide powder. Preparation of targeted Doxil-BN-AA1 was achieved by transferring the entire content of vial (A) into vial (B). The latter one is left to shake for 60 min at room temperature. The complete post-insertion of DSPE-Peg2000-maleimide in Doxil was confirmed by DLS measurements. In a second step, the content of vial B, obtained as above described, was transferred into the vial (C) containing 17.2 mg of the lyophilized peptide Cys-BN-AA1. The vial was placed on a shaker at room temperature and leaved to shake for 30 min.

#### Liposome characterization

The mean diameter of the final liposomes formulation was determined by dynamic light scattering (DLS) using a ZetasizerNano ZS (Malvern Instruments, Westborough, MA) equipped with a NIBS system (173° backscatter angle). Experimental settings for the determination of the mean diameter and polydispersity index were: measurement position (mm) 4.65; attenuator 8; temperature 25 °C; and cell, cuvette volume 1.0 mL. DLS measurements were carried out in triplicate on samples 100-fold diluted (concentration of  $2.0 \times 10^{-4}$  M). Eventually, impurities from the sample were physically removed before measurements by centrifuging the samples at room temperature at 13,000 rpm for 5 min.

#### Characterization of the final product

Here is reported a detailed description of the characterization achieved on the final formulation product, Doxil-BN-AA1, contained in vial (C) in terms of:

- (1) Physicochemical properties (size and polydispersity index)
- (2) Quantitatively occurrence of the coupling reaction between the peptide and the maleimido-function on the liposomal surface
- (3) Drug content of liposomes after derivatization

To verify point (1), 250  $\mu$ L from final solution in vial (C) was transferred to a clean Eppendorf and liposome size and polydispersity were measured by DLS.

To verify points (2) and (3), 250  $\mu$ L from the final solution in vial (C) was purified on gel filtration and the amount of free peptide and of Dox was determined by a deep analytical and spectroscopic characterization. Each characterization was carried out in triplicate starting from three different preparation lots. The free amount of Dox in vial (A) was estimated according to the same experimental procedure. Briefly, 250  $\mu$ L from the final solution in vial (C) was transferred to a clean Eppendorf and 150  $\mu$ L of water was added ( $V_{tot} = 400$   $\mu$ L). The solution was eluted on a Sephadex G50 column (GE Healthcare—Illustra Nick Column) with 800  $\mu$ L of water to obtain the liposomal fraction; the column was then eluted with additional 2.0 mL of water to collect the free fraction. Both Dox and peptide concentrations in this latter fraction were determined by UV–Vis on Thermo Fisher Scientific Inc. (Wilmington, DE, USA) Nanodrop 2000c spectrophotometer equipped with a 1.0-cm quartz cuvette (Hellma). Concentrations of peptide and of DOX were evaluated at a wavelength of 280 and 480 nm, respectively. The free peptide and DOX content were also estimated using an RP-HPLC calibration curve. RP-HPLC analyses were carried out on a column C18 (Jupiter, Phenomenoex, 150  $\times$  25 mm); eluents: H<sub>2</sub>O/0.1% TFA (A) and CH<sub>3</sub>CN/0.1% TFA (B); method from 5% (B) to 70% (B) in 10 min; and UV revelation at 210 nm. Tryptophan environment in the liposomal fraction was studied by fluorescence spectroscopy between 300 and 400 nm exciting the sample at 280 nm.

#### In vivo assays

Animal assays were carried out on 6-week-old female BALB/c nude mice (Harlan Nossan, Italy). Mice bearing xenografts of PC-3 cells were generated as previously described [41]. Briefly, 100  $\mu$ L of the cell suspensions at a density of  $2-3 \times 10^7$  mL<sup>-1</sup> in PBS with 0.1% glucose and mixed with an equal volume of Matrigel™ (BD Biosciences, Bedford) was injected subcutaneously into the flank of mice (weight 17–

23 g). All procedures were performed within a laminar airflow cabinet using aseptic technique. Tumor growth was measured each second day, starting 28 days following cell inoculation, using a caliper. Approximately 5 weeks after cell implantation, when tumors reached an average volume of 100–150 mm<sup>3</sup>, mice were randomly distributed into three groups ( $n = 12$ ) and intravenously (through the lateral tail vein) administered with a single dose of the following sterile formulations: saline buffer (CTRL), pegylated liposomal Dox modified with the bombesin peptide at 10 mg/kg dosage of Dox (Doxil-BN-AA1), and untargeted liposomal Dox at 10 mg/kg dosage of Dox (pegylated liposomal Dox). Drug dosage was adjusted with sterile PBS according to mean body weight for each group. Mice body weights were monitored twice a week following treatment. General animal health conditions were also evaluated to detect potential side effects, including food and water withdrawal, impaired movement, body weight loss, or behavioral changes. Procedures involving animals and their care were in conformity with institutional guidelines that comply with national and international laws and policies. MRI monitored tumor growth every 4 days for the following 36 days. The experiment was ended when tumors reached a volume close to 1500 mm<sup>3</sup> and before any sign of deteriorating health. Tumor growth curves, obtained by plotting tumor volume (mm<sup>3</sup>) versus day elapsed after treatment administration, were determined for the different experimental groups. MRI acquisitions were performed by using a Biospec tomograph (Bruker, Karlsruhe, Germany) equipped with a 4.7-T 33-cm bore horizontal magnet (Oxford, Oxford, UK). The mice were anesthetized by inhalation of a mixture of air and O<sub>2</sub> containing 0.5–1% isoflurane and were placed in a prone position inside a transmitter–receiver birdcage coil with an internal diameter of 3.5 cm. Images were acquired using transverse multislice, fast spin echo T<sub>2</sub>-weighted images (RARE, TE<sub>eff</sub> = 70 ms) for tumor localization and measurement of tumor volume. In some subjects ( $n = 6$  for each experimental group) and at three early time points (4, 8, 12 days after treatment), diffusion-weighted images (DWIs) were also acquired in order to detect early the therapeutic efficacy of the administered compounds [42]. DWIs were acquired using an EPI sequence with fat-suppression and with TR = 3000 ms, TE = 25.3 ms,  $b = 0$ ,  $b = 500$ , and  $b = 1000$  s/mm<sup>2</sup>, for a total acquisition time equal of 5 min and 24 s. The tumor volume and the mean apparent diffusion coefficient (ADC) values were obtained from images by using the software Paravision 5.1 (Bruker, Karlsruhe, Germany). A region-of-interest (ROI) was manually drawn on both T2w and DWI images in order to cover the whole tumor. The mean ADC value over the whole tumor was obtained by the weighted average of ADC values of different slice using the number of pixels of each slice as weight. Animal work was conducted following Italian law (D.L., March 4, 2014 no. 26) and the European Union normative (2010/63/EU). Major efforts were performed to minimize

the number of animals and to avoid their suffering. Statistical significant differences were analyzed group-wise at each time point with unpaired *t* test. The *p* values were corrected for multiple comparisons, and *p* values lower than 0.05 were accepted as significant.

## Results and discussion

### Rational for a kit development

Pegylated liposomal doxorubicin (PLD), commercially available as Doxil® (Caelyx® in Europe), is an example of successful formulation of liposomal drug for passive targeting of tumor cells. It was the first patented liposomal drug and the first nanomedicine reaching the clinic. The FDA approved it in 1995 for the following: (1) AIDS-related Kaposi's sarcoma (KS); (2) relapsed ovarian cancer, after platinum-based treatment; (3) metastatic breast cancer with cardiac risk; and (4) multiple myeloma in combination with Velcade. Active principle is doxorubicin, an antibiotic antineoplastic of anthracycline class, which works as DNA intercalating agent and as inhibitor of topoisomerase II. PLD formulation has much lower cardiotoxicity and most reduced side effects compared to conventional Dox. Indeed, the liposomal shell prevents its cardiotoxicity, while the presence of long PEG chains on the external liposomal surface helps in increasing circulation time of the entire vehicle. Overall, PLD improves patient compliance and quality of life. As the other clinically studied and approved liposomal drugs, it does not contain any targeting ligands and thus it reaches the tumor site by a passive targeting mechanism.

Several strategies for the preparation of peptide modified liposomal doxorubicin have been proposed until now [43]. Here we evaluated the possibility to prepare targeted PLD formulation by starting directly from the commercial untargeted one. This approach presents a series of advantages correlated to the product manufacture and to the drug efficacy and safety. Due to the small differences between the novel drug formulation and the approved one, the validation should occur quickly. The possibility to keep peptide derivative in its lyophilized form until to the *in vivo* administration preserves its chemical integrity without the introduction of novel excipients in the formulation. Moreover, the peptide sequence can be rationally tuned in agreement with the patient requirements, achieving an easy development of a personalized medicine. In our case, combining the post-insertion and the post-modification strategies, we achieved a direct PLD functionalization with BN-AA1 peptide sequence. The post-insertion strategy allows an easy and relatively fast introduction of functional group on the external surface of liposomes, whereas the post-modification strategy allows the selective coupling of a ligand on the liposome. Due to the large

accessibility of commercial phospholipids containing a maleimido-functional group (e.g., DSPE-Peg2000-maleimide, Fig. 2a), we bound the peptide, derivatized with a thiol group, using the Michael addition [43, 44].

Even if the method is applicable to some peptide sequence opportunistically modified, here we report results concerning PLD modification with a stable bombesin peptide analogue (Cys-BN-AA1; Fig. 2b). Following this idea, we developed a kit containing three vials: the first vial is filled with the commercially available pegylated liposomal Dox pharmaceutical preparation (Doxil); the second vial contains DSPE-Peg2000-maleimide phospholipid in its lyophilized form; and the third vial contains the targeting peptide modified with an appropriate reactive function in a 1:1 stoichiometric amount respect to the phospholipid and in its lyophilized form.

### Peptide identification and synthesis

The selected peptide, Cys-BN-AA1, reported in Fig. 2b, is a stable analogue of bombesin peptide displaying antagonist activity [42]. It is able to bind with high affinity and selectivity the bombesin receptors known as GRP-Receptors. The peptide sequence BN-AA1 (H-DPhe-Gln-Trp-Ala-Val-N(Me)Gly-His-Sta-Leu-NH<sub>2</sub>) has been selected from a side-by-side *in vitro* and *in vivo* comparison of eight different peptide sequences labeled with gamma emitting radioisotopes chelated by the macrocyclic DOTA (1,4,7,10-tetraazacyclododecane-1,4,7,10-tetraacetic acid) chelating agent [42]. Among all the screened compounds, this peptide labeled with <sup>111</sup>In shows very high *in vitro* affinity towards PC3 cells overexpressing GRP receptors (dissociation constant, K<sub>d</sub>, of 5.91 nM) and high serum stability (half-life of 414 h) [42]. Moreover, *in vivo* results on mice bearing subcutaneous PC-3 xenografts, overexpressing the GRP receptors,

clearly indicate a promising biodistribution profile with most of radioactivity concentrated on the tumor site and high *in vivo* tumor affinity.

BN-AA1 peptide was derivatized at the N-terminus with a cysteine (Cys) residue, since a thiol group (-SH) is required for the Michael addition on the liposomes, as shown in Fig. 3. According to the literature data, the C-terminal of the peptide is responsible for GRP receptor binding in this class of bombesin peptides; thus, our N-terminus modification should not affect the peptide binding capability [45]. In order to distance and better expose the bioactive sequence from the liposomal surface, a poly-oxoethylene linker Ahoh (-NH-(CH<sub>2</sub>CH<sub>2</sub>O)<sub>6</sub>-CH<sub>2</sub>CH<sub>2</sub>CO-) was introduced between the peptide and the cysteine residue. The full peptide derivative was synthesized in solid phase by using Rink-amide MBHA resin and Fmoc (fluorenylmethyloxycarbonyl protecting group) strategies. At the end of the synthesis, it was fully deprotected and cleaved from the solid support with TFA and scavenger solution. Crude peptide was precipitated in cold ethyl ether and lyophilized. Then, it was purified by reversed phase HPLC and each fraction was characterized by LC-MS analysis. The pure Cys-BN-AA1 peptide was recovered as lyophilized product in good yield (>47%) and with high HPLC purity (>97%).

### Product preparation and characterization

The procedure for preparation of Doxil-BN-AA1 is based on the use of a kit containing the three well-distinguished vials (Fig. 4). Vial (A) is the commercial PLD formulation (25 mL of liposomal Dox solution) at 2 mg/mL of Dox corresponding to 50 mg of Dox; vial (B) contains 32.3 mg of the maleimido-derivative of DSPE-Peg2000 phospholipid (DSPE-Peg2000-maleimide), corresponding to 2% mol/mol of the total lipids present in the liposomal Dox. Finally, vial (C) contains

**Fig. 2** Chemical structures of **a** DSPE-Peg2000-maleimide and **b** Cys-BN-AA1 peptide derivative. The commercial phospholipid DSPE-Peg2000-maleimide has the same hydrophobic moiety of HSPC lipid contained in Doxil, a polyethylene (glycole) spacer, and the maleimido reactive function. Cys-BN-AA1 peptide was synthesized according to the SPPS protocols using the tBu/Fmoc strategy. For the peptide sequence, a three-letter code is used for amino acid. -Ahoh- is the acronym for a PEG fragment with formula: -NH-(CH<sub>2</sub>CH<sub>2</sub>O)<sub>6</sub>-CH<sub>2</sub>CH<sub>2</sub>CO

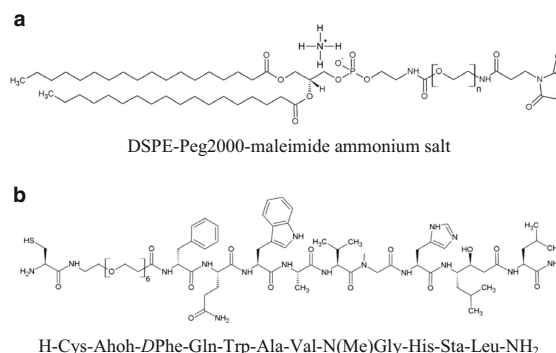
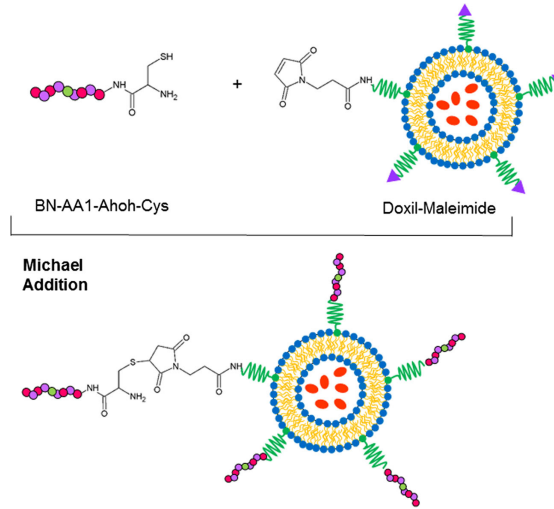


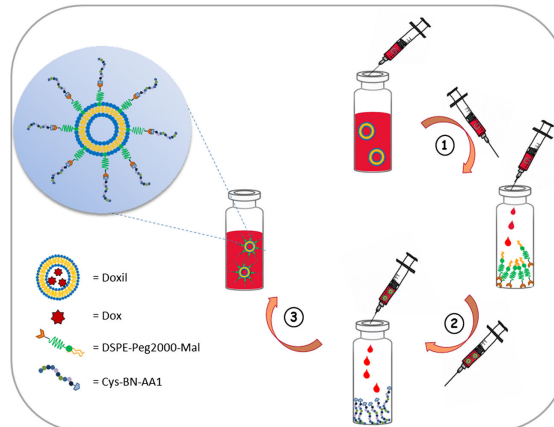
**Fig. 3** Schematic representation of liposome surface functionalization with Cys-BN-AA1 peptide via Michael addition in the last derivatization step. The reaction was conducted at room temperature under shaking of 30 min. Cysteine acts as Michael donor meanwhile maleimide serves as acceptor



17.2 mg of the lyophilized bombesin peptide, BN-AA1, derivatized at the N-terminus with a Cys residue (Cys-BN-AA1). This quantity of peptide corresponds to stoichiometric amount respect to DSPE-Peg2000-maleimide (1/1 mol/mol). Targeted liposomal Dox was obtained towards two steps. In the first step, it was achieved the post-insertion of DSPE-Peg2000-maleimide in pegylated liposomal Dox bilayer, whereas in the second, one liposomal surface was

functionalized with a modified analogue of the BN-AA1 peptide. The post insertion of DSPE-Peg2000-maleimide in the pegylated liposomal Dox was achieved by transferring the entire content of vial (A) into vial (B) and by leaving it to shake for 60 min at room temperature. The post-insertion was monitored by dynamic light scattering (DLS). After 60 min, the classical distribution mode around 17–20 nm, expected for of DSPE-Peg2000-maleimide pure micelles, is

**Fig. 4** Kit for preparation of peptide derivative liposomal doxorubicin. Step 1: quantitative transfer of PLD in vial B containing DSPE-Peg2000-maleimide. Step 2: transfer of maleimido derivatized liposomes in vial C containing lyophilized Cys-BN-AA1 peptide. Step 3: obtaining of targeted liposomal formulation



completely absent and DLS profile of liposomes in Fig. 5 shows a monomodal distribution centered at 95 nm. This result suggests the complete insertion of DSPE-Peg2000-maleimide in the liposomal doxorubicin suspension.

In the second step, the content of vial (B), obtained as above described, is transferred into vial (C) containing 17.2 mg of Cys-BN-AA1 peptide and the vial sheered at room temperature for 30 min. During the reaction time, a complete quantitative reaction occurs between the maleimido function on the liposomal surface and the cysteine sulfhydryl function at the N-terminus of the peptide derivative (see Fig. 3). This result was confirmed from the spectroscopical and chromatographic characterization performed on the final product after gel filtration. Both analytical methods clearly indicate the absence of free peptide in solution;  $Abs_{280}$  (for Trp) is absent or close to zero ( $<0.016$  that represents the value as upper limit to indicate peptide presence at the analytical experimental conditions we used), while RP-HPLC profile shows any peak at the peptide elution time (around 8 min at the reported RP-HPLC analytical conditions).

In order to obtain additional information on the peptide location, liposomal sample was also studied by fluorescence. By exciting the sample at 280 nm, which corresponds to the excitation wavelength of the Trp residue, it is possible to detect an emission peak around 350 nm, typically observed for tryptophan residue surrounded in a water environment (see Fig. 6) [46]. This result indicates that BN-AA1 peptide, covalently bound to the liposome, is well exposed on external liposomal surface with the active region prone to bind the target receptors. As expected, mean diameter and polydispersity index (PDI) of the targeted liposomal formulation Doxil-BN-AA1 are not significantly different with respect to pegylated liposomal Dox before and after post-insertion of

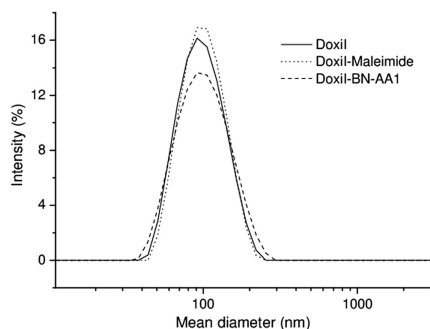


**Fig. 5** DLS intensity profiles of: (a) liposomes present in commercial preparation of Doxil; (b) liposomes after post insertion of DSPE-Peg2000-maleimide according to preparation procedure step 1 and (c) liposomes derivatized with BNAA-1 peptide sequence in the final preparation

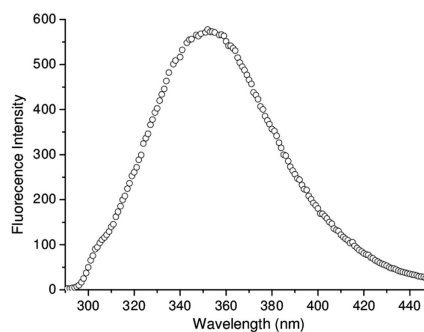


**Fig. 6** Fluorescence spectrum of the liposomal fraction measured by exciting at 280 nm (excitation for the tryptophan residue) and registering fluorescence emission in the 300–400 nm range

DSPE-Peg2000-maleimide. DLS profiles for the three liposomal formulations are reported in Fig. 5 and data summarized in Table 1. In all cases, liposome diameter is around  $95 \pm 35$  nm with a polydispersity index of  $0.20 \pm 0.10$ , thus confirming that both the insertion of DSPE-Peg2000 at very low percentage (2% mol/mol) and the peptide labelling do not modify the structural properties of the aggregates. Finally, we demonstrated by HPLC chromatography that manipulation of the commercial PLD, due to the post-insertion and to the post-derivatization of liposomal surface with peptide ligand, does not alter the amount of free Dox present in the original formulation. Both commercial PLD and targeted liposomes Doxil-BN-AA1 were purified by gel-filtration and free Dox removed quantified from the comparison of the areas of the HPLC peaks (data not shown).

All these data clearly indicate that by following the preparation procedure based on the three vials kit here reported, it is possible to efficiently prepare peptide modified liposomal doxorubicin with liposome properties and Dox content equal to that contained in the approved and commercially available PLD. Moreover, it appears clear that there is any free peptide in solution and all peptide is linked on the liposome external surface with the active region ready to bind the targeting receptors.

As deductible from the comparison of this study with our previous ones [9, 41, 47], the development a kit permits to overcome several problematic issue related to the regulatory needs, industrial preparation and storage of targeted liposomal Dox. Indeed, we previously prepared different BN-liposomal doxorubicin formulations using the pre-formulation method. According to this strategy, we synthesized very complex amphiphilic peptides (having as acronym MonY-BN) containing a bombesin active sequence derivatized with a chelator and with a hydrophobic portions composed of two C18 hydrocarbon chains. The high complexity of synthetic monomers, like

**Table 1** Structural parameters (hydrodynamic diameters, polydispersity indexes, PDI, and diffusion coefficients,  $D$ ) from dynamic light scattering measurements of Doxil before and after DSPE-Peg2000-maleimide post-insertion and after derivatization of the surface with Cys-BN-AA1 peptide

Liposomal systems	Diameter (nm) $\pm$ S.D.	PDI	$D$ ( $\text{m}^2 \text{s}^{-1}$ ) $\times 10^{-12}$
Pegylated liposomal Dox	91.7 $\pm$ 34.6	0.105	5.4 $\pm$ 2.0
Doxil-maleimide	94.6 $\pm$ 32.7	0.083	5.2 $\pm$ 1.8
Doxil-BN-AA1	97.8 $\pm$ 41.0	0.211	5.0 $\pm$ 2.1

monY-BN, and the low stability of the peptide sequences upon the time at physiological pH strongly limit the industrial development of novel targeted drugs.

### In vivo assays

Modifying the passive targeting mechanism adopted by PLD with an active targeting, mediated by a high affinity interaction of the peptide-receptor couple, a higher therapeutic profile of the drug is expected.

We have performed a preliminary in vivo experiment to study the efficacy of the liposomal Dox on tumor growth by comparing the effect of pegylated liposomal Dox with Doxil-BN-AA1 preparation, containing peptide sequence on external surface of liposomes. Figure 7a shows representative images of

mice belonging to Doxil-BN-AA1, Doxil and control (CTRL) groups acquired 32 days after treatment. These images qualitatively show that the treated tumors are smaller than untreated one and that Doxil-BN-AA1 is more effective than Doxil. Figure 7b shows the time dependence of the average tumor volume in the three groups. From 20 days after the treatment onward, both Doxil-BN-AA1 and pegylated liposomal Dox treated groups differ significantly from the CTRL group. Moreover, 32 and 36 days after the treatment, the Doxil-BN-AA1 group showed significantly smaller average tumor volume than the pegylated liposomal Dox group. Results obtained by using DWI are reported in Fig. 7c and confirm the better therapeutic profile of Doxil-BN-AA1: the average apparent diffusion coefficient (ADC) in Doxil-BN-AA1 group is significantly higher than in pegylated liposomal Dox group ( $p < 0.05$ ) and

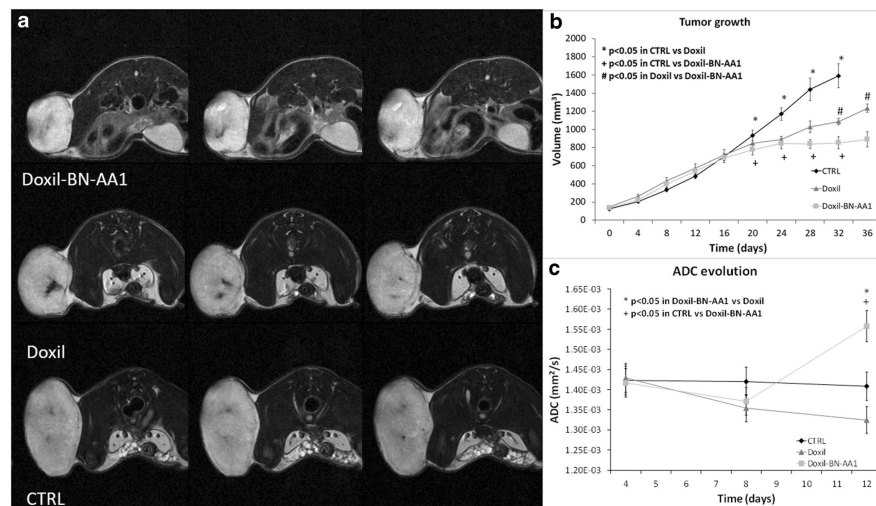


**Fig. 7** **a** Representative images of mice belonging the Doxil-BN-AA1 (upper line), Doxil (middle line), and CTRL (lower line) groups acquired 32 days after treatment. The three central slices of each tumor are reported. **b** Tumor volumes obtained by MRI for CTRL-, Doxil-, and Doxil-BN-AA1-treated mice. Mean values  $\pm$  SEM are reported. Tumor volumes in the Doxil-BN-AA1 group are significantly smaller than in the Doxil

group 32 and 36 days after the treatment. **c** Average ADC of tumors for CTRL-, Doxil-, and Doxil-BN-AA1-treated mice. Mean values  $\pm$  SEM are reported. Twelve days after drug administration, the ADC of tumors in Doxil-BN-AA1-treated mice is significantly higher than in either Doxil or CTRL group

significantly higher than in CRTL group, at 12 days after treatment. The pegylated liposomal Dox group was not statistically different from CRT. Interestingly enough, no difference is detectable in the tumor volume at this point. DW-MRI is highly sensitive to microenvironmental alterations at the cellular level and has been extensively evaluated for the generation of quantitative and early imaging biomarkers of therapeutic response in tumors. In this paper, we have applied DWI to obtain the value of the average ADC. According to literature, as cellular density decreases, water mobility increases and such an increase is reflected in higher values of ADC. We found a small but statistically significant increase in ADC of tumors treated with Doxil-BN-AA1 compared to both PLD and CRTL groups, 12 days after treatment that can be interpreted as a more pronounced cellular necrosis at the microscopic level [48]. It is noteworthy that such effect was measured well below any effect on tumor volume could be detected. A limitation of our *in vivo* results is the absence of *ex vivo* immunohistochemistry assessment of possible alterations in apoptosis or proliferation markers. A further limitation is in the experimental plan adopted envisaging a single treatment and a very long follow-up of 32/36 days. A different experimental plan with repeated treatments will probably produce a more pronounced decrease of the tumor volume in the group treated with Doxil-BN-AA1. The investigation of different administration regimen and dosages, as well as an immunohistochemical elucidation of the mechanism of action of the targeted drug, will be the objective of future studies. Although preliminary, *in vivo* experiments show that PLD modified with an active targeting is more effective than plain pegylated liposomal Dox since it slows down tumor growth, with statistically significant difference detectable at long time interval after treatment. In addition, we observed targeted liposomes induce higher cellular necrosis, as detected by ADC, at an early time point. We expect that a different dosing regimen with repeated administrations along the time course of tumor growth will greatly increase the efficacy of the proposed treatment. These results confirm that ADC measurement is a valuable and sensitive biomarker of the early efficacy of antitumor treatments for cytotoxic drugs similarly to other “functional” biomarkers used for antiangiogenic drugs [49–51].

## Conclusion

Development of peptide-targeted liposomes represents a great advance in the use of liposomal drugs for cancer therapy. Several studies, both *in vitro* and *in vivo* from many laboratories worldwide, confirm the efficacy of this approach [3, 13]. Many efforts in the fight against cancer have been devoted in the individuation of the best receptor/peptide couple, in the liposome design, and in the industrial development. However, many critical issues are still unsolved. Mainly, the scaling up of promising

compounds prepared at the lab scale limited their industrial development. This is particularly true for *de novo* preparation of peptide targeted liposomal drugs that needs highly pure peptide derivatives and the use expensive products good manufacturing protocol (GMP). Moreover, the peptide labeled liposomal drugs could be affected by short peptide shelf life in buffered solution at physiological pH. The limited stability of peptides in solution represents a severe limitation in the development of formulation having a long expiration date. As an alternative, more sophisticated preservation procedures such as lyophilizing steps and drug loading only on the reconstituted compound have been required.

We reported on a new method for an easy preparation of peptide targeted liposomal doxorubicin based on direct modification of the commercial liposomal drug pegylated liposomal Dox. The method uses a three vials kit and uses a two steps procedure that could be easily performed by clinicians directly before patient administration of the liposomal drug. Analytical data confirm the requested specifics for the final product such as (1) the absence of free peptide in solution, (2) the properties (shape and size) of the peptide modified liposomes similar to that of pegylated liposomal Dox liposomes, and (3) the Dox content of the liposomes in line with the amount of Dox loaded in pegylated liposomal Dox. We tested our method for label pegylated liposomal Dox liposomes with a bombesin analogue peptide for the development of targeted liposomal doxorubicin, Doxil-BN-AA1, to be used in GRP overexpressing tumors such as ovarian and breast cancers. Preliminary animal studies confirmed that in mice treated with targeted liposomal drug, prepared according the developed method, tumor growth is low, with an improved efficacy of the product respect to mice treated with non-modified pegylated liposomal Dox or with saline solution. However, more animal studies should be performed by using a procedure based on several treatments in the time, as it happens in women suffering of ovarian cancer treated with PLD formulations.

**Funding information** This research was funded by Italian Ministry for Research (M.I.U.R.), 0016/09 593/2000 (Invectors) and FIRB “RINAME” RBAP114AMK projects.

## Compliance with ethical standards

**Conflict of interest** A. Accardo and G. Morelli participate in a spin-off company (Invectors, srl) devoted to the development of targeted liposomal compounds for cancer therapy. The other authors report no conflicts of interest in this work.

**Publisher's Note** Springer Nature remains neutral with regard to jurisdictional claims in published maps and institutional affiliations.

## References

1. Maruccci F, Lefoulon F. Active targeting with particulate drug carriers in tumor therapy: fundamentals and recent progress. *Drug Discov Today*. 2004;9(5):219–28.

2. Pattni BS, Chupin VV, Torchilin VP. New developments in liposomal drug delivery. *Chem Rev*. 2015;115(19):10938–66.
3. Accardo A, Morelli G. Review peptide-targeted liposomes for selective drug delivery: advantages and problematic issues. *Biopolymers*. 2015;104(5):462–79.
4. Vijaykumar N, Sandeep K. Recent advances in liposomal drug delivery: a review. *Pharmaceutical Nanotechnology*. 2015;3(1):35–55.
5. Bozzuto G, Molinari A. Liposomes as nanomedical devices. *Int J Nanomedicine*. 2015;10:975–99.
6. Kuang H, Ku SH, Kokkole E. The design of peptide-amphiphiles as functional ligands for liposomal anticancer drug and gene delivery. *Adv Drug Delivery Rev*. 2017;110, 111 80–101.
7. Narayanaswamy R, Wang T, Torchilin VP. Improving peptide applications using nanotechnology. *Curr Top Med Chem*. 2016;16(3):253–70.
8. de Smet M, Langereis S, van den Bosch S, Bitter K, Hijnen NM, Heijman E, et al. SPECT/CT imaging of temperature-sensitive liposomes for MR-image guided drug delivery with high intensity focused ultrasound. *J Control Release*. 2013;169(1–2):82–90.
9. Accardo A, Mansi R, Morisco A, Mangiapia G, Paduano L, Tesaro D, et al. Peptide modified nanocarriers for selective targeting of bombesin receptors. *Mol BioSyst*. 2010;6(5):878–87.
10. Gabizon A, Catane R, Uziely B, Kaufman B, Safra T, Cohen R, et al. Prolonged circulation time and enhanced accumulation in malignant exudates of doxorubicin encapsulated in poly-ethylene-glycol coated liposomes. *Cancer Res*. 1994;54:987–92.
11. Gaber MH, Wu NZ, Hong K, Huang SK, Dewhirst MW, Papahadjopoulos D. Thermosensitive liposomes: extravasation and release of contents in tumor microvascular networks. *Int J Radiat Oncol Biol Phys*. 1996;36:1177–87.
12. Matsumura Y, Maeda H. A new concept for macromolecular therapeutics in cancer chemotherapy: mechanism of tumorotropic accumulation of proteins and the antitumor agent smancs. *Cancer Res*. 1986;46:6387–92.
13. Accardo A, Aloj L, Aurilio M, et al. Receptor binding peptides for target-selective delivery of nanoparticles encapsulated drugs. *Int J Nanomedicine*. 2014;27(9):1537–57.
14. Yu MK, Park J, Jon S. Targeting strategies for multifunctional nanoparticles in cancer imaging and therapy. *Theranostic*. 2012;2:3–44.
15. Ahn J, Miura Y, Yamada N, Chida T, Liu X, Kim A, et al. Antibody fragment-conjugated polymeric micelles incorporating platinum drugs for targeted therapy of pancreatic cancer. *Biomaterials*. 2015;39:23–30.
16. Liu M, Li W, Larregieu CA, Cheng M, Yan B, Chu T, et al. Development of synthetic peptide-modified liposomes with LDL receptor targeting capacity and improved anticancer activity. *Mol Pharm*. 2014;11(7):2305–12.
17. Ringhieri P, Iannitti R, Nardon C, Palumbo R, Fregona D, Morelli G, et al. Target selective micelles for bombesin receptors incorporating Au(III)-dithiocarbamate complexes. *Int J Pharm*. 2014;473:194–202.
18. Zong T, Mei L, Gao H, Shi K, Chen J, Wang Y, et al. Enhanced glioma targeting and penetration by dual-targeting liposome co-modified with T7 and TAT. *J Pharm Sci*. 2014;103(12):3891–901.
19. Apte A, Koren E, Koshkaryev A, Torchilin VP. Doxorubicin in TAT peptide-modified multifunctional immunoliposomes demonstrates increased activity against both drug-sensitive and drug-resistant ovarian cancer models. *Cancer Biol Ther*. 2014;15(1):69–80.
20. Nahar K, Absar S, Gupta N, Kotamraju VR, McMurtry IF, Oka M, et al. Peptide-coated liposomal fasudil enhances site specific vasodilation in pulmonary arterial hypertension. *Mol Pharm*. 2014;11(12):4374–84.
21. Wang F, Chen L, Zhang R, Chen Z, Zhu L. RGD peptide conjugated liposomal drug delivery system for enhance therapeutic efficacy in treating bone metastasis from prostate cancer. *J Control Release*. 2014;196:222–33.
22. Liu Y, Ran R, Chen J, Kuang Q, Tang J, Mei L, et al. Paclitaxel loaded liposomes decorated with a multifunctional tandem peptide for glioma targeting. *Biomaterials*. 2014;35(17):4835–47.
23. Ringhieri P, Mannucci S, Conti G, Nicolato E, Fracasso G, Marzola P, et al. Liposomes derivatized with multimeric copies of KCCYSL peptide as targeting agents for HER-2-overexpressing tumor cells. *Int J Nanomedicine*. 2017;12:501–14.
24. Song S, Liu D, Peng J, Sun Y, Li Z, Gu JR, et al. Peptide ligand-mediated liposome distribution and targeting to EGFR expressing tumor in vivo. *Int J Pharm*. 2008;363:155–61.
25. Wickremasinghe NC, Kumar VA, Hartgerink JD. Two-step self-assembly of liposome-multidomain peptide nanofiber hydrogel for time-controlled release. *Biomacromolecules*. 2014;15:3587–95.
26. Pradhan TK, Katsuno T, Taylor JE, Kim SH, Ryan RR, Mantey SA, et al. Identification of a unique ligand which has high affinity for all four bombesin receptor subtypes. *Eur J Pharmacol*. 1998;343(2–3):275–87.
27. Kahkonen E, Jambor I, Kempainen J, Lehtio K, Gronroos TJ, Kuisma A, et al. In vivo imaging of prostate cancer using [68Ga]-labeled bombesin analog BAY86-7548. *Clin Cancer Res*. 2013;19(19):5434–43.
28. Wieser G, Mansi R, Grosu AL, Schultze-Seemann W, Dumont-Walter RA, Meyer PT, et al. Positron emission tomography (PET) imaging of prostate cancer with a gastrin releasing peptide receptor antagonist—from mice to men. *Theranostics*. 2014;4(4):412–9.
29. Majumdar ID, Weber HC. Biology of mammalian bombesin-like peptides and their receptors. *Curr Opin Endocrinol Diabetes Obes*. 2011;18(1):68–74.
30. Reubi JC. Somatostatin and other peptide receptors as tools for tumor diagnosis and treatment. *Neuroendocrinology*. 2004;80(Suppl 1):51–6.
31. Fleischman A, Waser B, Reubi JC. High expression of gastrin-releasing peptide receptors in the vascular bed of urinary tract cancers: promising candidates for vascular targeting applications. *End Rel Canc*. 2009;16:623–33.
32. Fang MZ, Liu C, Song Y, Yang GY, Nie Y, Liao J, et al. Overexpression of gastrin-releasing peptide in human esophageal squamous cell carcinomas. *Carcinogenesis*. 2004;25(6):865–71.
33. Kömer M, Waser B, Rehm R, Reubi JC. Early over-expression of GRP receptors in prostatic carcinogenesis. *Prostate*. 2014;74(2):217–24.
34. Reile H, Armatis PE, Schally AV. Characterization of high-affinity receptors for bombesin/gastrin releasing peptide on the human prostate cancer cell lines PC-3 and DU-145: internalization of receptor bound <sup>125</sup>I-(Tyr4) bombesin by tumor cells. *Prostate*. 1994;25:29–38.
35. Markwalder R, Reubi JC. Gastrin-releasing peptide receptors in the human prostate: relation to neoplastic transformation. *Cancer Res*. 1999;59:1152–9.
36. Fleischman A, Waser B, Reubi JC. Overexpression of gastrin-releasing peptide receptors in tumor-associated blood vessels of human ovarian neoplasms. *Cel. Oncology*. 2007;29(5):421–33.
37. Morgat C, MacGrogan G, Brouste V, Vélasco V, Sévenet N, Bonnefoi H, et al. Expression of gastrin-releasing peptide receptor (GRPR) in breast cancer and its association with pathological, biological and clinical parameters: a study of 1432 primary tumors. *J Nucl Med*. 2017;58:1401–7.
38. Gugger M, Reubi JC. GRP receptors in non-neoplastic and neoplastic human breast. *Am J Pathol*. 2000;155:2067–76.
39. Chao C, Kirk I, Hellmich HL. Gastrin-releasing peptide receptor in breast cancer mediates cellular migration and interleukin-8 expression. *J Surg Res*. 2009;156:26–31.
40. Chang WC, White PD. Fmoc solid phase peptide synthesis. New York: Oxford University Press; 2000.

41. Accardo A, Salsano G, Morisco M, et al. Peptide-modified liposomes for selective targeting of bombesin receptors overexpressed by cancer cells: a potential theranostic agent. *Int J Nanomedicine*. 2012;7:2007–17.
42. Accardo A, Galli F, Mansi R, et al. Pre-clinical evaluation of DOTA coupled bombesin receptor ligands for imaging and therapy of gastrin releasing peptide receptor (GRP-R) expressing tumors. *Eur J Nucl Med Mol Imaging*. 2016;6:1–10.
43. Feldborg LN, Jølcck RI, Andresen TL. Quantitative evaluation of bioorthogonal chemistries for surface functionalization of nanoparticles. *Bioconjug Chem*. 2012;23(12):2444–50.
44. Accardo A, Del Zoppo L, Morelli G, et al. Liposome antibody–ionophore conjugate antiproliferative activity increases by cellular metallosis alteration. *Med Chem Commun*. 2016;7:2364–7.
45. Smith CJ, Volkert WA, Hoffman TJ. Radiolabeled peptide conjugates for targeting of the bombesin receptor superfamily subtypes. *Nucl Med Biol*. 2005;32:733–40.
46. Hixon JH, Reshetnyak YK. Algorithms for the analysis of tryptophan fluorescence spectra and their correlation with protein structural parameters. *Algorithms*. 2009;2:1155–75.
47. Accardo A, Mansi R, Salsano G, et al. Bombesin peptide antagonist for target-selective delivery of liposomal doxorubicin on cancer cells. *J Drug Target*. 2013;21(3):240–9.
48. Galbàn CJ, Hoff BA, Chenevert TL, et al. Diffusion MRI in early cancer therapeutic response assessment. *NMR Biomed*. 2017;30:3458.
49. Marzola P, Degrassi A, Calderan L, Farace P, Nicolato E, Crescimanno C, et al. Early antiangiogenic activity of SU11248 evaluated in vivo by dynamic contrast-enhanced magnetic resonance imaging in an experimental model of colon carcinoma. *Clin Cancer Res*. 2005;11(16):5827–32.
50. Marzola P, Degrassi A, Calderan L, Farace P, Crescimanno C, Nicolato E, et al. In vivo assessment of antiangiogenic activity of SU6668 in an experimental colon carcinoma model. *Clin Cancer Res*. 2004;10(2):739–50.
51. Marzola P, Ramponi S, Nicolato E, Lovati E, Sandri M, Calderan L, et al. Effect of tamoxifen in an experimental model of breast tumor studied by dynamic contrast-enhanced magnetic resonance imaging and different contrast agents. *Investig Radiol*. 2005;40(7):421–9.

*M. Costanzo, F. Vurro, B. Cisterna, F. Boschi, A. Marengo, E. Montanari, C. Di Meo, P. Matricardi, G. Berlier, B. Stella, S. Arpicco, M. Malatesta(2019). Uptake and intracellular fate of biocompatible nanocarriers in cycling and noncycling cells, Nanomedicine, 14(3):301-316. DOI: 10.2217/nmm-2018-0148.*



## Uptake and intracellular fate of biocompatible nanocarriers in cycling and noncycling cells

Manuela Costanzo<sup>\*1</sup>, Federica Vurro<sup>1</sup>, Barbara Cisterna<sup>1</sup>, Federico Boschi<sup>2</sup>, Alessandro Marengo<sup>3</sup>, Elita Montanari<sup>4</sup>, Chiara Di Meo<sup>4</sup>, Pietro Matricardi<sup>4</sup>, Gloria Berlier<sup>5</sup>, Barbara Stella<sup>3</sup>, Silvia Arpicco<sup>3</sup> & Manuela Malatesta<sup>1</sup>

<sup>1</sup>Department of Neurosciences, Biomedicine & Movement Sciences, University of Verona, Strada Le Grazie, 8 – 37134 Verona, Italy

<sup>2</sup>Department of Computer Science, University of Verona, Strada Le Grazie, 15 – 37134 Verona, Italy

<sup>3</sup>Department of Drug Science & Technology, University of Turin, Via P. Giuria, 9 – 10125 Torino, Italy

<sup>4</sup>Department of Drug Chemistry & Technologies, Sapienza University of Rome, Piazzale Aldo Moro, 5 – 00185 Roma, Italy

<sup>5</sup>Department of Chemistry & NIS Centre, University of Turin, Via P. Giuria, 7 – 10125 Torino, Italy

\*Author for correspondence: Tel.: +39 45 8027 272; [manuela.costanzo@univr.it](mailto:manuela.costanzo@univr.it)

**Aim:** To elucidate whether different cytokinetic features (i.e., presence or absence of mitotic activity) may influence cell uptake and distribution of nanocarriers, *in vitro* tests on liposomes, mesoporous silica nanoparticles, poly(lactide-co-glycolide) nanoparticles and nanohydrogels were carried out on C2C12 murine muscle cells either able to proliferate as myoblasts (cycling cells) or terminally differentiate into myotubes (noncycling cells). **Materials & methods:** Cell uptake and intracellular fate of liposomes, mesoporous silica nanoparticles, poly(lactide-co-glycolide) nanoparticles and nanohydrogels were investigated by confocal fluorescence microscopy and transmission electron microscopy. **Results:** Nanocarrier internalization and distribution were similar in myoblasts and myotubes; however, myotubes demonstrated a lower uptake capability. **Conclusion:** All nanocarriers proved to be suitably biocompatible for both myoblasts and myotubes. The lower uptake capability of myotubes is probably due to different plasma membrane composition related to the differentiation process.

First draft submitted: 27 April 2018; Accepted for publication: 13 November 2018; Published online: 22 January 2019

**Keywords:** microscopy • muscle cells • nanocarriers

Nanocarriers possess enormous potential as drug-delivery systems for controlled and targeted drug release, and a wide range of nanosystems have been reported for the treatment of various diseases and disorders [1]. Nanocarriers are able to protect the encapsulated agents from enzymatic degradation and to allow drug delivery and sustained release inside the cells; thus, they represent a promising approach to improve the administration of therapeutic agents while decreasing adverse systemic side effects. To carry out their therapeutic action without damaging patient's organism, nanocarriers should be biocompatible and biodegradable. In recent years, liposomes, mesoporous silica nanoparticles (MSN), polymeric nanoparticles (NPs) and nanohydrogels (NHs) have received great attention as biocompatible and versatile systems to encapsulate active agents.

Liposomes are attractive drug-delivery vehicles by their composition, which makes them biocompatible and biodegradable. They consist of an aqueous core entrapped by one or more bilayers of natural or synthetic phospholipids, and they are biologically inert, weakly immunogenic and intrinsically low toxic. Furthermore, drugs with different physicochemical characteristics can be encapsulated into liposomes: lipophilic drugs are entrapped in the lipid bilayer, hydrophilic drugs exclusively locate in the aqueous compartment and the amphiphilic ones are encapsulated in both the bilayer and the aqueous core [2,3].

Silica is generally recognized as safe by the US FDA and is used as an excipient in tablet-form drug formulations. The MSN have recently attracted attention as promising components of multimodal NP systems, owing to their straightforward synthesis and functionalization, ordered mesoporous structure with tunable pore size, large surface

and pore volumes resulting in high drug-loading capacity, good chemical stability and adequate biocompatibility [4–6]. The MSN (especially the amino-MSN) can be used to deliver small molecules or oligonucleotides and surface-tailored with various functional groups to increase biocompatibility, delivery capability and targeting [7–9].

Polymeric NPs are solid structures prepared from natural or synthetic polymers, where drugs can be adsorbed, dissolved, entrapped or encapsulated. They have good encapsulation efficiency and high stability in plasma, and increase the solubility and stability of hydrophobic drugs while lowering their toxicity, thus permitting a controlled release at target sites at relatively low doses [10–13]. In particular, the safe, biocompatible and commercially available poly(lactide-co-glycolide) (PLGA) is one of the most successfully used biodegradable polymers; its hydrolysis leads to metabolite monomers, lactic acid and glycolic acid, which are endogenous and easily metabolized *via* the Krebs cycle, thus having minimal systemic toxicity. Notably, PLGA is approved by US FDA and EMA for various drug-delivery systems for humans [14,15].

The NHs are nanosized 3D networks able to absorb large water amounts [16,17]. The NHs are usually soft, hydrophilic, biocompatible being a highly versatile nanosystem for delivering bioactive molecules (e.g., hydrophobic [18] and hydrophilic drugs [19], polypeptides [20] and genetic material [21]). Indeed, the porosity of NH networks provides a loading-reservoir for molecular and macromolecular therapeutics while protecting them from environmental degradation. The NHs can be prepared from natural [22] and/or synthetic [23] polymers and, based on the bonds in the polymer network, they are subdivided according to either physical [24] or chemical [25,26] cross-linking. A peculiarity of NHs is their swelling/deswelling properties in aqueous media; control over the swelling of the polymer network is useful for the controlled release of bioactive compounds. Moreover, being highly solvated, NHs display both liquid- and solid-like behavior: usually, these viscoelastic properties allow NHs to deform in the presence of a flow, enabling them to more easily travel through the extracellular matrix, thus enhancing permeation, binding and retention within tissues.

The cytotoxicity of these different nanocarriers has previously been tested *in vitro* using established cancer cell lines [2,27–30]. However, nanocarrier effects may depend on the metabolic activity and doubling time of the cells [31]; this suggests that the proliferation characteristics should be considered when testing the biocompatibility of nanosystems for systemic administration, since organisms are made of tissues and cells with peculiar kinetic and metabolic features. In particular, some tissues – such as the skeletal muscle – are mainly composed of terminally differentiated cells that have lost the ability to undergo mitotic divisions, but also contain stem cells (called satellite cells in the skeletal muscle), which are still able to divide under appropriate stimuli.

The aim of this study was therefore to elucidate whether different cytokinetic features (i.e., presence or absence of mitotic activity) may influence cell internalization of different nanocarriers previously demonstrated to be biocompatible to cultured cells. To do this, the uptake and intracellular fate of liposomes, MSN, PLGA NPs and NHs have been investigated by confocal fluorescence microscopy (CFM) and transmission electron microscopy (TEM) in C2C12 cells under cycling and noncycling conditions. The C2C12 are immortalized murine myoblast cells, which rapidly proliferate as myoblasts and efficiently fuse and terminally differentiate into myotubes, thus losing mitotic activity [32]. The C2C12 cells, therefore, represent a suitable system *in vitro* for studying cell-nanocarrier interactions in cycling (myoblasts) and terminally differentiated noncycling cells (myotubes).

## Materials & methods

### Nanocarriers

Liposomes were prepared by thin lipid film hydration and extrusion method. A chloroform solution of the lipid components (Avanti Polar-Lipids) 1,2-dipalmitoyl-*sn*-glycero-3-phosphocholine, cholesterol and L- $\alpha$  phosphatidyl-DL-glycerol sodium salt (70:30:3 molar ratios) was evaporated, and the resulting lipid film dried under vacuum overnight. Lipid films were hydrated with HEPES (4-[2-hydroxyethyl] piperazine-1-ethanesulfonic acid) buffer (pH 7.4), and the suspension was vortexed for 10 min and bath sonicated. The formulations were extruded (Extruder, Lipex) at 60°C passing the suspension ten-times under nitrogen through a 400 and 200 nm polycarbonate membrane (Costar, Corning Incorporated). Fluorescently labeled liposomes (Fluo-Lipo) were prepared as described above using a 10 mM solution of fluorescein-5-(and-6)-sulfonic acid trisodium salt (Invitrogen, Life Technologies) in HEPES buffer during hydration. Liposomes were purified through chromatography on Sepharose CL-4B columns, eluting with HEPES buffer at room temperature (RT).

Amino-mesoporous silica NPs (NH<sub>2</sub>-MSN) were prepared as previously described [6]. Fluorescein isothiocyanate (FITC) labeled MSN (Fluo-MSN) were prepared as previously reported [33] with minor modifications. Briefly, 250  $\mu$ l of FITC ethanol solution (0.3 mg/ml) were added to 1 mg of NH<sub>2</sub>-MSN in 150  $\mu$ l of MilliQ® water. The

mixture was maintained for 5 h under stirring in the dark, and then the NPs were centrifuged and washed with ethanol until the supernatants were colorless.

For the preparation of PLGA (50:50 or 75:25; Sigma) NPs, the nanoprecipitation technique was employed [34]. For each preparation, 12 mg of PLGA 50:50 or 75:25 were dissolved in 2 ml of acetone. This solution was poured into 4 ml of MilliQ® water under magnetic stirring; precipitation of particles spontaneously occurred. After solvent evaporation under reduced pressure, an aqueous suspension of NPs was obtained. Fluorescently labeled PLGA NPs were prepared by nanoprecipitation of PLGA 50:50 or 75:25 (12 mg) in the presence of 16.8 µg of Nile red (9-diethylamino-5H-benzo[α]phenoxazine-5-one, Sigma) dissolved in acetone; this solution was then added to 4 ml of MilliQ® water, as described for nonlabeled NPs. Fluorescent NPs were purified from nonincorporated dye by gel filtration on a Sepharose CL-4B column.

Hyaluronan (HA<sup>-</sup>TBA<sup>+</sup>,  $M_w = 2.2 \times 10^5$ , Contipro) was functionalized with cholesterol (15% mol per repeating unit) as previously reported [20]. For NHs preparation, 5 mg of hyaluronan-cholesterol were dispersed in 2.5 ml of MilliQ® water (2 mg/ml) overnight under magnetic stirring at 25°C; 2.5 ml of phosphate buffered saline (PBS; pH 7.4) were then added. Samples were autoclaved for 20 min at 121°C, leading to NHs formation [35]. For fluorescent NHs (Rhod-NHs) synthesis, rhodamine B-isothiocyanate (Sigma), was solubilized in DMSO (9 mg/ml) and then added to NHs aqueous suspension (8 µl for 1 mg of polymer, corresponding to a degree of functionalization of 6.3% mol/mol). The reaction mixture was left for 5 h at 25°C in the dark under magnetic stirring, followed by extensive dialysis (Mw cutoff: 12,000–14,000) and freeze-drying. The final functionalization degree was assessed through UV-Vis analysis in DMSO solution at 550 nm using a rhod calibration curve (8.5–125 µg/ml), resulting 1.3% mol/mol (mol of rhod per mol of hyaluronan-cholesterol repeating unit).

The mean particle size and the polydispersity index of liposomes, polymeric NPs and NHs were determined at 25°C by quasi-elastic light scattering using a nanosizer (Nanosizer Nano Z, Malvern Inst.). The selected angle was 173° and the measurement made after dilution of the nanoparticle suspension in MilliQ® water. Each measure was performed in triplicate.

Particle size of MSN was determined by measurements with a JEM 3010-UHR TEM (JEOL) operating at 300 kV. Powders were dispersed on a copper grid coated with a perforated carbon film. The size distribution of the samples was obtained by measuring 250 particles. The results are indicated as mean particle diameter ± standard deviation.

The particle surface charge of all formulations was investigated by ζ potential measurements at 25°C applying the Smoluchowski equation and using the Zetasizer Nano Z. Measurements were carried out in triplicate.

#### *In vitro* cell culture

C2C12 myoblasts (a spontaneously immortalized cell line from ECACC 91031101, Lot: 13K011, sex female) were grown in 25 cm<sup>2</sup> plastic flasks (1–2 × 10<sup>3</sup> cells/cm<sup>2</sup>) in Dulbecco's modified Eagle medium with 10% (v/v) FBS, 1% (w/v) Gln, 0.5% (v/v) AmpB, 100 units/ml of PS (Gibco, MA, USA), at 37°C in a 5% CO<sub>2</sub> humidified atmosphere. Under these culture conditions, myoblasts adhered to the substrate and, in 24 h, took the form of a spindle (about 50 µm in length and 20 µm in width).

Cells were trypsinized in PBS containing 0.05% EDTA when subconfluent (about 70%) and seeded on 24 or 96 multiwell plastic microplates for cell viability evaluation, or on glass coverslips in 12-multiwell microplates for CFM and TEM. All the experiments were performed with cells at passage 7–10. For myogenic differentiation, at 80% confluence the growth medium was substituted with the differentiation medium containing 1% FBS. Under these culture conditions, myoblasts ceased mitotic divisions and fused to form myotubes of variable lengths (up to about 400 µm).

Myoblasts were treated with the nanocarriers 1 day post-seeding, while myotubes were treated after 6 days in differentiation medium. The initial medium was replaced with a fresh one containing the nanocarriers, and the cells were incubated for 2, 24 and 48 h. At the end of each incubation time, the cells were processed as described below; untreated cells were used as controls. The C2C12 are highly proliferating cells with a cell cycle of about 20 h ([www.dsmz.de/catalogues/details/culture/ACC-565.html?tx\\_dsmzresources\\_pi5%5BreturnPid%5D=192](http://www.dsmz.de/catalogues/details/culture/ACC-565.html?tx_dsmzresources_pi5%5BreturnPid%5D=192)); therefore, a 48-h incubation time allows the completion of two cycles.

#### Myoblast viability & proliferation assay

To estimate the effect on cell viability and growth, three concentrations of each nanocarrier were tested: liposomes were administered at the concentrations of 125, 250 or 500 µg/ml (the weight refers to the lipid content); MSN

at 12.5, 25 or 50  $\mu\text{g/ml}$  (with reference to the weight of suspended MSN); PLGA NPs at 100, 200 or 400  $\mu\text{g/ml}$  (with reference to the polymer content); NHs at 50, 100 or 200  $\mu\text{g/ml}$  (with reference to the polymer content). The chosen concentrations previously proved to be noncytotoxic for various cultured cells [2,27–30]. Nanocarrier suspensions were prepared in DMEM with 200 units/ml PS, kept in the medium for 1 h at 37°C and then administered. According to [36], after each incubation time, 100  $\mu\text{l}$  of medium was removed and the release of the cytosolic enzyme LDH upon cell lysis was estimated with CytoTox96® Non-Radioactive Cytotoxicity Assay (Promega). In our experience, the results of this test proved to be consistent with those of the widely applied Trypan blue exclusion test, but with the advantage of using the culture medium while sparing the cells. Optical density was measured with a microplate reader (Tecan) at 490 nm. The relative amount of released LDH was normalized (as a percentage) to the total LDH release in control cells, which were completely lysed with lysis buffer provided in the kit. Results were expressed as the mean  $\pm$  standard error (SE) of five independent experiments.

To evaluate the cell population size,  $8 \times 10^3$  cells/well were seeded on 24 multiwell microplates. After incubation, the cells were detached by mild trypsinization and their total number estimated by counting in a Burker Turk hemocytometer; data were expressed as the mean  $\pm$  SE of three independent experiments.

To evaluate the effect of nanocarrier administration on myoblast proliferation ability, the S-phase cells fraction was estimated by BrdU incorporation after 24 and 48 h of incubation with nanocarrier concentrations that did not induce decrease in cell population, in other words, 125 of  $\mu\text{g/ml}$  liposomes, 50 of  $\mu\text{g/ml}$  MSN, 100 of  $\mu\text{g/ml}$  PLGA NPs and 100  $\mu\text{g/ml}$  of NHs. In detail, cells grown on coverslips were pulse labeled with 20  $\mu\text{M}$  BrdU (Sigma) for 30 min at 37°C, fixed with 70% ethanol and treated for 20 min at RT in 2N HCl, to denature DNA. After 3 min of neutralization with 0.1 M sodium tetraborate (pH 8.2), samples were washed in PBS, permeabilized for 15 min in PBS containing 0.1% FBS and 0.05% Tween-20 and incubated for 1 h with a mouse monoclonal antibody recognizing BrdU (1:20 in PBS; BD). After washing with PBS, samples were incubated for 1 h with an Alexafluor 488-conjugated anti-mouse antibody (1:200 in PBS; Life Technologies). Cells were washed with PBS, stained for 5 min with 1  $\mu\text{g/ml}$  of Hoechst 33342 (Sigma) in PBS, and finally mounted in PBS:glycerol (1:1) to be observed and scored in fluorescence microscopy (1000 cells per sample were counted).

In order to evaluate the occurrence of apoptotic cells (i.e., of cells committed to programmed death but undetectable by the usual viability tests), the samples used for the assessment of the S-phase fraction after 24 h of incubation with nanocarriers were also used to evaluate the percentage of apoptotic cells (1000 cells per sample were considered). Apoptotic nuclei were detected by microscope examination after Hoechst staining, based on the typical heterochromatin crescent-like morphology or nuclear fragmentation.

For the fraction of both S-phase and apoptotic cells, data were expressed as the mean  $\pm$  SE of three independent experiments. The Mann-Whitney U test was used to statistically compare treated and control samples.

An Olympus BX51 microscope equipped with a 100 W mercury lamp (Olympus Italia Srl) was used under the appropriate spectral conditions for FITC and Hoechst 33342. Images were recorded with a QICAM Fast 1394 digital camera (QImaging) and processed using Image-Pro Plus 7.0 software (Media Cybernetics Inc.).

#### Nanocarrier distribution in myoblasts & myotubes

For CFM, myoblasts and myotubes were incubated for 2 and 24 h with Fluo-Lipo, Fluo-MSN, Nile Red-labeled PLGA NPs or Rhod-NHs at the concentrations found to be noncytotoxic by cell viability and proliferation tests. At each incubation time, cells were fixed with 4% (v/v) paraformaldehyde in PBS, pH 7.4, for 30 min at RT.

To visualize the intracellular distribution of fluorescent nanocarriers, the cells were washed in PBS, incubated with either 0.1% Trypan blue (Gibco) or Phalloidin-Atto 594 or Phalloidin-Atto 488 (Sigma) diluted 1:20 in PBS, stained for DNA with Hoechst 33342 (1  $\mu\text{g/ml}$  in PBS), rinsed in PBS, and finally mounted in 1:1 mixture of glycerol:PBS.

To investigate nanocarrier uptake, live myoblasts were preincubated with either PKH26 Red Fluorescent Cell Linker or PKH67 Green Fluorescent Cell Linker (Sigma) to stain the plasma membrane, then incubated with the different fluorescently labeled nanocarriers for 30 min (this short time is necessary to label early endosomes only [37]) and finally fixed and processed for CFM, as described above. This procedure allowed detecting possible co-localization of the fluorescence signals of the internalized vesicles and nanocarriers, irrespective of the type of the occurring endocytic process (e.g., clathrin-mediated endocytosis, caveolin-mediated endocytosis, lipid-raft mediated endocytosis, phagocytosis, macro-pinocytosis). It is, in fact, known that cell internalization of nanoparticles depends on several factors, and the mechanisms may be multiple [38–40].

**Table 1. Characterization of nanocarriers.**

Nanocarriers	Mean diameter (nm ± SE)	Polydispersity index	ζ potential (mV ± SE)
Liposomes	180 ± 12	0.09	-15 ± 2.10
Fluo-lipo	177 ± 8	0.08	-14 ± 1.75
MSN	100 ± 23 <sup>†</sup>	–	+35 ± 0.90
Fluo-MSN	100 ± 23 <sup>†</sup>	–	+22 ± 0.60
PLGA NPs 50:50	109 ± 6	0.06	-33 ± 1.17
PLGA NPs 75:25	121 ± 4	0.05	-25 ± 0.64
PLGA NPs 50:50-Nile red	115 ± 4	0.06	-31 ± 2.34
PLGA NPs 75:25-Nile red	123 ± 3	0.04	-23 ± 1.72
NHs	200 ± 15	0.12	-38 ± 2
Rhod-NHs	250 ± 35	0.18	-35 ± 3

<sup>†</sup>Determined by transmission electron microscopy analysis.  
SE: Standard error.

For CFM, a Leica TCS SP5 AOBs system (Leica Microsystems Italia) was used: for fluorescence excitation, a diode laser at 405 nm for Hoechst 33342, an Ar laser at 488 nm for FITC and a He/Ne laser at 543 nm for Trypan blue, Nile Red and Rhod were employed. Z-stack of 1 μm step sized images (1024 × 1024 pixel format) was collected.

For TEM, myoblasts and myotubes were incubated for 2, 24 and 48 h with the nanocarriers at the same concentrations used for CFM. Cells were fixed with 2.5% (v/v) glutaraldehyde and 2% (v/v) paraformaldehyde in 0.1 M PBS, pH 7.4, at 4°C for 2 h, postfixed with 1% OsO<sub>4</sub> at RT for 1 h, dehydrated with acetone and embedded in Epon. Ultrathin sections were observed unstained or after weak staining with UAR-EMS Uranyl acetate replacement stain (Electron Microscopy Science). Observations were made in a Philips Morgagni TEM (FEI Company Italia Srl), operating at 80 kV and equipped with a Megaview II camera for digital image acquisition.

## Results

### Characterization of nanocarriers

Nanocarrier features are summarized in Table 1. Moreover, MSN showed an ordered mesoporous structure with MCM-41-like hexagonal array, resulting in high specific surface area of around 800 m<sup>2</sup>/g and pore size about 3 nm.

### Myoblasts viability & proliferation

Cell viability was evaluated after 2, 24 and 48 h of nanocarrier treatment; the LDH test demonstrated values ranging from 2.09 to 12.71% for all nanocarriers, at no variance with control samples for any incubation time (data not shown).

The total number of cells (Figure 1) was similar in control samples and in samples exposed to 75:25 PLGA NPs at all times considered. Conversely, cell populations exposed to liposomes, MSN, 50:50 PLGA NPs and NHs underwent significant modification in comparison with controls; in detail, liposomes and NHs induced a significant decrease after 48 h of incubation, while 50:50 PLGA NPs induced a decrease after both 24 and 48 h. Cell population exposed to MSN showed a significant increase after 48 h of incubation.

The amount of myoblasts incorporating BrdU (i.e., the S-phase fraction) did not significantly change after 24 h of incubation except for 50:50 PLGA NPs and for NHs; in detail, S-phase cells increased for 50:50 PLGA NPs 100 μg/ml, while decreased for NHs 100 μg/ml. After 48 h of incubation, no change was found (Figure 2).

Morphologically recognizable apoptotic nuclei were quite scarce in all samples after 24 h of incubation with the different nanocarriers and their percentage was similar in control (0.40 ± 0.24%) and treated cells (liposomes 0.51 ± 0.17%, MSN 0.38 ± 0.28%, 50:50 PLGA NPs 0.22 ± 0.15%, 75:25 PLGA NPs 0.22 ± 0.22%, NHs 0.29 ± 0.16%).

### Nanocarrier distribution in myoblasts & myotubes

#### Liposomes

The CFM showed that, in myoblasts, liposomes were mostly found in the peripheral cytoplasmic region, never entering the nucleus. They always appeared as isolated fluorescing spots which never formed aggregates nor markedly

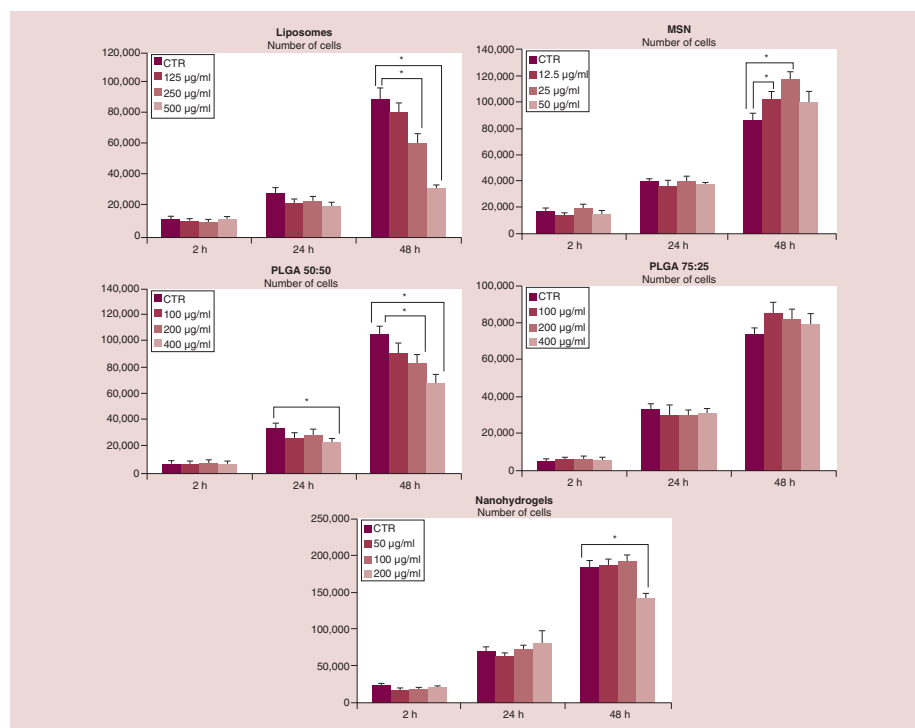


**Figure 1.** Evaluation of cell population. Mean values ± SE of cell number after 2, 24 and 48 h of incubation with the nanocarriers. Asterisks indicate significant difference with control cells at the same incubation time. MSN: Mesoporous silica nanoparticles; PLGA: Poly(lactide-co-glycolide); SE: Standard error.

accumulated in the cell; their intracellular amount was evidently larger after 24 h of incubation (Figure 3A & B). In myotubes, only few liposomes were found in the peripheral and perinuclear region of the cytoplasm after all incubation times (Figure 3C). Fluorescent liposomes never co-located with fluorescing intracellular membranes (Figure 3D).

At TEM, liposomes were strongly electron-dense due to the lipid staining by OsO<sub>4</sub>; in both myoblasts and myotubes, their number was very low and they occurred at the cell periphery just beneath the cell membrane (Figure 3E) or in the perinuclear area (Figure 3G). No endocytic or phagocytotic processes were observed; accordingly, liposomes were always found to occur free in the cytosol. In myoblasts, a fine electron-dense granular material was freely distributed in the cytosol and in close proximity to lipid droplets (Figure 3F). Cell nuclei and cytoplasmic organelles of both myoblasts and myotubes never showed morphological alterations.

#### Mesoporous silica nanoparticles

The CFM revealed that, in both myoblasts and myotubes, after 2 h of incubation, MSN mostly occurred as aggregates at the cell surface; only a few small clusters were observed inside the cytoplasm. After 24 h of incubation, many MSN clusters were distributed in the cytoplasm, preferentially around, but never inside, the cell nuclei (Figure 4A–

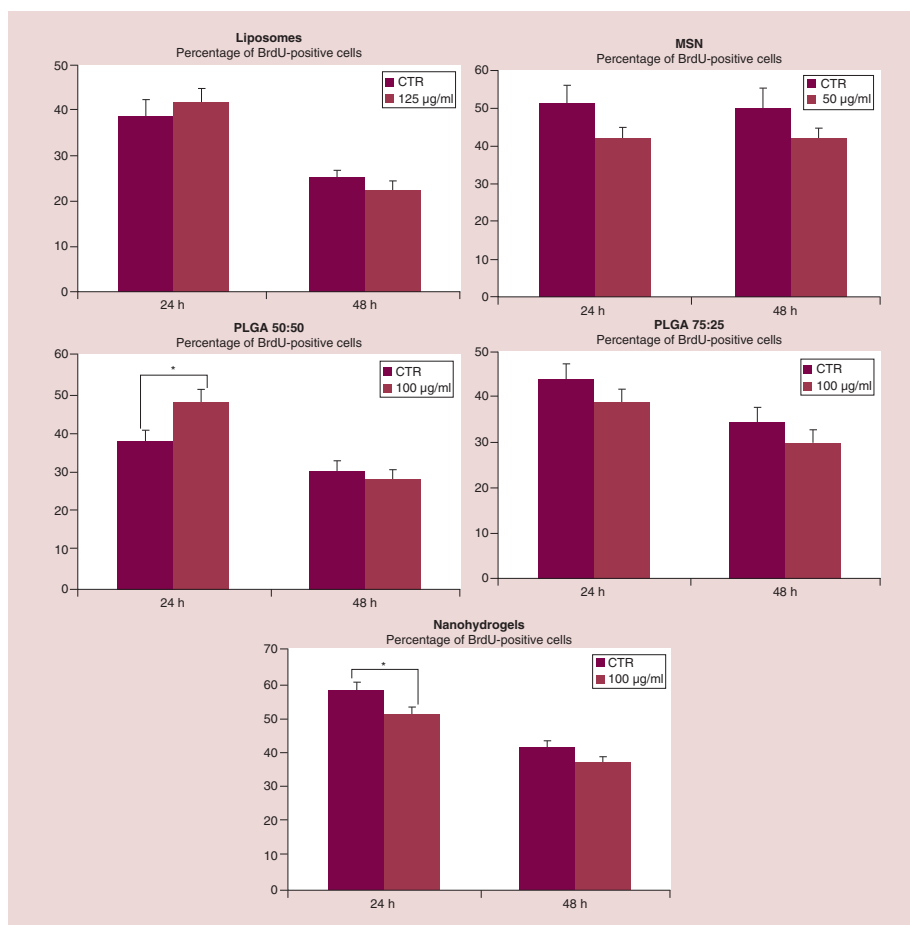


**Figure 2.** Evaluation of S-phase cells. Mean values  $\pm$  SE of BrdU-positive cell percentage after 24 and 48 h of incubation with the nanocarriers. Asterisks indicate significant difference with control cells at the same incubation time. MSN: Mesoporous silica nanoparticles; PLGA: Poly(lactide-co-glycolide); SE: Standard error.

C). Fluo-MSN co-located with fluorescing intracellular membranes, thus suggesting they were internalized via endocytosis (Figure 4D).

At TEM, the MSN were roundish and highly electron-dense. According to the CFM observations, aggregates of MSN were found adhering to the cell surface and to be internalized by endocytosis (Figure 4E). In the cytoplasm, MSN were always found inside ubiquitously distributed vacuoles of various sizes, but they were never observed inside the nuclei (Figure 4E & F). After 24 and 48 h of incubation, MSN accumulated inside large vacuoles

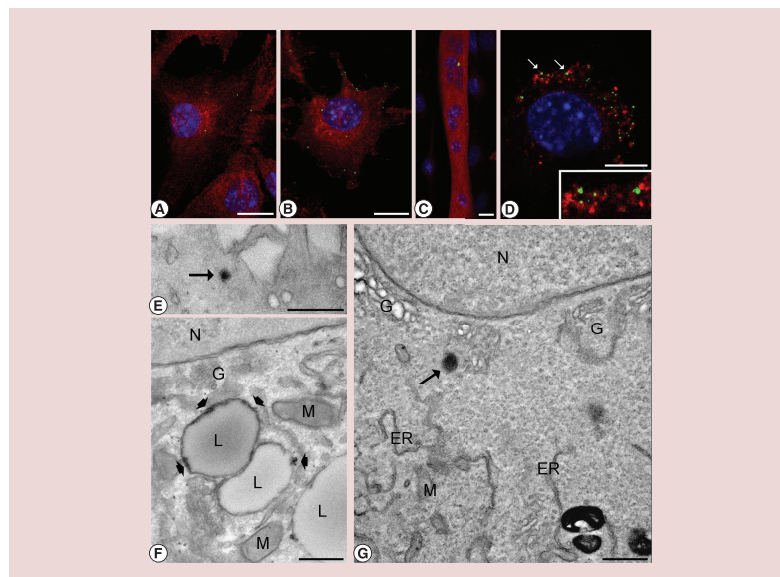


**Figure 3.** Microscopical analysis of liposomes uptake and intracellular distribution. CFM optical sections of myoblasts (A & B) and myotubes (C) after 2 h (A) and 24 h (B & C) of liposome incubation. Cytoplasm was stained with trypan blue (red fluorescence) and DNA with Hoechst 33342 (blue). (D) A myoblast incubated with PKH26 (red, to visualize endocytic vesicles) and with liposomes (green): the two signals never co-located. Inset: 2x magnification of the detail (small arrows). Bars: 20 μm (A–C), 10 μm (D). TEM analysis of liposome intracellular distribution in myoblasts (E & F) and myotubes (G) after 24 h of incubation. (E) A liposome (arrow) occurs free in the cytoplasm at the cell periphery. (F) Electron-dense fine granular material (arrowheads) in close proximity of lipid droplets (L). (G) A liposome (arrow) in perinuclear position. Note the good structural preservation of cell organelles in both myoblasts and myotubes: nucleus (N), Golgi complex (G), mitochondria (M), endoplasmic reticulum (ER). Bars: 500 nm. CFM: Confocal fluorescence microscopy; TEM: Transmission electron microscopy.

(probably secondary lysosomes) and sometimes appeared as loosened (Figure 4G & H). The MSN always remained confined inside vacuoles and did not contact any cell organelle. No sign of subcellular alteration or organelle damage was observed at any incubation time in both myoblasts and myotubes.

#### *Poly(lactide-co-glycolide) nanoparticles*

Observations at CFM and TEM were similar for the two formulations of PLGA NPs.

The CFM showed that, in both myoblasts and myotubes, after 2 h of incubation, a few PLGA NPs were present in the cytoplasm; after 24 h of incubation, they accumulated in large amount in the cytoplasm, often forming aggregates, preferentially in the perinuclear area, but never entering the nucleus (Figure 5A–C). Overlapping of red-fluorescing PLGA NPs and green-fluorescing membrane marker suggested the occurrence of endocytic processes (Figure 5D).

At TEM, PLGA NPs showed a regular roundish shape and moderate electron density. After 2 h of incubation, single NPs were seldom observed inside endosomes at the cell periphery (Figure 5E) and some NPs exhibited endosomal escape (Figure 5F), but most of PLGA NPs were found free in the cytosol (Figure 5G). After 24 and 48 h of incubation, numerous residual bodies containing roundish moderately electron-dense structures (likely NP remnants) accumulated in the cytoplasm (Figure 5H & I); these particular residual bodies were never found

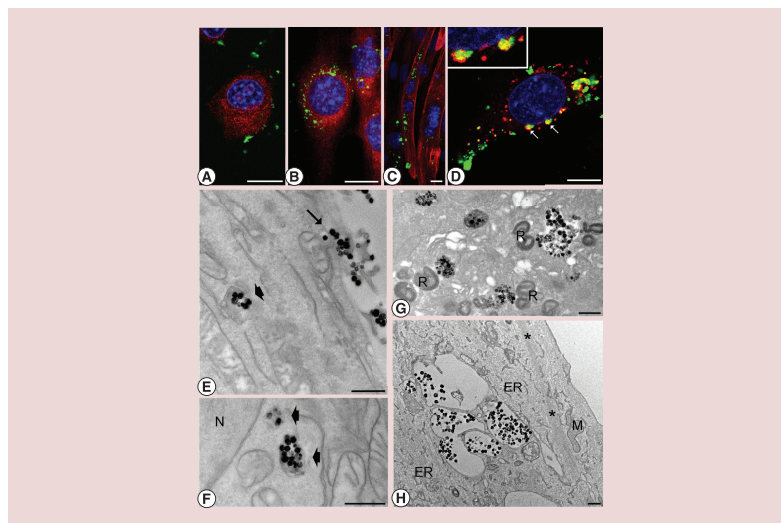


**Figure 4.** Microscopical analysis of mesoporous silica nanoparticles uptake and intracellular distribution. CFM optical sections of myoblasts (A & B) and myotubes (C) 2 h (A) and 24 h (B & C) after incubation with MSN. DNA was stained with Hoechst 33342 (blue) and the cytoplasm counterstained for actin with phalloidin (red). (D) A myoblast incubated with PKH26 (red, to visualize endocytic vesicles) and with Fluo-MSN (green): the two signals co-locate (yellow). Inset: 2 $\times$  magnification of the detail (small arrows). Bars: 20  $\mu$ m (A–C), 10  $\mu$ m (D). TEM analysis of MSN intracellular distribution after 2 h (E & F) and 24 h (G) of incubation in myoblasts, and after 24 h of incubation in myotubes (H). (E) Clusters of MSN occur at the cell surface; some of them are enclosed in a membrane invagination (arrow). Internalized MSN occur inside a vacuole (arrowhead). (F) Vacuoles containing MSN (arrowheads) locate very close to the nucleus (N). (G) After 24 h of incubation, in myoblasts MSN accumulate in vacuoles, while the cytoplasm contains many residual bodies (R). (H) In myotubes, after 24 h of incubation, MSN occur in large vacuoles without perturbing the typical structural organization: bundles of myofibrils (asterisks), mitochondria (M), endoplasmic reticulum (ER). Bars: 500 nm.

CFM: Confocal fluorescence microscopy; MSN: Mesoporous silica nanoparticles.

in control cells or in samples treated with the other nanocarriers. The PLGA NPs were never found inside the nucleus nor making contact with cytoplasmic organelles. No cell alteration or damage was observed in myoblasts and myotubes at any incubation time.

#### Nanohydrogels

The CFM showed that only low amounts of NHs were internalized in myoblasts after 2 h, while after 24 h NHs were present in large quantity in the cytoplasm, especially in the perinuclear region (Figure 6A & B). They were never found inside the nucleus. In myotubes, NHs were observed in the cytoplasm only after 24 h, but their amount was always very low (Figure 6C).

The red fluorescence of NHs was found to co-locate with the green-fluorescing membrane marker (Figure 6D), thus suggesting that internalization occurs *via* endocytosis.

At TEM, NHs appeared as roundish homogeneously electron-dense structures. They were found to adhere to the cell surface inside invaginations of the plasma membrane (Figure 6E) and, in the cytoplasm, a few of them were observed inside endosomes (Figure 6F). However, most of NHs occurred free in the cytosol, and were often partially surrounded by double membranes, as it typically occurs during autophagic processes (Figure 6G). Some NH remnants were still recognizable inside secondary lysosomes (Figure 6H). The NHs were never found to

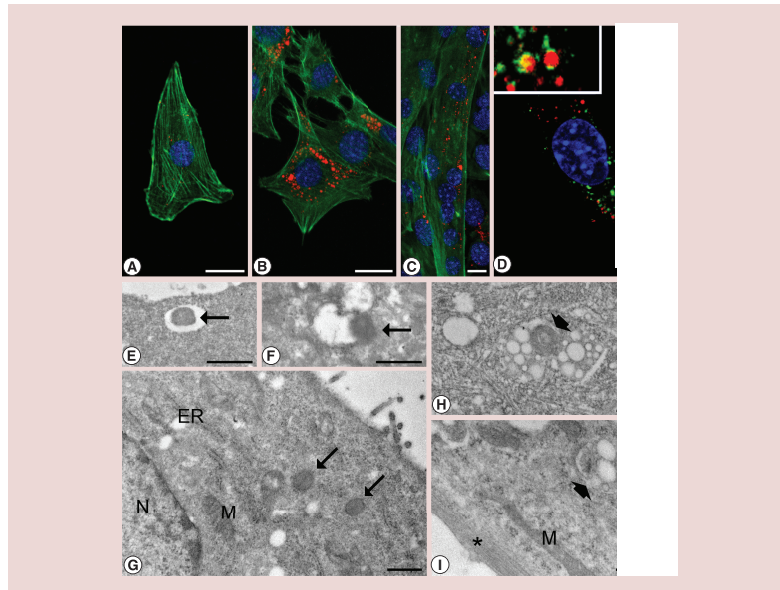


**Figure 5. Microscopical analysis of poly(lactide-co-glycolide) nanoparticles uptake and intracellular distribution.** CFM optical sections of myoblasts (A & B) and myotubes (C) after 2 h (A) and 24 h (B & C) of PLGA NPs incubation. DNA was stained with Hoechst 33342 (blue) and the cytoplasm counterstained for actin with phalloidin (green). (D) A myoblast incubated with PKH67 (green, to visualize endocytic vesicles) and with PLGA NPs (red): the two signals co-locate (yellow). Inset: 2× magnification of the detail (small arrow). Bars: 20 μm (A–C), 10 μm (D). TEM analysis of PLGA NPs intracellular distribution after 2 h (E–G) and 24 h (H) of incubation in myoblasts, and after 24 h of incubation in myotubes (I). (E) A PLGA NP enclosed in an endosome (arrow) occurs just beneath the cell surface. (F) A PLGA NP (arrow) is escaping from an endosome. (G) Two PLGA NPs (arrows) occur free in the cytosol. (H) After 24 h of incubation, the cytoplasm contains large amounts of peculiar vacuolated residual bodies where some NP remnants occurs (arrowhead). (I) In myotubes, after 24 h of incubation, the same residual bodies (arrowheads) are frequently present. Nucleus (N), Golgi complex (G), mitochondria (M), endoplasmic reticulum (ER), bundles of myofibrils (asterisk). Bars: 500 nm.  
CFM: Confocal fluorescence microscopy; PLGA NP: Poly(lactide-co-glycolide) nanoparticle.

make contact with cell organelles or to occur inside the nucleus; moreover, no sign of cell structural alteration was observed in both myoblasts and myotubes.

### Discussion

This study aimed at investigating the possible influence of cytokinetic features on the cellular response to different nanocarriers previously demonstrated to be safe for various established cancer cell lines [2,27–30]. In particular, we considered skeletal muscle cells at two differentiation steps characterized by distinct cytokinetic features: highly cycling myoblasts and terminally differentiated noncycling myotubes.

Under our experimental conditions, myoblast viability as well as the apoptotic rate were unaffected by the exposure to all the tested nanocarriers. Consistently, no nanocarrier induced quantitative reduction of myoblast population, apart from the highest concentrations tested at the longest incubation times, when the intracellular accumulation of nanocarriers likely perturbed cell proliferation. Indeed, MSN administration led to a significant increase in cell population, probably related to the silica-NP-induced activation of MAPK signaling and the downregulation of

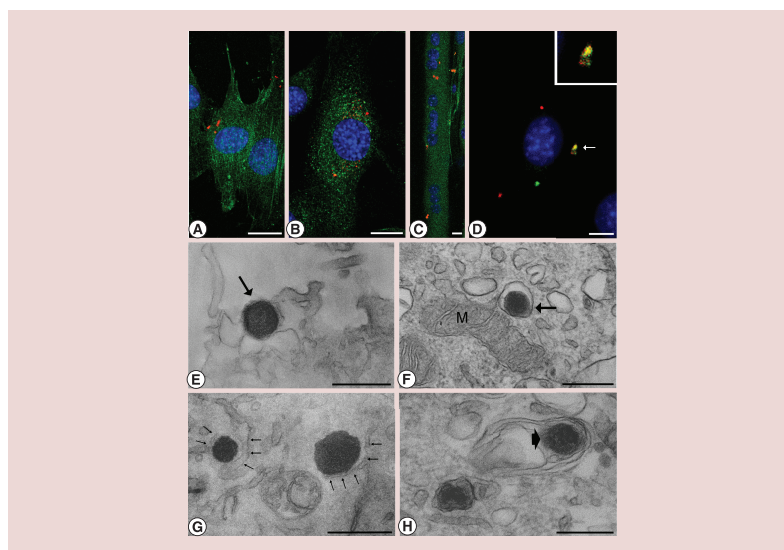


**Figure 6. Microscopical analysis of nanohydrogel uptake and intracellular distribution.** CFM optical sections of myoblasts (A & B) and myotubes (C) after 2 h (A) and 24 h (B & C) of NH incubation. DNA was stained with Hoechst 33342 (blue) and the cytoplasm counterstained for actin with phalloidin (green). (D) A myoblast incubated with PKH67 (green, to visualize endocytic vesicles) and then with NHs (red): the two signals co-localize (yellow). Inset: 2× magnification of the detail (small arrow). Bars: 20 μm (A-C), 10 μm (D). TEM analysis of NHs intracellular distribution after 2 h (E & F) and 24 h (G & H) of incubation in myoblasts. (E) A NH (arrow) occurs at the cell surface. (F) A NH is enclosed in an endosome (arrow). (G) Two NHs (arrows) occur free in the cytosol and are partially enclosed by autophagic double-membranes (small arrows). (H) A residual body with a NH remnant (arrowhead). Mitochondria (M). Bars: 500 nm. CFM: Confocal fluorescence microscopy; NH: Nanohydrogel; TEM: Transmission electron microscopy.

*p53*, which in turn inhibit apoptosis and induce cell proliferation [41]. The amount of S-phase cells was also found to be unaffected after liposomes, MSN and 75:25 PLGA NP, and even increased after 50:50 PLGA NP administration, thus definitely demonstrating that liposomes, MSN and both PLGA NP formulations do not negatively affect the proliferation capability of myoblasts. On the other hand, NHs administration induced a decrease of S-phase cells number after 24 h, followed by a recovery after 48 h and thus suggesting a transitory hindering of DNA synthesis, without negative effects on cell population at longer incubation times. This phenomenon could be due to cell overloading after 24 h of incubation, as suggested by the evidence at CFM.

Altogether, our results provide evidence that all the tested nanocarriers are highly biocompatible to C2C12 myoblasts. However, biocompatibility is here attained at lower concentrations than those reported as safe for some cancer cell lines [2,27–30]. It is known that different cell types may differently react to nanocarrier administration; in particular, a comparative *in vitro* study demonstrated that myoblasts are much more sensitive than other cell types [42]. In addition, our results demonstrate that C2C12 myoblasts internalize nanocarriers more slowly than other cell types [28,43,44]. We may speculate that these differences may depend on different metabolic rates or peculiar cell features, such as dissimilar membrane composition or endocytic capability.

Anyway, the uptake mechanisms and intracellular fate observed in C2C12 myoblasts correspond to those already reported for other cells.

The experimental evidence of both CFM (fluorescing liposomes never overlap fluorescently labeled vesicles) and TEM (liposomes never occur inside endosomes) indicates that liposomes enter the cells mostly by mechanisms

different from typical endocytosis. It is in fact likely that liposomes, due to their lipidic nature, are internalized by a direct translocation through the plasmalemma, probably by fusion with the cell membrane [45-47]. Once inside the cytoplasm, as observed in HeLa cells [28], liposomes undergo rapid degradation and migrate in the cytosol toward lipid droplets, probably for chemical affinity: this prevents their intracellular accumulation and explains their preferential occurrence at the cell periphery. However, in HeLa cells lipid droplets became so numerous to be extruded from the cell [28], whereas in C2C12 myoblasts no accumulation and/or extrusion of lipid droplet was observed, probably due to the lower concentrations of liposomes administered.

Consistent with previous observations [9,28,48] CFM and TEM confirmed that MSN enter the myoblasts by endocytosis and follow the endolytic pathway, always remaining confined inside membrane-bounded vacuoles and never entering the nucleus. This is probably the reason for the absence of cell injury even after long-term exposure (7 days) [48]; moreover, MSN uptake in C2C12 myoblasts was shown to enhance their differentiation into myotubes [48], opening interesting perspectives for the use of this nanocarrier for muscle tissue therapy.

At both formulations, PLGA NPs enter the cell as single units by endocytosis; however, they rapidly escape from the endosomes, as already observed for other polymeric NPs [49,50], and occur free in the cytosol without making contact with any organelle. Afterward, PLGA NPs re-enter the lytic pathway by autophagic processes [51-53], undergoing enzymatic degradation and giving rise to numerous residual bodies. Their presence as free NPs in the cytosol is therefore transient and it is likely that most of the fluorescing spots detectable at CFM are remnants of PLGA NPs inside residual bodies. Similarly to other polymeric NPs [28,54,55], PLGA NPs do not enter the nucleus.

The NHs also are endocytosed, as already reported for cancer cells [30,43,56], but our data provide the first ultrastructural evidence of their intracellular fate. The NH uptake in C2C12 appears to be less efficient than in cancer cells. It has been reported that NHs show CD44-dependent endocytosis [30], whose efficiency could be related to the expression levels of this transmembrane protein: consistently, C2C12 cells do express CD44 [57], but cancer cells are often characterized by a very high expression of this receptor [58,59]. Once in the cytoplasm, NHs seem to rapidly escape endosomes in C2C12 cells; in fact, findings of NHs occurring free in the cytosol are very frequent, whereas endosomes containing NHs are quite scarce. However, free NHs re-enter the lytic pathway by autophagic process and finally degraded by lysosomal enzymes. Lysosomal degradation has been also found in HaCaT keratinocytes, where NHs were observed to co-locate with acidic organelles (Montanari *et al.*, submitted).

The C2C12 myotubes, treated with nanocarrier concentrations which were safe for myoblasts, did not show any sign of cell stress, thus extending biocompatibility to noncycling differentiated muscle cells. However, it was evident that the amount of nanocarriers internalized by myotubes was lower than in myoblasts. Similarly, other NPs which easily enter myoblasts did not penetrate myotubes [60]. Such a difference may reside in the higher metabolic rate of a cycling cell compared with its differentiated noncycling counterpart [31]. Moreover, the differentiation process of myoblasts into myotubes entails a differential expression of numerous proteins among which those related to cell adhesion, transmembrane transport, and cytoskeleton composition and dynamics [61-63], as well as of cell membrane lipids and fatty acids [64]. Furthermore, cell size markedly increases in myotubes compared with myoblasts. All these cell modifications could affect nanocarrier uptake depending on the internalization mechanisms involved [65]. A further factor could play a role in the different internalization rate observed in myoblasts and myotubes: the protein corona [66]. Taking into consideration that the composition of the culture media for myoblasts and myotubes was similar but not identical, the adsorption of environmental proteins on nanocarriers could have modified their physicochemical properties, thus affecting their interactions with the cells.

Once internalized into the myotubes, all nanovectors undergo a fate similar to that observed in myoblasts, without perturbing cell organelles.

### Conclusion

Taken together, our results demonstrate that all the tested nanocarriers are suitably biocompatible for both cycling myoblasts and noncycling myotubes although the differentiation stage markedly affects the uptake efficiency (and this should be taken into consideration when designing nanoconstructs for therapeutic or diagnostic purposes). At the concentrations used in our experiments, all the tested NPs enter the intracellular environment and undergo degradation through the physiological pathways without inducing microscopically detectable cytological alterations. The high biocompatibility to muscle cells of these nanoconstructs is also supported by their inability to enter the nucleus, thus avoiding the unpredictable long-term risks of possible interactions between nanomaterials and nucleic acids and/or nuclear protein factors. All these features make these nanocarriers potential candidates for delivering therapeutic agents *in vivo* for treating also diseased differentiated cells, which are to be preserved.

### Future perspective

Looking at the scientific literature, up to now, most of the nanocarriers designed for drug delivery have been intended to treat cancer (i.e., to kill highly metabolizing cycling cells); on the contrary, less attention has so far been paid in nanomedical research to cure terminally differentiated noncycling diseased cells, such as muscle or neuronal cells. There are several neuromuscular diseases, especially those of genetic origin, still lacking specific treatment; in some cases, promising therapeutic molecules have been experimentally identified, but they have scarce applicability because of their low *in vivo* bioavailability due to either enzymatic degradation or high systemic toxicity. Nanotechnology may represent a successful strategy to respond to the need of coping therapy efficacy while decreasing adverse tissue-specific and systemic side effects. Our research aims at identifying biocompatible and biodegradable nanocarriers suitable for muscle cells. The present work is the first step of a long way: the results obtained herein using an established muscle cell line provided the experimental background for further studies presently in progress to test nanocarriers in human primary muscle cells from healthy subjects and patients affected by neuromuscular diseases, as well as to perform appropriate nanocarrier functionalization to promote preferential uptake by the target tissue. The application of nanotechnology to cure tissues and organs mainly composed by nonrenewing cells represents a new challenge. By using appropriate experimental models mimicking the complexity of a living organ [67], and taking into account the multiple physicochemical interactions to which the nanocarriers are submitted in the biological environment [65], this research field will undergo a rapid development in the next few years.

### Summary points

- Liposomes, mesoporous silica nanoparticles (MSN), poly(lactide-co-glycolide) nanoparticles (PLGA NPs) and nanohydrogels (NHs) are biocompatible and versatile systems to encapsulate active agents.
- Since nanocarrier effects may depend on the cytokinetic features, cell uptake and distribution of liposomes, MSN, PLGA NPs and NHs were investigated by microscopical techniques in an immortalized murine myoblast cell line able to undergo mitosis as myoblasts (cycling cells) and to terminally differentiate into myotubes (noncycling cells).
- Under our experimental conditions, myoblast viability and proliferation were unaffected by the exposure to all the tested nanocarriers.
- Liposomes enter the cells by fusion with plasma membrane and undergo rapid cytoplasmic degradation.
- The MSN enter by endocytosis and persist in the cytoplasm enclosed in vacuoles.
- The PLGA NPs and NHs enter by endocytosis, escape endosomes but undergo autophagic process and, finally, enzymatic degradation.
- For each nanocarrier, internalization mechanisms and intracellular distribution are similar in myoblasts and myotubes.
- The amount of nanocarriers internalized by myotubes is lower than in myoblasts.
- Myoblasts and myotubes do not show cytological alterations following nanocarrier uptake.

### Ethical conduct of research

The authors state that they have obtained appropriate institutional review board approval or have followed the principles outlined in the Declaration of Helsinki for all human or animal experimental investigations. In addition, for investigations involving human subjects, informed consent has been obtained from the participants involved.

### Financial & competing interests disclosure

This work was supported by the Italian Ministry for University and Research (MIUR)-University of Turin, 'Fondi Ricerca Locale (ex-60%)'. The authors have no other relevant affiliations or financial involvement with any organization or entity with a financial interest in or financial conflict with the subject matter or materials discussed in the manuscript apart from those disclosed.

No writing assistance was utilized in the production of this manuscript.

### Author contributions

M Costanzo organized the experimental work, participated in cell culture and nanocarrier testing, and performed transmission electron microscopy observations. F Vurro and B Cisterna performed cell culture and nanocarrier testing, and prepared samples for microscopical analyses. F Boschi performed confocal microscopy analyses. E Montanari, CD Meo and P Matricardi synthesized and

characterized nanohydrogels. G Berlier synthesized and characterized mesoporous silica nanoparticles. B Stella synthesized and characterized PLGA nanoparticles. S Arpico and A Marengo synthesized and characterized liposomes. M Malatesta conceived the experimental design, interpreted the results and wrote the manuscript.

## References

Papers of special note have been highlighted as: ● of interest

- Dilnawaz F, Acharya S, Sahoo SK. Recent trends of nanomedicinal approaches in clinics. *Int. J. Pharm.* 538(1-2), 263–278 (2018).
- Arpico S, Lerda C, Dalla Pozza E et al. Hyaluronic acid-coated liposomes for active targeting of gemcitabine. *Eur. J. Pharm. Biopharm.* 85(3 Pt A), 373–380 (2013).
- **Preparation and characterization of liposomes.**
- Pedrini I, Gazzano E, Chegaev K et al. Liposomal nitrooxy-doxorubicin: one step over Caelyx® in drug-resistant human cancer cells. *Mol. Pharm.* 11(9), 3068–3079 (2014).
- Slowing II, Vivero-Escoto JL, Wu CW, Lin VS. Mesoporous silica nanoparticles as controlled release drug delivery and gene transfection carriers. *Adv. Drug Deliv. Rev.* 60(11), 1278–1288 (2008).
- **The advantages of using mesoporous silica nanoparticles for drug delivery, including proofs of concept for their potential as stimuli responsive nanodevices.**
- Chen Y, Chen H, Shi J. Drug delivery/imaging multifunctionality of mesoporous silica-based composite nanostructures. *Expert Opin. Drug Deliv.* 11(6), 917–930 (2014).
- Sapino S, Ugazio E, Gastaldi L et al. Mesoporous silica as topical nanocarriers for quercetin: characterization and *in vitro* studies. *Eur. J. Pharm. Biopharm.* 89, 116–125 (2015).
- Peng J, He X, Wang K et al. An antisense oligonucleotide carrier based on amino silica nanoparticles for antisense inhibition of cancer cells. *Nanomedicine* 2(2), 113–120 (2006).
- Malfanti A, Mileto I, Bottinelli E et al. Delivery of gemcitabine prodrugs employing mesoporous silica nanoparticles. *Molecules* 21(4), 522 (2016).
- Ricci V, Zonari D, Cannito S et al. Hyaluronated mesoporous silica nanoparticles for active targeting: influence of conjugation method and hyaluronic acid molecular weight on the nanovector properties. *J. Colloid. Interface Sci.* 516, 484–497 (2018).
- **The mesoporous silica nanoparticles stability toward aggregation and cell internalization is improved by one-pot conjugation with high molecular weight hyaluronan.**
- Stella B, Arpico S, Rocco F et al. Encapsulation of gemcitabine lipophilic derivatives into polycyanoacrylate nanospheres and nanocapsules. *Int. J. Pharm.* 344(1-2), 71–77 (2007).
- Stella B, Marsaud V, Arpico S et al. Biological characterization of folic acid-conjugated poly(H<sub>2</sub>NPEGCA-co-HDCA) nanoparticles in cellular models. *J. Drug Target* 15(2), 146–153 (2007).
- **Biodegradable polymeric nanoparticles are versatile systems for passive and active drug targeting.**
- Lince F, Bolognesi S, Stella B, Marchisio DL, Dosio F. Preparation of polymer nanoparticles loaded with doxorubicin for controlled drug delivery. *Chem. Eng. Res. Des.* 89(11), 2410–2419 (2011).
- Grottkau BE, Cai X, Wang J, Yang X, Lin Y. Polymeric nanoparticles for a drug delivery system. *Curr. Drug Metab.* 14(8), 840–846 (2013).
- Danhier F, Ansorena E, Silva JM, Coco R, Le Breton A, Pr at V. PLGA-based nanoparticles: an overview of biomedical applications. *J. Control. Rel.* 161(2), 505–522 (2012).
- Kapoor DN, Bhatia A, Kaur R, Sharma R, Kaur G, Dhawan S. PLGA: a unique polymer for drug delivery. *Ther. Deliv.* 6(1), 41–58 (2015).
- Kabanov AV, Vinogradov SV. Nanogels as pharmaceutical carriers: finite networks of infinite capabilities. *Angew. Chem. Int. Ed. Engl.* 48(30), 5418–5429 (2009).
- Soni KS, Desale SS, Bronich TK. Nanogels: an overview of properties, biomedical applications and obstacles to clinical translation. *J. Control. Rel.* 240, 109–126 (2016).
- Choi KY, Jeon EJ, Yoon HY et al. Theranostic nanoparticles based on PEGylated hyaluronic acid for the diagnosis, therapy and monitoring of colon cancer. *Biomaterials* 33(26), 6186–6193 (2012).
- Montanari E, D'Arrigo G, Di Meo C et al. Chasing bacteria within the cells using levofloxacin-loaded hyaluronic acid nanohydrogels. *Eur. J. Pharm. Biopharm.* 87(3), 518–523 (2014).
- **Hyaluronan-cholesterol nanohydrogels were loaded with levofloxacin and their ability to enter cells and treat intracellular infections was demonstrated.**
- Montanari E, Capece S, Di Meo C et al. Hyaluronic acid nanohydrogels as a useful tool for BSAO immobilization in the treatment of melanoma cancer cells. *Macromol. Biosci.* 13(9), 1185–1194 (2013).

21. Ganguly K, Chaturvedi K, More UA, Nadagouda MN, Aminabhavi TM. Polysaccharide-based micro/nanohydrogels for delivering macromolecular therapeutics. *J. Control. Rel.* 193, 162–173 (2014).
- **Polysaccharide-based micro- and nanosystems and their ability to deliver macromolecular therapeutics were extensively reviewed.**
22. Akiyoshi K, Deguchi S, Moriguchi N, Yamaguchi S, Sunamoto J. Self-aggregates of hydrophobized polysaccharides in water. Formation and characteristics of nanoparticles. *Macromolecules* 26(12), 3062–3068 (1993).
23. Vinogradov S, Batrakova E, Kabanov A. Poly(ethylene glycol)-polyethyleneimine NanoGel™ particles: novel drug delivery systems for antisense oligonucleotides. *Colloids Surf. B Biointerfaces* 16(1-4), 291–304 (1999).
24. Di Meo C, Montanari E, Manzi L, Villani C, Coviello T, Matricardi P. Highly versatile nanohydrogel platform based on riboflavin-polysaccharide derivatives useful in the development of intrinsically fluorescent and cytocompatible drug carriers. *Carbohydr. Polym.* 115, 502–509 (2015).
25. Pedrosa SS, Gonçalves C, David L, Gama M. A novel crosslinked hyaluronic acid nanogel for drug delivery. *Macromol. Biosci.* 14(11), 1556–1568 (2014).
26. Montanari E, Gennari A, Pelliccia M *et al.* Hyaluronan/tannic acid nanoparticles via catechol/boronate complexation as a smart antibacterial system. *Macromol. Biosci.* 16(12), 1815–1823 (2016).
27. Slowing I, Trewyn BG, Lin VS. Effect of surface functionalization of MCM-41-type mesoporous silica nanoparticles on the endocytosis by human cancer cells. *J. Am. Chem. Soc.* 128(46), 14792–14793 (2006).
28. Costanzo M, Carton F, Marengo A *et al.* Fluorescence and electron microscopy to visualize the intracellular fate of nanoparticles for drug delivery. *Eur. J. Histochem.* 60(2), 2640 (2016).
29. Jonderian A, Maalouf R. Formulation and *in vitro* interaction of rhodamine-B loaded PLGA nanoparticles with cardiac myocytes. *Front. Pharmacol.* 7, 458 (2016).
30. Quagliariello V, Jaffaioli RV, Armenia E *et al.* Hyaluronic acid nanohydrogel loaded with quercetin alone or in combination to a macrolide derivative of rapamycin RAD001 (Everolimus) as a new treatment for hormone-responsive human breast cancer. *J. Cell Physiol.* 232(8), 2063–2074 (2017).
31. Chang JS, Chang KL, Hwang DF, Kong ZL. *In vitro* cytotoxicity of silica nanoparticles at high concentrations strongly depends on the metabolic activity type of the cell line. *Environ. Sci. Technol.* 41(6), 2064–2068 (2007).
- **Nanoparticle internalization depends on the metabolic activity of the cell.**
32. Strohmman RC, Paterson B, Fluck R, Przybyla A. Cell fusion and terminal differentiation of myogenic cells in culture. *J. Anim. Sci.* 38(5), 1103–1110 (1974).
33. Yu M, Jambhrunkar S, Thorn P, Chen J, Gu W, Yu C. Hyaluronic acid modified mesoporous silica nanoparticles for targeted drug delivery to CD44-overexpressing cancer cells. *Nanoscale* 5(1), 178–183 (2013).
34. Fessi H, Puisieux F, Devissaguet JPH, Ammoury N, Benita S. Nanocapsule formation by interfacial polymer deposition following solvent displacement. *Int. J. Pharm.* 55(1), R1–R4 (1989).
35. Montanari E, De Rugeris MC, Di Meo C *et al.* One-step formation and sterilization of gellan and hyaluronan nanohydrogels using autoclave. *J. Mater. Sci. Mater. Med.* 26(1), 5362 (2015).
36. Thomas MG, Marwood RM, Parsons AE, Parsons RB. The effect of foetal bovine serum supplementation upon the lactate dehydrogenase cytotoxicity assay: important considerations for *in vitro* toxicity analysis. *Toxicol. In Vitro* 30(1 Pt B), 300–308 (2015).
37. Grecchi S, Malatesta M. Visualizing endocytotic pathways at transmission electron microscopy via diaminobenzidine photo-oxidation by a fluorescent cell-membrane dye. *Eur. J. Histochem.* 58(4), 2449 (2014).
38. Oh N, Park JH. Endocytosis and exocytosis of nanoparticles in mammalian cells. *Int. J. Nanomedicine* 9(Suppl. 1), 51–63 (2014).
39. Behzadi S, Serpooshan V, Tao W *et al.* Cellular uptake of nanoparticles: journey inside the cell. *Chem. Soc. Rev.* 46(14), 4218–4244 (2017).
40. Ding L, Zhu X, Wang Y *et al.* Intracellular fate of nanoparticles with polydopamine surface engineering and a novel strategy for exocytosis-inhibiting, lysosome impairment-based cancer therapy. *Nano Lett.* 17(11), 6790–6801 (2017).
41. Christen V, Camenzind M, Fent K. Silica nanoparticles induce endoplasmic reticulum stress response, oxidative stress and activate the mitogen-activated protein kinase (MAPK) signaling pathway. *Toxicol. Rep.* 1, 1143–1151 (2014).
42. Nie Y, Zhang ZR, He B, Gu Z. Investigation of PEG-PLGA-PEG nanoparticles-based multipolyplexes for IL-18 gene delivery. *J. Biomater. Appl.* 26(8), 893–916 (2012).
43. Pan YJ, Chen YY, Wang DR *et al.* Redox/pH dual stimuli-responsive biodegradable nanohydrogels with varying responses to dithiothreitol and glutathione for controlled drug release. *Biomaterials* 33(27), 6570–6579 (2012).
44. Freichels H, Danhier F, Pr at V, Lecomte P, J r me C. Fluorescent labeling of degradable poly(lactide-co-glycolide) for cellular nanoparticles tracking in living cells. *Int. J. Artif. Organs* 34(2), 152–160 (2011).
45. Verma A, Stellacci F. Effect of surface properties on nanoparticle–cell interactions. *Small* 6(1), 12–21 (2010).
46. Nazareus M, Zhang Q, Soliman MG *et al.* In vitro interaction of colloidal nanoparticles with mammalian cells: what have we learned thus far? *Beilstein J. Nanotechnol.* 5, 1477–1490 (2014).

47. Lanza R, Langer R, Vacanti JP. *Principles of tissue engineering*. Lanza R, Langer R, Vacanti JP. (Eds). 4<sup>th</sup> ed. Academic Press, New York, USA, p 1344 (2011).
48. Poussard S, Decossas M, Le Bihan O, Mornet S, Naudin G, Lambert O. Internalization and fate of silica nanoparticles in C2C12 skeletal muscle cells: evidence of a beneficial effect on myoblast fusion. *Int. J. Nanomed.* 10, 1479–1492 (2015).
49. Varkouhi AK, Scholte M, Storm G, Haisma HJ. Endosomal escape pathways for delivery of biologicals. *J. Control. Rel.* 151(3), 220–228 (2011).
50. Malatesta M, Giagnacovo M, Costanzo M et al. Diaminobenzidine photoconversion is a suitable tool for tracking the intracellular location of fluorescently labelled nanoparticles at transmission electron microscopy. *Eur. J. Histochem.* 56(2), e20 (2012).
51. Malatesta M, Grecchi S, Chiesa E, Cisterna B, Costanzo M, Zancanaro C. Internalized chitosan nanoparticles persist for long time in cultured cells. *Eur. J. Histochem.* 59(1), 2492 (2015).
52. Zhang J, Chang D, Yang Y et al. Systematic investigation on the intracellular trafficking network of polymeric nanoparticles. *Nanoscale* 9(9), 3269–3282 (2017).
53. Panyam J, Labhasetwar V. Biodegradable nanoparticles for drug and gene delivery to cells and tissue. *Adv. Drug. Deliv. Rev.* 55(3), 329–347 (2003).
54. Kim HR, Gil S, Andrieux K et al. Low-density lipoprotein receptor-mediated endocytosis of PEGylated nanoparticles in rat brain endothelial cells. *Cell Mol. Life Sci.* 64(3), 356–364 (2007).
55. Brambilla D, Nicolas J, Le Droumaguet B, Andrieux K, Marsaud V, Couraud PO. Design of fluorescently tagged poly(alkyl cyanoacrylate) nanoparticles for human brain endothelial cell imaging. *Chem. Commun. (Camb)* 46(15), 2602–2604 (2010).
56. Palvai S, Kuman MM, Basu S. Hyaluronic acid coated oleic acid nanoparticles inhibit MAPK signaling with sub-cellular DNA damage in colon cancer cells. *J. Mat. Chem. B* 5, 3658–3666 (2017).
57. Kaneko K, Higuchi C, Kunugiza Y et al. Hyaluronan inhibits BMP-induced osteoblast differentiation. *FEBS Lett.* 589(49), 447–454 (2015).
58. Morath I, Hartmann TN, Orian-Rousseau V. CD44: more than a mere stem cell marker. *Int. J. Biochem. Cell Biol.* 81(Pt A), 166–173 (2016).
59. Senbanjo LT, Chellaiah MA. CD44: a multifunctional cell surface adhesion receptor is a regulator of progression and metastasis of cancer cells. *Front. Cell Dev. Biol.* 5, 18 (2017).
60. Salova AV, Leontieva EA, Mozhenok TP, Kornilova ES, Krolenko SA, Belyaeva TN. Change in localization of cellular vesicular apparatus during differentiation of myoblasts into myotubes in cell culture. *Cell Tissue Biol.* 5(3), 255–263 (2011).
61. Kislinger T, Gramolini AO, Pan Y, Rahman K, MacLennan DH, Emili A. Proteome dynamics during C2C12 myoblast differentiation. *Mol. Cell. Proteomics* 4(7), 887–901 (2005).
62. Casadei L, Vallorani L, Gioacchini AM et al. Proteomics-based investigation in C2C12 myoblast differentiation. *Eur. J. Histochem.* 53(4), e31 (2009).
63. Forterre A, Jalabert A, Berger E et al. Proteomic analysis of C2C12 myoblast and myotube exosome-like vesicles: a new paradigm for myoblast-myotube cross talk? *PLoS ONE* 9(1), e84153 (2014).
64. Briolay A, Jaafar R, Nemoz G, Bessueille L. Myogenic differentiation and lipid-raft composition of L6 skeletal muscle cells are modulated by PUFAs. *Biochim. Biophys. Acta* 1828(2), 602–613 (2013).
65. Mahmoudi M. Debugging nano-bio interfaces: systematic strategies to accelerate clinical translation of nanotechnologies. *Trends Biotechnol.* 36(8), 755–769 (2018).
66. Rahman M, Laurent S, Tawil N, Yahia L, Mahmoudi M. Nanoparticle and protein corona. In: *Protein-Nanoparticle Interactions (Volume 15)*. Martinac B. (Ed). Springer Series in Biophysics. Springer, Berlin, Heidelberg, Germany, 21–44 (2013).
67. Carton F, Calderan L, Malatesta M. Incubation under fluid dynamic conditions markedly improves the structural preservation *in vitro* of explanted skeletal muscles. *Eur. J. Histochem.* 61(4), 2862 (2017).

## **V. BIBLIOGRAPHY**

---

## V. Bibliography

---

- Abenojar C., Wickramasinghe S., Bas-Concepcion J. And Samia A. C. S., “Structural effects on the magnetic hyperthermia properties of iron oxide nanoparticles” *Progress in Natural Science : Materials International*. (2016), 26, 440-448.
- Acharya S. and Sahoo S. K., “Effects of Sonication Processing on the Behavior of the Synthesis Human Serum Albumin-SPIONs Loaded PLGA Nanoparticles, *Advanced Drug Delivery Rev.* (2011), 63, 170–183.
- Banerjee S. S. and Chen D. H., “Magnetic Nanoparticles Grafted with Cyclodextrin for Hydrophobic Drug Delivery” ,*Chemical Materials*. (2007), 19 , 6345 —6349.
- Bernabucci U., Lacetera N., Danieli P. P., Bani P., Nardone A., Ronchi B., “Influence of different periods of exposure to hot environment on rumen function and diet digestibility in sheep”, *International Journal of Biometeorology*. (2009), 53: 387.
- Bowerman C.J., Byrne J.D., Chu K.S., Schorzman A.N., Keeler A.W., Sherwood C.A., Perry J.L., Luft J.C., Darr D.B., Deal A.M., “Docetaxel-loaded PLGA nanoparticles improve efficacy in taxane-resistant triple-negative breast cancer”. *Nano Letters*, (2017),17:242–248.
- Cao M.D., Cheng M., Rizwan A., Jiang L., Krishnamachary B., Bhujwala Z.M., Bathen T.F., Glunde K., “targeting choline phospholipid metabolism: GDPD5 and GDPD6 silencing decrease breast cancer cell proliferation, migration, and invasion” *NMR in biomedicine*. (2016), 29, 1098 1107.
- Chandrasekharan, P.; Tay, Z. W.; Hensley, D.; Zhou, X. Y.; Fung, B. K.; Colson, C.; Lu, Y.; Fellows, B. D.; Huynh, Q.; Saayujya, C.; Yu, E.; Orendorff, R.; Zheng, B.; Goodwill, P.; Rinaldi, C.; Conolly, S., “Using magnetic particle imaging systems to localize and guide magnetic hyperthermia treatment: tracers, hardware, and future medical applications”. *Theranostics*. (2020), 10 (7), 2965-2981.

## V. Bibliography

---

- Chang, M. Lim, J. A. C. M. Goos, R. Qiao, Y. Y. Ng, F. M. Mansfeld, M. Jackson, T. P. Davis and M. Kavallaris, “Biologically Targeted Magnetic Hyperthermia: Potential and Limitations”, *Frontiers in Pharmacology*. (2018), 9, 831.
- Cherukuri P., Glazer E. S. and Curley S. A., “Targeted Hyperthermia Using Metal Nanoparticles”, *Adv. Drug Delivery Rev.*, 2010, 62, 339–345.
- Das, P.; Colombo, M.; Prospero, D., Recent advances in magnetic fluid hyperthermia for cancer therapy. *Colloids Surf B Biointerfaces* **2019**, 174, 42-55.
- Di Corato R., Béalle G., Kolosnjaj-tabi J, Espinosa A., Clément O., Silva A.K.A., Ménager C., C. Wilhelm, “Combining magnetic hyperthermia and photodynamic therapy for tumor ablation with photoresponsive magnetic liposomes *ACS Nano*, (2015), pp. 2904-2916.
- E. CazaresCortes, A. Espinosa, J.M. Guigner, A. Michel, N. Griffete, C. Wilhelm, C.Ménager, “Doxorubicin intracellular remote release from biocompatible oligo(ethylene glycol) methyl ether methacrylate-based magnetic nanogels triggered by magnetic hyperthermia”, *ACS Appl Mater Interfaces*. (2017), 9(31):25775-25788.
- E. Natividad, M. Castro and A. Mediano, “Accurate measurement of the specific absorption rate using a suitable adiabatic magnetothermal setup”, *Applied Physics Letter*. (2008), 92, 093116.
- Ellis R.J. , “Roles of molecular chaperones in protein folding”, *Ann Rev Biochem*, (1994), pp. 321-347.
- Farkhani S.M., Valizadeh A., Karami H., Mohammadi S., Sohrabi N., Badrzadeh F.. “Cell penetrating peptides: efficient vectors for delivery of nanoparticles, nanocarriers, therapeutic and diagnostic molecules”. *Peptides*, (2014), 57:78–94.
- Fortin J. P., Gazeau F. and Wilhelm C., “Intracellular heating of living cells through Néel relaxation of magnetic nanoparticles”, *European biophysics Journal*. (2008), 37, 223–228.
- Fortin-Ripoche J. P., Martina M. S., Gazeau F., Menager C., Wilhelm C., Bacri J. C., Lesieur S. and Clement O., *Radiology*, “Magnetic targeting of magnetoliposomes to solid tumors with MR imaging monitoring in mice: feasibility”, *radiology*. (2006),239,415–424.

## V. Bibliography

---

G. Hegyi, G.P. Szigeti, A Szász, “Hyperthermia versus Oncothermia: Cellular Effects in Complementary Cancer Therapy”, *Evidence- Based Complementary and Alternative Medicine*. (2013), 672873.

García Rubia, G.; Peigneux, A.; Jabalera, Y.; Puerma, J.; Oltolina, F.; Elert, K.; Colangelo, D.; Gómez Morales, J.; Prat, M.; Jimenez-Lopez, C. “pH-Dependent Adsorption Release of Doxorubicin on MamC-Biomimetic Magnetite Nanoparticles”, *Langmuir*. (2018), 34, 13713–13724.

Glunde K., Bhujwala Z.M., Ronen S.M., “Choline metabolism in malignant transformation”. *Nature Reviews. Cancer*. (2011), 11, 835–848.

Golstein P.and Kroemer G., *Trends Biochem. Sci.*, (2007), 32, 37–43. “Cell death by necrosis: towards a molecular definition”, *Sci.*, (2007), 32, 37–43.

Greish K., Mathur A., Bakhiet M., Taurin S., “Nanomedicine: is it lost in translation?” *Therapeutic Delivery*. (2018), 9(4):269-285.

Hamdy S., Haddadi A., Hung R.W., Lavasanifar A., “Targeting dendritic cells with nanoparticulate PLGA cancer vaccine formulations”, *Advanced Drug Delivery Reviews*. (2011), 63:943–955.

Harrington K.J., Mohammadtaghi S., Uster P.S., Glass D., Peters A.M., Vile R.G., Stewart J.S., “Effective targeting of solid tumors in patients with locally advanced cancers by radiolabeled pegylated liposomes”, *Clinical Cancer Research*. (2001), 7(2):243-54.

Hergt and Dutz S., J, “Magnetic particle hyperthermia—biophysical limitations of a visionary tumour therapy”, *Journal of Magnetism and Magnetic Materials*. (2007), 311, 187– 192.

Hergt R, Hiergeist R., Zeisberger M., Glockl G., Weitschies W., Ramirez P., Hilger I and Kaiser W. A., “Enhancement of AC-losses of magnetic nanoparticles for heating applications”, *Journal of Magnetism and Magnetic Materials*. (2004), 280,

## V. Bibliography

---

358–368.

Hergt R., Dutz S., Muller R. and Zeisberger M., “Magnetic particle hyperthermia: nanoparticle magnetism and materials development for cancer therapy”, *Journal of physics: Condensed Matter*. (2006), 18, S2919–S2934.

Hervault and N. T. K. Thanh, “Magnetic nanoparticle-based therapeutic agents for thermo-chemotherapy treatment of cancer”, *Nanoscale*, (2014), 6, 11553-11573.

Hildebrandt, Wust P., Ahlers O., Dieing A., Sreenivasa G., Kerner T., Felix R. and Riess H., “The cellular and molecular basis of hyperthermia”, *Critical Reviews in Oncology/Hematology* (2002), 43, 33–56. 29.

Hu Y., Meng L., Niu L. and Lu Q., “Highly Cross-Linked and Biocompatible Polyphosphazene-Coated Superparamagnetic Fe<sub>3</sub>O<sub>4</sub> Nanoparticles for Magnetic Resonance Imaging”, *Langmuir*. (2013), 29 , 9156 —9163.

Huang H. S. and Hainfeld J. F., “Intravenous magnetic nanoparticle cancer hyperthermia”, *International Journal of Nanomedicine*. (2013), 8, 2521–2532.

Huang S., Wang S. Y., Gupta A., Borca-Tasciuc D. A. and Salon S. J., “On the measurement technique for specific absorption rate of nanoparticles in an alternating electromagnetic field”,

Issels R. D., “Hyperthermia adds to chemotherapy”, *European journal of Cancer*. (2008), 44, 2546–2554.

J.N. Van der Veen, J.P. Kennelly, S. Wan, J.E. Vance, D.E. Vance, R.L. Jacobs, “The critical role of phosphatidylcholine and phosphatidylethanolamine metabolism in health and disease”. *Biochimica. Biophysica. Acta Biomembranes*. (2017), 1859, 1558–1572.

Jabalera Y., Sola-Leyva A., Peigneux A., Vurro F., Iglesias G R., Vilchez-Garcia J., Pérez-Prieto I., Aguilar-Troyano F J., López-Cara L C., Carrasco-Jiménez María P. and Jimenez-Lopez C. “Biomimetic Magnetic Nanocarriers Drive Choline Kinase Alpha Inhibitor inside Cancer Cells for Combined Chemo-Hyperthermia Therapy”, *Pharmaceutics*. (2019), 11(8), 408;

## V. Bibliography

---

- Jang J., Nah H., H J. Lee, Moon S. H., Kim M. G. and Cheon J., “Critical enhancements of MRI contrast and hyperthermic effects by dopant-controlled magnetic nanoparticles”, *Angewandte Chemie*. (2009), 48, 1234-1238.
- Johannsen M., Gneveckow U., Eckelt LFeussner., A., Waldofner N., Scholz R., Deger S., Wust P., Loening S. A. and Jordan A., “Clinical hyperthermia of prostate cancer using magnetic nanoparticles: presentation of a new interstitial technique”, *International Journal of Hyperthermia*. (2005), 21, 637–647.
- Jordan A, Wust P., Scholz R., Faehling H., Krause J. and Felix R., “Magnetic fluid hyperthermia (MFH): Cancer treatment with AC magnetic field induced excitation of biocompatible superparamagnetic nanoparticles”, *Journal of Magnetism and Magnetic Materials*. (1997), 978-1-4757-6482-6.
- Kallumadil M., Tada M., Nakagawa T., Abe M., Southern P., Pankhurst Q.A.. “Suitability of commercial colloids for magnetic hyperthermia”, *Journal of Magnetism and Magnetic Materials* 2009;321(10):1509–1513.
- Kerr J. F. R., Winterford C. M. and Harmon B. V., “Apoptosis, its significance in cancer therapy”, *Cancer*. (1994), 73, 2013–2026.
- Kotitz R., Weitschies W., Trahms L. and Semmler W., “Investigation of Brownian and Neel relaxation in magnetic fluids”, *Journal of Magnetism and magnetic materials*. (1999), 201, 102–104.
- Kregel K. C., “Heat shock proteins: modifying factors in physiological stress responses and acquired thermotolerance”, *journal of applied physiology*. (2002), 92(5):2177-86.
- Krishnan K. M., “Biomedical nanomagnetism: A spin through possibilities in imaging, diagnostics, and therapy”, *IEEE Trans. Magn.*, 2010, 46, 2523–2558.
- Kumar C.S.S.R. , Mohammad F., “Magnetic nanomaterials for hyperthermia-based therapy and controlled drug delivery”, *Adv. Drug Deliv. Rev.* (2011), 63(9): 789–808.
- Laszlo, “The effects of hyperthermia on mammalian cell structure and function”, *Cell proliferation*. (1992), 25(2):59-87.

## V. Bibliography

---

- Laurent S., Dutz S., Häfeli U.O., Mahmoudi M., “Magnetic fluid hyperthermia: focus on superparamagnetic iron oxide nanoparticles”, *Adv. Colloid Interface Sci.* (2011), 166(1-2):8-23.
- Lee C.T., Mace T., and Repasky E.A., “Hypoxia-driven immunosuppression: a new reason to use thermal therapy in the treatment of cancer”, *International journal of hyperthermia.* (2010), 26(3):232-246.
- Lee N., Kim H., Choi S. H, Park M., Kim D., Kim H. C, Choi Y., Lin S., Kim B. Magnetosome-like ferromagnetic iron oxide nanocubes for highly sensitive MRI of single cells and transplanted pancreatic islets H, Jung H. S., Kim H., Park K. S, Moon W. K. and Hyeon T., *Proc. Natl. Acad. Sci. U. S. A.*, (2011), **108**, 2662-2667.
- Lee N. and Hyeon T., “Designed synthesis of uniformly sized iron oxide nanoparticles for efficient magnetic resonance imaging contrast agents. *Chem. Soc. Rev.*, (2012), 41, 2575-2589.
- Lepock J. R., “Cellular effects of hyperthermia: relevance to the minimum dose for thermal damage”, *International Journal of Hyperthermia.* (2003), 19, 252–266.
- Levy M., Wilhelm C., Siaugue J.-M., Horner O., Bacri J.-C. and Gazeau F., “Magnetically induced hyperthermia: size-dependent heating power of  $\gamma$ -Fe<sub>2</sub>O<sub>3</sub> nanoparticles” *Journal of Physics.: Condensed Matter.* (2008), 20, 204133.
- Liu X.L., Fan H.M., Yi J.B., Yang Y., Choo E.S.G., Xue J.M., Fan D. D. and Ding J. “Optimization of surface coating on Fe<sub>3</sub>O<sub>4</sub> nanoparticles for high performance magnetic hyperthermia agents”, *Journal of Material Chemistry* (2012), 22, 8235.
- Maeda H., Khatami M., “Analyses of repeated failures in cancer therapy for solid tumors: poor tumor-selective drug delivery, low therapeutic efficacy and unsustainable costs”, *Clinical and Translational Medicine.* (2018),7(1):11.)
- Mahmoudi K., Bouras A., Bozec D., Ivkov R. and Hadjipanayis C., “Magnetic hyperthermia therapy for the treatment of glioblastoma: a review of the therapy’s history, efficacy and application in humans”, *International Journal of Hyperthermia.* (2018), 34, 1316-1328.

## V. Bibliography

---

Maier-Hauff K., Rothe R., Scholz R., Gneveckow U., Wust P., Thiesen B., Feussner A., A. von Deimling, Waldoefner N., Felix R. and Jordan A., “Intracranial Thermotherapy using Magnetic Nanoparticles Combined with External Beam Radiotherapy: Results of a Feasibility Study on Patients with Glioblastoma Multiforme”, *Journal of Neuro-oncology*. (2007), 81, 53–60.

Marinozzi M.R., Pandolfi L., Malatesta M., Colombo M., Collico V., Lievens P. M. J., Tambalo S., Lasconi C., Vurro F., Boschi F., Mannucci S., Sbarbati A., Prosperi D, Calderan L. “Innovative approach to safely induce controlled lipolysis by superparamagnetic iron oxide nanoparticles-mediated hyperthermic treatment”, *Int. J. Biochem. Cell Biol.*,2017, 93, 62-73.

Moyer H.R. and Delman K.A., “the role of hyperthermia in optimizing tumor response to regional therapy”, *International journal of hyperthermia*. (2008), 24:3, 251-261.

Noh S., Moon S. H., Shin T. H., Lim Y. and Cheon J., “Ultrathin Interface Regime of Core-Shell Magnetic Nanoparticles for Effective Magnetism Tailoring”, *Nano Today*. (2017), 13, 61-76.

Pankhurst Q. A., Connolly J., Jones S. K and Dobson J., “Applications of magnetic nanoparticles in biomedicine”, *journal of physics*. (2003), 36, R167-R181.

Prozorov T., D.A. Bazylinski, S.K. Mallapragada, R Prozorov,” Novel magnetic nanomaterials inspired by magnetotactic bacteria: Topical review” *Mater. Sci. Eng. R Rep.* (2013), 74, 133–172.

Purushotham S., Chang P. E., Rumpel H., Kee I. H., Ng R. T., Chow P. K., Tan C. K. and Ramanujan R. V., “Thermoresponsive core-shell magnetic nanoparticles for combined modalities of cancer therapy”, *Nanotechnology*( 2009), 20 , 305101.

Rahimi M., Wadajkar A., Subramanian K., Yousef M., Cui W. N., Hsieh J. T. and Nguyen K. T., “In vitro evaluation of novel polymer-coated magnetic nanoparticles for controlled drug delivery”, *Nanomedicine: Nanotechnology, Biology and Medicine*. (2010), 6 , 672 —680.

## V. Bibliography

---

- Rao W., Deng Z.-S. and Liu J., “A review of hyperthermia combined with radiotherapy/chemotherapy on malignant tumors”, *CRC Crit. Rev. Bioeng.* (2010), 38, 101–116.
- Sanson , O. Diou , J. Thevenot , E. Ibarboure , A. Soum , A. Brulet , S. Miraux , E. Thiaudiere , S. Tan , A. Brisson , V. Dupuis , O. Sandre and S. Lecommandoux, “Doxorubicin loaded magnetic polymersomes: theranostic nanocarriers for MR imaging and magneto-chemotherapy”, *ACS Nano.* (2011), 5 , 1122 —1140.
- Santini B., Zanoni I., Marzi R., Cigni C., Bedoni M., Gramatica F., Palugan L., Corsi F., Granucci F., Colombo M., “Cream formulation impact on topical administration of engeneered colloidal nanoparticles“, *PLoS One.* (2015).
- Sharifi, H. Shokrollahi and S. Amiri, “Ferrite-Based Magnetic Nanofluids Used in Hyperthermia Applications”, *Journal of Magnetism and magnetic materials.* (2012), 324, 903–915.
- Shen Z., Wu A. and Chen X., “Iron oxide nanoparticle based contrast agents for magnetic resonance imaging” *Mol. Pharmaceutics* (2017), 14, 1352-1364.
- Siemann W., The Unique Characteristics of Tumor Vasculature and Preclinical Evidence for its Selective Disruption by Tumor-Vascular Disrupting Agents”, *Cancer Treat. Rev.* (2011), 37, 63–74.
- Song W., “Effect of local hyperthermia on blood flow and microenvironment: a review”, *Cancer Research.* (1984), 44, 4721s–4730s.
- Song W., Park H. and Griffin R. J., “Improvement of tumor oxygenation by mild hyperthermia” *Radiat. Res.* (2001), 155, 515–528.
- Suto M., Hirota Y., Mamiya H., Fujita A., Kasuya R., Tohji K. and Jeyadevan B., “Heat dissipationmechanism of magnetite nanoparticles in magnetic fluid hyperthermia”, *Journal of Magnetism and Magnetic Materials.* (2009), 321, 1493– 1496. 57.
- Theato P., Sumerlin B. S., O'Reilly R. K. and Epps T. H., “Stimuli responsive materials”, *Chemical Society Reviews.* (2013), 42, 7055–7056.
- Torchilin V., “Tumor delivery of macromolecular drugs based on the EPR effect”, *Advanced Drug Deliv Rev.* (2011), 63:131–135.

## V. Bibliography

---

- Van der Zee J.,” Effect of Cytoreductive Surgery Combined with Intraoperative Intra-Thoracic Hyperthermic Chemotherapy in Patients with Advanced Non-Small Cell Lung Cancer”, *Ann. Oncol.* (2002), 13, 1173–1184.
- Veiseh O., Gunn JW., Zhang M., “Design and fabrication of magnetic nanoparticles for targeted drug delivery and imaging”, *Advanced Drug Delivery Reviews.* (2010), 62(3):284–304.
- Wang H., Shrestha T. B., Basel M. T., Dani R. K., Seo G. M., Balivada S., Pyle M. M., Prock H., Koper O. B., Thapa P. S., Moore D., Li P., Chikan V., Troyer D. L. and Bossmann S. H., “Magnetic-Fe/Fe(3)O(4)-nanoparticle-bound SN38 as carboxylesterase-cleavable prodrug for the delivery to tumors within monocytes/macrophages”, *Beilstein J. Nanotechnology.* (2012), 3, 444 —455.
- Ward M. A. and Georgiou T. K., “Thermoresponsive Polymers for Biomedical Applications”, *Polymers.* (2011), 3, 1215– 1242.
- Willingham M. C., “Cytochemical Methods for the Detection of Apoptosis”, *J. Histochemistry and Cytochemistry.* (1999), 47, 1101–1109 .
- Wust P., Hildebrandt B., Sreenivasa G., Rau B., Gellermann J., Riess H., Felix R. and Schlag P. M., “Hyperthermia in combined treatment of cancer” *Lancet Oncol.* (2002), 3, 487–497.
- Yalcin, B. Clem, S. Makoni, A. Clem, K. Nelson, J. Thornburg, D. Siow, A.N. Lane, S.E. Brock, U.Goswami, “Selective inhibition of choline kinase simultaneously attenuates MAPK and PI3K/AKT signaling”, *Oncogene.* (2010), 29, 139–149.
- Zulauf G. D., Trembly B. S., Giustini A. J., Flint B. R., Strawbridge R. R. and Hoopes P. J., *Energy-Based Treatment of Tissue and Assessment VII.* (2013), 8584.